Winter 12-15-2021

Interfacial Engineering and Photoelectrochemistry of Patterned Metal/Semiconductor Heterostructures

Che Tan
Washington University in St. Louis

WASHINGTON UNIVERSITY IN ST. LOUIS

McKelvey School of Engineering
Department of Energy, Environmental & Chemical Engineering

Dissertation Examination Committee:
Bryce Sadtler, Chair
Pratim Biswas
William Buhro
Elijah Thimsen
Jay Turner

Interfacial Engineering and Photoelectrochemistry of Patterned Metal/Semiconductor Heterostructures

by

Che Tan

A dissertation presented to
The Graduate School
of Washington University in
partial fulfillment of the
requirements for the degree
of Doctor of Philosophy

December 2021
St. Louis, Missouri

Table of Contents

List of Figures

List of Tables

List of Abbrevations and Symbols

RHE	Reversible hydrogen electrode
HER	Hydrogen evolution reaction
OER	Oxygen evolution reaction
MIS	Metal-insulator-semiconductor
SEM	Scanning electron microscope
TEM	Transmission electron microscope
ALD	Atomic layer deposition
RIE	Reactive ion etching
PVD	Physical vapor deposition
ICP	Inductively coupled plasma
J-E	Current density *vs.* potential
CV	Cyclic voltammetry
LSV	Linear sweep voltammetry
EIS	Electrochemical impedance spectroscopy
FIB	Focused ion-beam
Φ_b	Barrier height
J_s	Dark saturation current
J_L	Limiting current density
n	Diode quality factor
V_{oc}	Open-circuit voltage

N_D	Donor density
V_n	Energy difference between the conduction band edge and the Fermi level
Δ	Barrier-height difference
W	Depletion width
V_{bb}	Degree of band bending
SPR	Surface plasmon resonance
AFM	Atomic force microscopy
NPGS	Nanometer Pattern Generation System
ITO	Indium-doped tin oxide
MACE	Metal-assisted chemical etching
FDTD	Finite Difference Time Domain

Acknowledgments

I would foremost like to thank my advisor, Dr. Bryce Sadtler. I really appreciate the high value he put on graduate education and the mentoring that he offered. I want to thank him for the wisdom, kindness, and attention to detail that he showed us. I would also like to thank him for his guidance, patience, and encouragement for the past five years. Thank you for giving me the opportunity to learn and expertise in so many amazing instruments and techniques.

I would like to thank all members of my thesis committee, Dr. Elijah Thimsen, Dr. Jay Turner, Dr. Pratim Biswas, and Dr. William Buhro, for sharing time with me and giving me valuable suggestions. I would especially like to thank Dr. Pratim Biswas for his generous support, and I am grateful for this opportunity.

I would like to thank all the staff of the Institute of Material Science & Engineering for their patience and the precious training quality they provided. I would like to give special thanks to the cleanroom manager Dr. Rahul Gupta for training me on almost all the equipment in the cleanroom and answering my countless questions. Thanks for being such a wonderful cleanroom manager who always tried his best to help me out and offered me with so much encouragement.

I would like to thank present and past members of the Sadtler lab for creating a great environment for doing research. Thank Dr. Meikun Shen for many useful experimental advice and Dongyan Zhang for offering help in muscular capacities. I enjoyed our discussions, including our research, philosophy of life, policies, and sports.

I would like to thank Dr. Nathan Reed from the Biswas lab, for the technical expertise he provided and for the willingness to help whenever I needed him. I missed the fun discussions while

we were always fixing the thermal evaporator. I would also like to thank Dr. Dian Tan from the Murch lab for helping me with electron beam lithography and the brilliant insights he often provided.

Last but not least, I would like to thank my brother, who was also a doctoral student at WashU. He is the one who initiated my interest in science and research and is always there when I need him. I would like to thank my mom for her enduring care and emotional support. I would also like to thank my husband for his continuous support from Madison and then Portland. Finally, I would like to thank my entire family for encouraging me to fulfill my dream with all the love and support.

Che Tan

Washington University in St. Louis

December 2021

Dedicated to my brother.

ABSTRACT OF THE DISSERTATION

Interfacial Engineering and Photoelectrochemistry of Patterned Metal/Semiconductor Heterostructures

by

Che Tan

Doctor of Philosophy

Energy, Environmental & Chemical Engineering

Washington University in St. Louis, 2021

Professor Bryce Sadtler, Chair

Photoelectrochemical (PEC) cells enable the conversion of solar energy into storable fuels, which is critical in overcoming the intermittent nature of this largest renewable source. However, the majority of semiconductors used as photoelectrodes in these cells have low conversion efficiencies and/or stabilities. Silicon (Si) is an attractive semiconductor material for photoelectrodes, but the development of efficient Si-based photoanodes is challenging due to their instability in alkaline solutions. Thus, one focus of this dissertation is the design and fabrication of highly stable nickel (Ni)-patterned Si photoanodes through interfacial engineering of the barrier heights. Recently, hot carriers in plasmonic metal nanostructures have also been used to enhance solar energy conversion in photovoltaic and PEC cells. The generation and transfer of hot carriers in a metal/semiconductor heterostructure are not yet well understood. Other goals of this thesis are thus to investigate how the spatial distribution of hot-carrier photochemistry depends on local variations in the electromagnetic field intensity and how the interfacial hot-carrier transfer varies for different geometries of metal/semiconductor interfaces.

In the first project, we fabricated high-performance, Si-based metal-insulator-semiconductor (MIS) photoanodes patterned with arrays of Ni catalysts for PEC water oxidation. Using a combination of laser-write lithography and interfacial engineering, we systematically varied the size of the Ni catalysts as well as the difference in barriers heights at the inhomogeneous Schottky junction. Specifically, we introduced a stacked layer of SiO_x/Al_2O_3 that imposes a large difference in the potential barriers of the inhomogeneous junction. We demonstrate for the first time that the pinch-off regime can be successfully achieved even with microscale Ni catalysts. The pinched-off, n-Si/$SiO_{x,RCA}$/Al_2O_3/Ni photoanodes produce a high photocurrent density of 30.2 mA cm^{-2} at 1.23 V *vs*. RHE (i.e., the reversible hydrogen electrode) and a low onset potential of 0.98 V *vs.* RHE. In addition to the excellent PEC performance, the photoanodes are robust and exhibit a stable photocurrent for over 48 h in a highly corrosive alkaline solution.

The photochemistry of hot carriers is investigated using different configurations of plasmonic metal/semiconductor heterostructures that are fabricated through electron beam lithography and laser-write lithography to precisely control the size and shape of the metal nanostructures. Photodeposition is used to map hot-carrier photochemistry in plasmonic gold (Au)/ titanium oxide (TiO_2) heterostructures. The distribution of the reactivity maps obtained from photodeposition agrees with the simulated electromagnetic field intensities. The contact area between Au and Si in n-Si/Au composite electrodes is controlled using metal-assisted chemical etching, followed by characterization using atomic force microscopy and photoelectrochemical measurements. The results reveal that the doping density and crystallographic orientation of the Si substrate affect the interface geometry between the Au and Si during etching, which determines the performance of the n-Si/Au photoanode.

Chapter 1

Introduction: Metal/Semiconductor Photoelectrodes for Water Splitting and Factors Affecting Their Performance

1.1 Background

The rapid growth of the world's population has raised the concern of an energy crisis due to the depletion of fossil fuels. The combustion of fossil fuels also causes severe environmental issues, such as pollution and climate change. Therefore, finding alternative, renewable energy sources that are clean and efficient is urgent. Solar energy is one of the most attractive renewable energy resources, as approximately 120,000 terawatts (TW) of solar radiation reaches the Earth every day.[1] However, because of its seasonal and daily intermittency, full use of solar energy cannot be realized by direct solar-to-electrical energy conversion.[2] One way to overcome this problem is to efficiently convert solar energy into storable chemical fuels that can be released upon demand.[3]

Hydrogen is a promising solar-fuel candidate. It has a high energy yield and produces zero pollution because the final exhaustive product is water.[4, 5] Current hydrogen production is mainly derived from fossil fuels using methods such as natural gas reforming and coal gasification.[6, 7] In contrast, photoelectrochemical (PEC) water splitting offers a clean route to generate hydrogen by using solar energy to perform water electrolysis, where a voltage is applied to electrodes in solution to decompose water molecules into oxygen and hydrogen.[8, 9] One device configuration that can accomplish this process is composed of an n-type semiconductor photoanode and a metal cathode, as shown in **Figure 1.1**. The semiconductor photoanode absorbs light to generate energetic electrons and holes, which drive the hydrogen evolution reaction (HER) at the cathode and the oxygen evolution reaction (OER) at the anode, respectively.

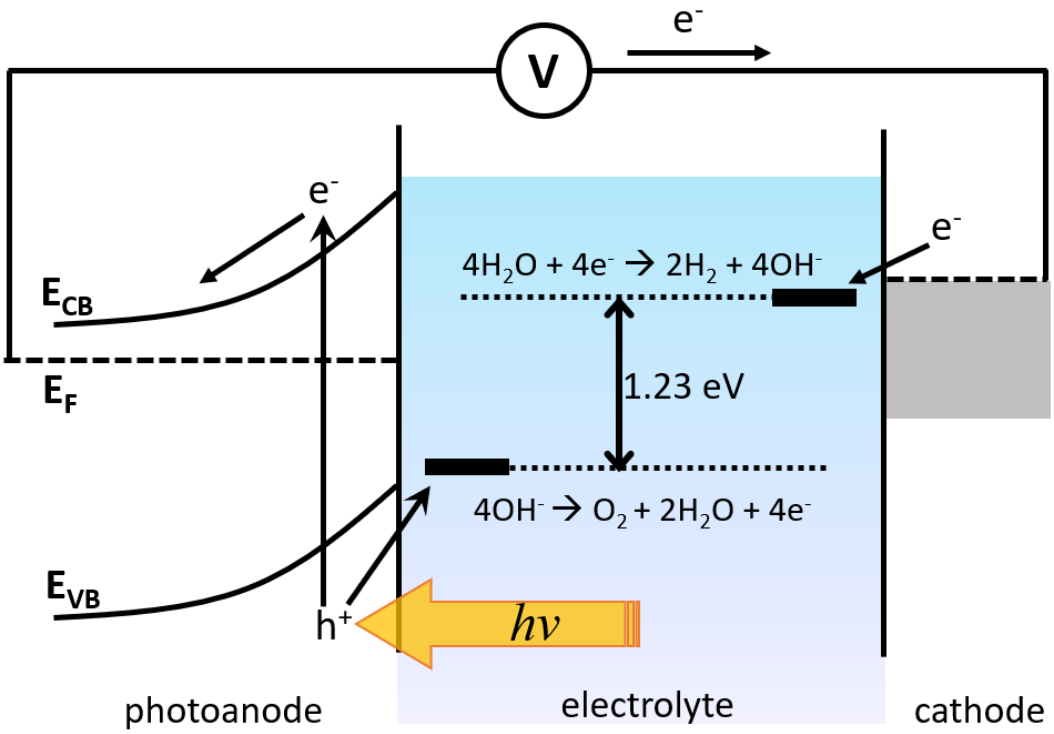

Figure 1.1 Solar water splitting using a photoelectrochemical cell.

The overall water splitting reaction, which requires a thermodynamic potential difference of 1.23 V in theory, is energetically demanding. In practice, an even higher potential (>1.8 V) is required to overcome the kinetic barriers of the half reactions at the anode and cathode.[10] As illustrated in the diagram in **Figure 1.1**, PEC water splitting involves three main steps. First, the semiconductor must absorb incident light to provide photogenerated charge carriers. Second, the semiconductor photoelectrode needs to have a sufficient photovoltage to transport the charge carriers to the electrode surface and drive the water splitting reaction. Third, water oxidation and hydrogen evolution must take place at the anode and cathode, respectively. While all three steps are important in determining the conversion efficiency of PEC water splitting, the main bottleneck is the large overpotential for water oxidation at the photoanode. The requirement to transfer 4 electrons and 4 protons in this process leads to slow reaction kinetics.[11] Thus, it is essential to

introduce an electrocatalyst at the photoanode surface to lower the overpotential for OER. Improvements in conversion efficiency are necessary to lower hydrogen production costs and achieve economic feasibility for replacing fossil fuels.

1.2 Semiconductor Photoelectrodes

Semiconductors absorb light to generate excited charge carriers. The excited electrons are directed to the conduction band, and the holes are left in the valence band. Therefore, for a semiconductor to be employed as a PEC photoelectrode, the first consideration is the semiconductor band gap energy and band edge positions. **Figure 1.2** shows the band gap energies and band edge positions of various semiconductor photoelectrodes relative to the electrode potentials for the HER and OER. An ideal semiconductor for overall water splitting should have a valence band edge located below (i.e., more positive on the NHE scale) the water oxidation potential, and the conduction band edge should be above (i.e., more negative on the NHE scale) the water reduction potential. TiO_2 was the first semiconductor to be applied for PEC water splitting by Fujishima and Honda in 1972.[12, 13] Its conduction band and valence band edge potentials straddle the water reduction and oxidation potentials, making it sufficient to perform both HER and OER.[14] However, the large band gap of TiO_2 (~3.2 eV) only allows it to absorb ultraviolet light that constitutes only about 5% of the entire solar spectrum, leading to a low photoconversion efficiency.[5] Extensive research has focused on extending the absorption spectrum of TiO_2 into the visible region. One effective strategy is to incorporate plasmonic metal nanoparticles, which will be discussed in Section 1.5.

Because it is hard to find a single semiconductor that meets all the requirements described above, a tandem semiconductor configuration is preferred to provide the photovoltage needed to perform both OER and HER. This system involves using two semiconductors, an n-type

semiconductor as the photoanode and a p-type semiconductor as the photocathode. Recent studies suggest that the optimal band gaps for the two semiconductors in a tandem system should be between 1 and 2 eV to maximize efficiency.[15, 16] To realize feasible hydrogen generation by PEC water splitting, both high-efficiency photoanodes and photocathodes need to be developed. Due to the more facile kinetics associated with the two-electron transfer needed for water reduction, the cathodic reaction can be achieved at a low overpotential with common semiconductor materials combined with HER catalysts, such as Pt.[17] However, OER at the anode is still considered the bottleneck for water splitting. Therefore, the focus of Chapter 2 is to fabricate and improve the efficiency of Si-based photoanodes that are patterned with arrays of catalysts for the OER.

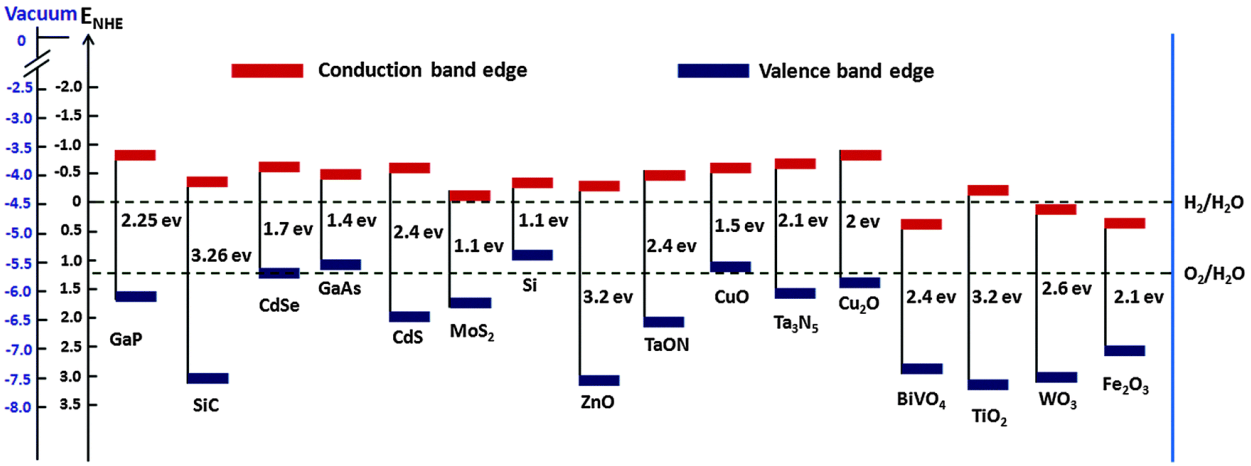

Figure 1.2 Band edge positions of various semiconductors referenced to both the NHE scale and the vacuum level. The dashed lines show the thermodynamic potentials for water reduction and water oxidation at pH = 0.[18] Reproduced from (Tamirat, A. G., Using hematite for photoelectrochemical water splitting: a review of current progress and challenges. Nanoscale Horizons **2016**, 1 (4), 243-267) with permission from the Royal Society of Chemistry.

Silicon (Si) is an attractive photoelectrode material because it is earth-abundant, has high carrier mobility, and has a small band gap (~1.1 eV) that allows it to absorb a large portion of the solar spectrum.[19] However, using Si as a photoanode is challenging for two reasons. One is the

high valence band edge position. As shown in **Figure 1.2**, the valence band edge of Si is located above water oxidation potential. Therefore, operating at a high pH with an applied potential is often required to overcome the energy level mismatch. The second problem is that the self-oxidation potential for Si (−0.99 V vs. the reversible hydrogen electrode, RHE) is very negative compared to the water oxidation potential (+1.23 V vs. RHE).[20] This results in the spontaneous passivation/corrosion of Si in aqueous solutions, especially in the alkaline pH range typically used for water oxidation.[21] Thus, in order for Si photoanodes to be used, they must be protected from the highly corrosive electrolyte solution in the electrochemical cell.

Protection strategies for stabilizing Si photoanodes typically involve eliminating the Si/electrolyte interface by coating the semiconductor with a conformal protection layer. Thin, non-catalytic passivation layers such as TiO_x, SiO_x, and Al_2O_3 have been shown to significantly improve the stability of Si photoanodes under various pH conditions, including 1 M NaOH.[22-24] Attempts have also been made to directly use metal oxides to both protect Si photoanodes and act as catalysts for OER. Nickel (Ni) is an excellent candidate for such a layer as it exhibits high chemical stability in alkaline solutions and possesses high catalytic activity for OER. Furthermore, Ni is a non-precious metal and offers a high work function for large photovoltage generation. Thin Ni films (2 nm) coated on n-type Si electrodes by electron beam evaporation exhibit high PEC activity with a low onset potential (~1.07 V vs. RHE) in 1 M KOH, and can reach a photocurrent density of 60 mW cm^{-2} under xenon lamp illumination at a light intensity equivalent to 2 suns.[25] The thin film was sufficient to form a Schottky junction with the Si semiconductor but insufficient to protect the underlying Si photoanode in 1 M KOH. The performance started to decay after 24 h of operation. Depositing thicker Ni films that are more resistant to corrosion is not plausible as it will lead to absorption loss.

From the examples described above, a stabilized photoanode with high performance can only be achieved if the following conditions are satisfied: (1) the protection layer should possess minimal defects to provide long-term stability, (2) absorption losses caused by the protection layer or electrocatalysts deposited on top of the semiconductor should be limited, (3) the protection layer should not block the transport of photogenerated charge carriers from the semiconductor but should instead be designed to ensure formation of a large Schottky barrier height. This third criterion is critical in determining the photovoltage of a photoelectrode and is currently under extensive research to achieve better performance.[26-28]

1.3 Metal-Insulator-Semiconductor (MIS) Photoanodes

The protection strategy that will be the focus of this dissertation is to construct metal-insulator-semiconductor (MIS) photoanodes, which have the potential to fulfill all three criteria listed in the previous section. First, a thin insulating layer is coated on the semiconductor to protect it from corrosion, and then a metal electrocatalyst is deposited on top. The metal layer both provides sites for electrocatalytic water oxidation and forms a Schottky junction at the MIS interface. This interface is called a Schottky barrier, and it determines the generation of photovoltage under illumination. The characteristics of the Schottky junction can affect the amount of generated photovoltage, and some of the important factors to consider will be discussed below for the development of high-performance photoanodes.

Schottky barrier height:

When the Fermi levels of the metal and semiconductor are aligned, a Schottky barrier contact is formed. For an n-type semiconductor, there will be a depletion layer in the semiconductor due to transfer of electrons to the metal, and a positive potential is formed in this

region (**Figure 1.3**).[29] This electric potential force drives minority carriers to migrate towards the interface and majority carriers away from the interface.[30] For n-type semiconductors, electrons are the majority charge carrier, and holes are the minority charge carrier. The strength of the electric field at the interface is related to the barrier height (Φ_b), which is defined as the energy difference between the band edge of majority carriers in the semiconductor and the Fermi level of metal (work function of metal, Φ_m).[31] If the barrier height is small, the driving force will be insufficient to separate electrons and holes, causing recombination of the photogenerated charge carriers, which leads to photovoltage loss. A large barrier height will provide the system with better charge separation and reduce the amount of charge recombination. Thus, to maximize the photovoltage in a photoelectrode, the selection of a semiconductor and a metal that have a large difference between their Fermi energies is critical.

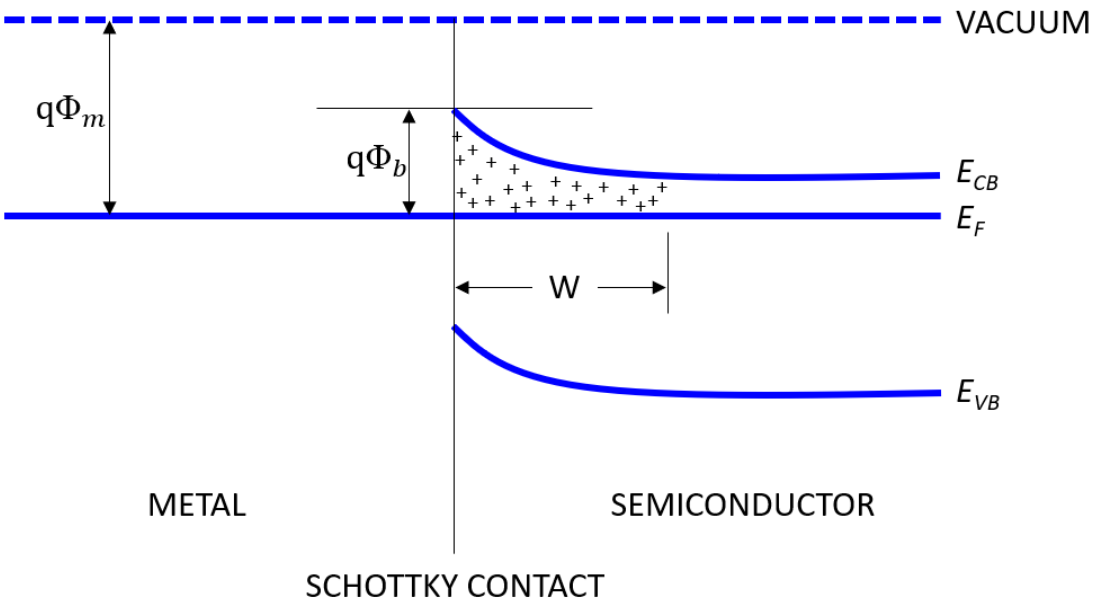

Figure 1.2 Energy band diagram of a metal, an n-type semiconductor, and the Schottky junction between them. Φ_b is the barrier height of the system. Φ_m is the work function of metal. W is the width of the depletion region.

***Surface states*:**

According to the Mott–Schottky rule, an ideal Schottky barrier has a barrier height that depends strongly on the work function of the metal. However, in many prior experimental results, the Schottky barrier height showed little dependence on the work function of metal.[31, 32] This deviation is caused by the presence of surface states between the semiconductor and metal. These states could be metal-induced gap states, which are introduced during the direct chemical bonding of the metal and semiconductor, or dangling bonds that are present at the semiconductor surface.[30, 33, 34] A high density of surface states will cause the Fermi level position of the semiconductor to be "pinned" because the Fermi energy is now aligned to the energy of the surface states rather than the work function of the metal. This phenomenon is called "Fermi-level pinning", which causes the system to have a much smaller barrier height than what would be predicted by the Mott–Schottky rule.

Insulating layer:

Another important factor that affects the properties of an MIS Schottky junction is the insulating layer at the metal/semiconductor interface. The presence of an insulator imposes a barrier for both electrons and holes to cross the interface. The insulating layer should be thin enough to allow charge carriers to tunnel through, as the tunneling probability decreases exponentially with increasing insulator thickness.[35] Insulating layers are also able to passivate surface states at the semiconductor surface.[30, 36, 37] This alleviates Fermi-level pinning and improves the photovoltage of the MIS photoelectrode. The extent of Fermi-level pinning is affected by the type of insulator and the quality of the insulating film, which depends on the process used to fabricate it.[38]

1.4 MIS Photoanodes with Inhomogeneous Barrier Heights

Studies using partially coated Si photoanodes with metal catalysts have recently emerged, as this design can maximize light absorption.[9, 20, 39, 40] Furthermore, the inhomogeneous nature of partially coated photoanodes can benefit from the pinch-off effect, generating large photovoltages for better charge separation. In the case of an n-type Si electrode decorated with metal nanoparticles, the electrode surface possesses two different barrier heights. The n-Si/metal contact has a low barrier height, while the n-Si/electrolyte interface can have a high barrier height. The pinch-off effect can occur when the metal contact size becomes smaller than the depletion width in the n-Si. In this regime, the low barrier height n-Si/metal interface will experience a higher effective barrier height imposed by the surrounding high barrier height of the n-Si/electrolyte junction.[41] This behavior was experimentally demonstrated in previous work using n-Si electrodes patterned with arrays of small Ni particles in contact with a reversible, one-electron redox couple in the electrolyte, which showed a size-dependent photovoltage as the size of the patterned Ni catalyst particles was systematically varied.[41]

In 2015, Switzer's group demonstrated a significant photovoltage improvement in Si photoanodes coated with nanoscale Co islands compared to those coated with a coalesced Co film.[37] The improvement was attributed to the inhomogeneous barrier heights produced by the discontinuous Co islands that led to the pinch-off effect. More recently, several groups have used electrodeposition to fabricate pinched-off Si photoanodes decorated with Ni nanoparticles.[9, 20, 39, 40] These studies point out the importance of a photoelectrochemical activation step for the Ni catalyst, which greatly enhances its performance for OER. The formation of a Ni/NiOOH core-shell structure after activation improves the OER kinetics.[42] More importantly, because of the increase in work function of Ni after oxidation to NiOOH, an inhomogeneous barrier height is

generated around the Ni nanoparticles, which initiates the pinch-off effect.[30, 43] While these electrodeposited pinched-off photoanodes can achieve a photovoltage close to a buried junction emitter, their stability under OER condition is still limited to below 11 h due to the small catalyst size.

1.5 Plasmonic Metal/Semiconductor Photoelectrodes

Wide band gap semiconductors can offer a sufficient driving force (E_g > 1.23 eV) for the overall water splitting reaction and are often more stable in harsh, oxidative electrolyte solutions.[14] For instance, TiO_2 is a popular material because it also has appropriate band edge positions relative to the water redox potentials. The main problem with these large band gap semiconductors is that they only absorb ultraviolet light, limiting their maximum achievable solar conversion efficiency.[5] One promising strategy to resolve this issue is to incorporate plasmonic metal nanoparticles into the semiconductor to extend their absorption range.

Surface plasmons are collective oscillations of conduction electrons in response to electromagnetic radiation. Nanoparticles of noble metals, such as gold (Au) and silver (Ag), support the formation of localized surface plasmons in response to visible light.[2, 44] After incident light excitation, surface plasmons can decay non-radiatively to generate energetic hot electron–hole pairs. When they are interfaced with a semiconductor, hot electrons can be injected into the conduction band of the semiconductor; this process is also known as plasmon-induced charge separation.[45] Because the photon energies required in this process need to be greater than the Schottky barrier height rather than the semiconductor band gap, plasmonic metal nanoparticles can be used to sensitize wide bandgap semiconductors to visible light.[46, 47] Many studies have demonstrated PEC performance enhancement in TiO_2 photoelectrodes decorated with plasmonic Au nanoparticles.[48-50]

The plasmon resonance frequency and the light-focusing properties of plasmonic nanoparticles depend largely on their size and shape.[2] Therefore, many studies have focused on tuning the size and shape of the metal nanoparticles to improve light absorption in semiconductor composite electrodes.[48, 51] Although light absorption is critical for generating charge carriers, the collection of hot carriers is also important but is often overlooked. The reported hot-carrier collection efficiency is less than 1%, which still needs a lot of improvement.[46, 52] One straightforward method to improve the collection efficiency is to embed plasmonic nanostructures into the semiconductor. Additional Schottky interfaces will be introduced when the plasmonic nanostructures are embedded, allowing a larger population of excited electrons to be extracted into the semiconductor. For example, a 25 times greater photocurrent enhancement after embedding was observed in a plasmonic Au nanowire/Si diode device.[53]

1.6 Contributions and Outline of the Dissertation

In this dissertation, we study the role of barrier height difference in initiating the pinch-off effect in Ni patterned Si photoanodes. Through the combination of laser lithography and interfacial engineering, we enabled the pinch-off effect in Si photoanodes with microscale Ni catalysts. The ability to use microscale catalysts is critical in realizing pinched-off photoanodes with both high photovoltages and high stability. This work also points out the importance of incorporating barrier height differences in the design of MIS photoanodes to exploit the pinch-off effect.

Three major metal/semiconductor photoelectrode systems are studied in this dissertation. **Chapter 2** describes how inhomogeneous barrier heights affect the performance of patterned Ni-silicon photoanodes for water oxidation. High-performance Si-based MIS photoanodes patterned with arrays of Ni catalysts for PEC water oxidation were fabricated. The barrier heights at the

inhomogeneous junction are altered through interfacial engineering, and the role of different interfacial oxide layers is determined. We demonstrate for the first time that the pinch-off regime can be successfully achieved with microscale Ni catalysts by tuning the barrier-height difference at the inhomogeneous junction. This dissertation also provides insight into the photochemistry of hot-carrier extraction in plasmonic metal/semiconductor photoelectrodes and the effect of the interface geometry on the performance of photoelectrodes. **Chapter 3** studies the spatial distribution of hot-carrier photochemistry in Au/TiO_2 heterostructures. The performance of Au/silicon photoelectrodes with different interface geometry was also investigated in this chapter and was found to be affected by the doping density and crystallographic orientation of the Si substrate.

1.7 References

1. Lewis, N. S.; Crabtree, G.; Nozik, A.; Wasielewski, M.; Alivisatos, P.; Kung, H.; Tsao, J.; Chandler, E.; Walukiewicz, W.; Spitler, M. *Basic research needs for solar energy utilization. report of the basic energy sciences workshop on solar energy utilization, April 18-21, 2005*; DOESC (USDOE Office of Science (SC)): 2005.

2. Warren, S. C.; Thimsen, E., Plasmonic solar water splitting. *Energy & Environmental Science* **2012,** *5* (1), 5133-5146.

3. Wang, Q.; Domen, K., Particulate photocatalysts for light-driven water splitting: mechanisms, challenges, and design strategies. *Chemical Reviews* **2019,** *120* (2), 919-985.

4. Wang, S.; Lu, A.; Zhong, C.-J., Hydrogen production from water electrolysis: role of catalysts. *Nano Convergence* **2021,** *8* (1), 1-23.

5. Yang, W.; Prabhakar, R. R.; Tan, J.; Tilley, S. D.; Moon, J., Strategies for enhancing the photocurrent, photovoltage, and stability of photoelectrodes for photoelectrochemical water splitting. *Chemical Society Reviews* **2019,** *48* (19), 4979-5015.

6. Selli, E.; Chiarello, G. L., Hydrogen production by photo-catalytic steam reforming of methanol on noble metal-modified titanium dioxide, In *ACS National Meeting,* **2011**.

7. Jafari, T.; Moharreri, E.; Amin, A. S.; Miao, R.; Song, W.; Suib, S. L., Photocatalytic water splitting—the untamed dream: a review of recent advances. *Molecules* **2016,** *21* (7), 900.

8. Lee, S. A.; Choi, S.; Kim, C.; Yang, J. W.; Kim, S. Y.; Jang, H. W., Si-based water oxidation photoanodes conjugated with earth-abundant transition metal-based catalysts. *ACS Materials Letters* **2019,** *2* (1), 107-126.

9. Lee, S. A.; Lee, T. H.; Kim, C.; Lee, M. G.; Choi, M.-J.; Park, H.; Choi, S.; Oh, J.; Jang, H. W., Tailored NiO x/Ni cocatalysts on silicon for highly efficient water splitting photoanodes via pulsed electrodeposition. *ACS Catalysis* **2018,** *8* (8), 7261-7269.

10. Li, X.; Zhao, L.; Yu, J.; Liu, X.; Zhang, X.; Liu, H.; Zhou, W., Water splitting: from electrode to green energy system. *Nano-Micro Letters* **2020,** *12* (1), 1-29.

11. Suen, N.-T.; Hung, S.-F.; Quan, Q.; Zhang, N.; Xu, Y.-J.; Chen, H. M., Electrocatalysis for the oxygen evolution reaction: recent development and future perspectives. *Chemical Society Reviews* **2017,** *46* (2), 337-365.

12. Fujishima, A.; Honda, K., Electrochemical photolysis of water at a semiconductor electrode. *Nature* **1972,** *238* (5358), 37-38.

13. Hisatomi, T.; Domen, K., Introductory lecture: sunlight-driven water splitting and carbon dioxide reduction by heterogeneous semiconductor systems as key processes in artificial photosynthesis. *Faraday Discussions* **2017,** *198*, 11-35.

14. Nguyen, P. D.; Duong, T. M.; Tran, P. D., Current progress and challenges in engineering viable artificial leaf for solar water splitting. *Journal of Science: Advanced Materials and Devices* **2017,** *2* (4), 399-417.

15. Cardon, F., *Photovoltaic and photoelectrochemical solar energy conversion*. Springer Science & Business Media: 2012; Vol. 69.

16. Seitz, L. C.; Chen, Z.; Forman, A. J.; Pinaud, B. A.; Benck, J. D.; Jaramillo, T. F., Modeling practical performance limits of photoelectrochemical water splitting based on the current state of materials research. *ChemSusChem* **2014,** *7* (5), 1372-1385.

17. Chen, Y.; Sun, K.; Audesirk, H.; Xiang, C.; Lewis, N. S., A quantitative analysis of the efficiency of solar-driven water-splitting device designs based on tandem photoabsorbers patterned with islands of metallic electrocatalysts. *Energy & Environmental Science* **2015,** *8* (6), 1736-1747.

18. Tamirat, A. G.; Rick, J.; Dubale, A. A.; Su, W.-N.; Hwang, B.-J., Using hematite for photoelectrochemical water splitting: a review of current progress and challenges. *Nanoscale Horizons* **2016,** *1* (4), 243-267.

19. Yang, J.; Walczak, K.; Anzenberg, E.; Toma, F. M.; Yuan, G.; Beeman, J.; Schwartzberg, A.; Lin, Y.; Hettick, M.; Javey, A., Efficient and sustained photoelectrochemical water oxidation by cobalt oxide/silicon photoanodes with nanotextured interfaces. *Journal of the American Chemical Society* **2014,** *136* (17), 6191-6194.

20. Oh, K.; Mériadec, C.; Lassalle-Kaiser, B.; Dorcet, V.; Fabre, B.; Ababou-Girard, S.; Joanny, L.; Gouttefangeas, F.; Loget, G., Elucidating the performance and unexpected stability of partially coated water-splitting silicon photoanodes. *Energy & Environmental Science* **2018,** *11* (9), 2590-2599.

21. Sun, K.; McDowell, M. T.; Nielander, A. C.; Hu, S.; Shaner, M. R.; Yang, F.; Brunschwig, B. S.; Lewis, N. S., Stable solar-driven water oxidation to O_2 (g) by Ni-oxide-coated silicon photoanodes. *The Journal of Physical Chemistry Letters* **2015,** *6* (4), 592-598.

22. Chen, Y. W.; Prange, J. D.; Dühnen, S.; Park, Y.; Gunji, M.; Chidsey, C. E.; McIntyre, P. C., Atomic layer-deposited tunnel oxide stabilizes silicon photoanodes for water oxidation. *Nature Materials* **2011,** *10* (7), 539-544.

23. Hu, S.; Shaner, M. R.; Beardslee, J. A.; Lichterman, M.; Brunschwig, B. S.; Lewis, N. S., Amorphous TiO_2 coatings stabilize Si, GaAs, and GaP photoanodes for efficient water oxidation. *Science* **2014,** *344* (6187), 1005-1009.

24. Scheuermann, A. G.; Lawrence, J. P.; Meng, A. C.; Tang, K.; Hendricks, O. L.; Chidsey, C. E.; McIntyre, P. C., Titanium oxide crystallization and interface defect passivation for high performance insulator-protected schottky junction MIS photoanodes. *ACS Applied Materials & Interfaces* **2016,** *8* (23), 14596-14603.

25. Kenney, M. J.; Gong, M.; Li, Y.; Wu, J. Z.; Feng, J.; Lanza, M.; Dai, H., High-performance silicon photoanodes passivated with ultrathin nickel films for water oxidation. *Science* **2013,** *342* (6160), 836-840.

26. Ji, L.; McDaniel, M. D.; Wang, S.; Posadas, A. B.; Li, X.; Huang, H.; Lee, J. C.; Demkov, A. A.; Bard, A. J.; Ekerdt, J. G., A silicon-based photocathode for water reduction with

an epitaxial SrTiO 3 protection layer and a nanostructured catalyst. *Nature Nanotechnology* **2015,** *10* (1), 84-90.

27. Jung, J.-Y.; Yu, J.-Y.; Shinde, S. S.; Kim, S.-H.; Kim, D.-H.; Lin, C.; Wehrspohn, R. B.; Lee, J.-H., Remarkable improvements in the performance and stability of Si photoanodes adopting nanocrystalline NiOx electrocatalyst and stoichiometric SiO_2 protection. *Applied Surface Science* **2019,** *493*, 1150-1158.

28. Hu, S.; Lewis, N. S.; Ager, J. W.; Yang, J.; McKone, J. R.; Strandwitz, N. C., Thin-film materials for the protection of semiconducting photoelectrodes in solar-fuel generators. *The Journal of Physical Chemistry C* **2015,** *119* (43), 24201-24228.

29. Kasap, S. O., *Principles of Electronic Materials and Devices*. McGraw-Hill New York: **2006**; Vol. 2.

30. Digdaya, I. A.; Adhyaksa, G. W.; Trześniewski, B. J.; Garnett, E. C.; Smith, W. A., Interfacial engineering of metal-insulator-semiconductor junctions for efficient and stable photoelectrochemical water oxidation. *Nature Communications* **2017,** *8* (1), 1-8.

31. Tung, R. T., The physics and chemistry of the Schottky barrier height. *Applied Physics Reviews* **2014,** *1* (1), 011304.

32. Farmanbar, M.; Brocks, G., Controlling the Schottky barrier at MoS_2/metal contacts by inserting a BN monolayer. *Physical Review B* **2015,** *91* (16), 161304.

33. Mönch, W., On the alleviation of Fermi-level pinning by ultrathin insulator layers in Schottky contacts. *Journal of Applied Physics* **2012,** *111* (7), 073706.

34. Cowley, A.; Sze, S., Surface states and barrier height of metal-semiconductor systems. *Journal of Applied Physics* **1965,** *36* (10), 3212-3220.

35. Hemmerling, J.; Quinn, J.; Linic, S., Quantifying Losses and Assessing the Photovoltage Limits in Metal–Insulator–Semiconductor Water Splitting Systems. *Advanced Energy Materials* **2020,** *10* (12), 1903354.

36. Dingemans, G.; Kessels, W., Status and prospects of Al_2O_3-based surface passivation schemes for silicon solar cells. *Journal of Vacuum Science & Technology A: Vacuum, Surfaces, and Films* **2012,** *30* (4), 040802.

37. Hill, J. C.; Landers, A. T.; Switzer, J. A., An electrodeposited inhomogeneous metal–insulator–semiconductor junction for efficient photoelectrochemical water oxidation. *Nature Materials* **2015,** *14* (11), 1150-1155.

38. Digdaya, I. A.; Trześniewski, B. J.; Adhyaksa, G. W.; Garnett, E. C.; Smith, W. A., General considerations for improving photovoltage in metal–insulator–semiconductor photoanodes. *The Journal of Physical Chemistry C* **2018,** *122* (10), 5462-5471.

39. Xu, G.; Xu, Z.; Shi, Z.; Pei, L.; Yan, S.; Gu, Z.; Zou, Z., Silicon photoanodes partially covered by $Ni@Ni(OH)_2$ core–shell particles for photoelectrochemical water oxidation. *ChemSusChem* **2017,** *10* (14), 2897-2903.

40. Loget, G.; Fabre, B.; Fryars, S.; Meriadec, C.; Ababou-Girard, S., Dispersed Ni nanoparticles stabilize silicon photoanodes for efficient and inexpensive sunlight-assisted water oxidation. *ACS Energy Letters* **2017,** *2* (3), 569-573.

41. Rossi, R. C.; Lewis, N. S., Investigation of the size-scaling behavior of spatially nonuniform barrier height contacts to semiconductor surfaces using ordered nanometer-scale nickel arrays on silicon electrodes. *The Journal of Physical Chemistry B* **2001,** *105* (49), 12303-12318.

42. Oh, S.; Oh, J., High performance and stability of micropatterned oxide-passivated photoanodes with local catalysts for photoelectrochemical water splitting. *The Journal of Physical Chemistry C* **2016,** *120* (1), 133-141.

43. Laskowski, F. A.; Oener, S. Z.; Nellist, M. R.; Gordon, A. M.; Bain, D. C.; Fehrs, J. L.; Boettcher, S. W., Nanoscale semiconductor/catalyst interfaces in photoelectrochemistry. *Nature Materials* **2020,** *19* (1), 69-76.

44. Linic, S.; Christopher, P.; Ingram, D. B., Plasmonic-metal nanostructures for efficient conversion of solar to chemical energy. *Nature Materials* **2011,** *10* (12), 911-921.

45. Tian, Y.; Tatsuma, T., Mechanisms and applications of plasmon-induced charge separation at TiO2 films loaded with gold nanoparticles. *Journal of the American Chemical Society* **2005,** *127* (20), 7632-7637.

46. Knight, M. W.; Sobhani, H.; Nordlander, P.; Halas, N. J., Photodetection with active optical antennas. *Science* **2011,** *332* (6030), 702-704.

47. Smith, J. G.; Faucheaux, J. A.; Jain, P. K., Plasmon resonances for solar energy harvesting: a mechanistic outlook. *Nano Today* **2015,** *10* (1), 67-80.

48. Kim, H. J.; Lee, S. H.; Upadhye, A. A.; Ro, I.; Tejedor-Tejedor, M. I.; Anderson, M. A.; Kim, W. B.; Huber, G. W., Plasmon-enhanced photoelectrochemical water splitting with size-controllable gold nanodot arrays. *ACS Nano* **2014,** *8* (10), 10756-10765.

49. Rayalu, S. S.; Jose, D.; Joshi, M. V.; Mangrulkar, P. A.; Shrestha, K.; Klabunde, K., Photocatalytic water splitting on Au/TiO_2 nanocomposites synthesized through various routes: enhancement in photocatalytic activity due to SPR effect. *Applied Catalysis B: Environmental* **2013,** *142*, 684-693.

50. DeSario, P. A.; Pietron, J. J.; DeVantier, D. E.; Brintlinger, T. H.; Stroud, R. M.; Rolison, D. R., Plasmonic enhancement of visible-light water splitting with Au–TiO_2 composite aerogels. *Nanoscale* **2013,** *5* (17), 8073-8083.

51. Yen, Y.-C.; Chen, J.-A.; Ou, S.; Chen, Y.-S.; Lin, K.-J., Plasmon-enhanced photocurrent using gold nanoparticles on a three-dimensional TiO_2 nanowire-web electrode. *Scientific Reports* **2017,** *7* (1), 1-8.

52. Mubeen, S.; Lee, J.; Singh, N.; Krämer, S.; Stucky, G. D.; Moskovits, M., An autonomous photosynthetic device in which all charge carriers derive from surface plasmons. *Nature Nanotechnology* **2013,** *8* (4), 247-251.

53. Knight, M. W.; Wang, Y.; Urban, A. S.; Sobhani, A.; Zheng, B. Y.; Nordlander, P.; Halas, N. J., Embedding plasmonic nanostructure diodes enhances hot electron emission. *Nano Letters* **2013,** *13* (4), 1687-1692.

Chapter 2

Interfacial Engineering of The Barrier Height in Patterned Nickel-Silicon Photoanodes for Efficient Photoelectrochemical Water Oxidation

2.1 Introduction

Photoelectrochemical (PEC) water splitting is a promising approach to solar-to-chemical energy conversion and has been envisioned as a sustainable method to provide a clean and renewable energy source.[1-3] A PEC water-splitting cell consists of a photocathode and a photoanode that can perform reduction and oxidation of water simultaneously to generate hydrogen and oxygen, respectively. Silicon is one of the most attractive semiconductors for photoelectrodes because it has a small bandgap (1.12 eV) that can absorb a significant portion of the solar spectrum and high carrier mobilities that enable the efficient extraction of the photoexcited carriers.[4, 5] Moreover, Si is earth-abundant and is widely used in the photovoltaic industry, making its refining relatively low in cost and trending down over the last decade.[6] However, the development of efficient Si-based photoanodes is particularly challenging, because of i) the kinetically sluggish oxygen evolution reaction (OER) at the silicon/electrolyte interface[7, 8] and ii) the instability of Si in aqueous solutions.[9-11] The latter problem is especially pronounced in alkaline solutions, which is the favorable condition for OER. Tremendous research has been done to overcome these crucial problems, with most strategies involving the combination of a conformal protection layer that eliminates the Si/electrolyte interface and an OER co-catalyst that improves the kinetics for OER.[7, 12-15] Conformal layers are effective in providing long-term stability for Si photoanodes in strongly alkaline solution but can cause series resistance in the junction and/or block the incident light leading to absorption loss.[4, 14, 16]

Recently, alternative approaches based on lithographic patterning or electrodeposition of metal particle catalysts on the surface of Si have been used to prepare partially coated Si-photoanodes designed to maximize light absorption while minimizing the resistance for charge collection. Specifically, Si-photoanodes with electrodeposited metal nanoparticles have drawn

significant attention because of the large photovoltage they can achieve through the pinch-off effect without the need for a buried-junction emitter. The pinch-off effect results from inhomogeneous barrier heights between the semiconductor/electrolyte and semiconductor/catalyst interfaces. The high barrier height of the n-Si/electrolyte interface (Φ_b^0) induces a large depletion region surrounding the low barrier height of the n-Si/metal nano-contact (Φ_b^M) that increases the total effective barrier between the semiconductor and catalyst and enhances charge separation.[17] Switzer's group reported Si-photoanodes with electrodeposited nanoscale Co islands exhibiting a surprisingly large photovoltage of 470 mV.[18] More recently, other groups have reported similar photovoltage enhancements in Si photoanodes decorated with electrodeposited Ni nanoparticles due to the strengthened pinch-off effect when the contact area of the Ni catalysts is much smaller than the depletion width in the n-Si photoanode.[3, 11, 19] Despite the high performance of partially coated Si-photoanodes that operate in the pinch-off regime, their stability during the OER is poor with a noticeable decay in photocurrent within 10 h (**Table 2.1**). The deterioration arises because etching of the Si surface in strongly alkaline solution used for OER leads to undercutting of the nanoscale catalysts.

Micrometer or sub-micrometer scale metal catalysts that are lithographically patterned on Si as periodic arrays can successfully reduce parasitic absorption while still maintaining high stability that is comparable to conformal, thin-film protected Si photoanodes. For example, buried-junction np^+-Si photoanodes patterned with Ni patches that are 5.6 μm in size, exhibit stable oxygen evolution for over 240 h of continuous operation in 1M KOH.[20] While these metal-patterned Si photoanodes also contain inhomogeneous barrier heights, they do not operate in the pinch-off regime because they are typically patterned by conventional photolithography, which limits the diameter of each catalyst region to be larger than 5 μm. Without the benefit of the pinch-

off effect, the Si-photoanodes patterned with arrays of microscale catalysts required in almost all cases a pre-formed buried junction to improve the photovoltage (**Table 2.1**).[15, 20, 21]

Table 2.1 Comparison of the water-oxidation performance of Si-based photoanodes with inhomogeneous barrier heights

Photoanodes not in the pinch-off regime						
Photoanodes	**Method**	**V_{onset} (V)[a]**	**$J_{1.23\ V}$ (mA cm^{-2})**	**Stability time[b]**	**J_{max} (mA cm^{-2})**	**Catalyst size**
np^{+}-Si/Ni[20]	Photolithography & sputtering deposition	1	12.7	200 h	20.4	5.6 µm
np^{+}-Si/Au/NiFe IO (inverse opal)[21]	Photolithography & electrophoretic deposition	0.94	31.2	> 11 h	32.5	20 µm
np^{+}-Si/SiO$_x$/Ti/Ni[15]	Photolithography & sputtering deposition	1	22.5	> 24 h	27	6 µm
np^{+}-Si/SiO$_x$/NiFe[22]	Electrodeposition	0.89	30.7	13 h	30.7	15 nm
Photoanodes in the pinch-off regime						
Photoanodes	**Method**	**V_{onset} (V)[a]**	**$J_{1.23\ V}$ (mA cm^{-2})**	**Stability time[b]**	**J_{max} (mA cm^{-2})**	**Catalyst size**
n-Si/SiO$_x$/Co/CoOOH[18]	Electrodeposition	1.1	13.1	2 h	35	21 nm
n-Si/SiO$_x$/Ni[19]	Electrodeposition	1.1	3.5	10 h	33	59 nm
n-Si/SiO$_x$/Ni@Ni(OH)$_2$[23]	Electrodeposition	1.03	15.5	N/A	36.4	200–300 nm
n-Si/SiO$_x$/Ni[11]	Electrodeposition	1.18	7.8	11 h	27.9	60 nm
n-Si/Ni/NiO$_x$[3]	Electrodeposition	1.08	14.7	3 h	31.7	< 50 nm
n-Si/NiSi$_x$/NiO$_x$ n-Si/NiSi$_x$/NiO$_x$/Au-NPs[24]	Pulsed laser deposition	1.01 0.88	10 35	6 h 10 h	31.42 37.03	Ni:11 nm Au:20 nm
n-Si/SiO$_x$/Al$_2$O$_3$/Ni (This work)	Laser-write lithography & sputtering deposition	0.98	30.2	> 48 h	35	1.5 µm

[a] V *vs.* RHE at 1 mA cm^{-2}. [b] Photocurrent stability time in 1 M KOH/NaOH.

It is known that the extent of the pinch-off effect in a system with an inhomogeneous barrier height is largely determined by both the contact size of the metal catalyst and the difference in potential barriers between the metal (Φ_b^M) and metal-free (Φ_b^0) regions. However, to date, only the size effect of pinched-off Si photoanodes for water oxidation has been extensively studied and solely based on electrodeposited Si-photoanodes.[17] There is a lack of studies on Si-photoanodes that utilize the pinch-off effect by tuning the potential barriers in metal-insulator-semiconductor (MIS) junctions with inhomogeneous barrier heights. This is in part because metal nanoparticles cannot be electrodeposited on silicon substrates with a pre-formed thin oxide layer which limits the tunability of the MIS junction potential in these systems.

Herein, we demonstrate highly stable Si photoanodes patterned with Ni by constructing a novel, inhomogeneous MIS junction that operates in the pinch-off regime for efficient PEC water oxidation. In this model system, arrays of Ni catalysts with a size of 1.5 μm are patterned on n-Si substrates by direct laser-write lithography. Laser-write lithography enables precise control of both the size and coverage of the patterned catalyst and produces catalysts dimensions that are smaller than those typically made by photolithography. Inhomogeneous barrier heights at the two interfaces, Φ_b^0 and Φ_b^M, are tuned independently by depositing or etching interfacial oxide layers in combination with laser-write lithography. The effect of different interfacial oxide layers on Fermi-level pinning was elucidated by using three different configurations of MIS photoanodes. The Ni coverage on the Si photoanodes was optimized to provide the highest photocurrent density. Specifically, we introduced a SiO_x/Al_2O_3 stacked layer that imposes a large difference in the potential barriers of the inhomogeneous junction and demonstrate for the first time that the pinch-off regime can be successfully achieved even with microscale Ni catalysts. Pinched-off, n-$Si/SiO_{x,RCA}/Al_2O_3/Ni$ photoanodes produce a high photocurrent density of 30.2 mA cm^{-2} at 1.23 V

vs. RHE and a low onset potential for the OER of 0.98 V *vs*. RHE. In addition to the excellent PEC performance, the photoanodes are robust and exhibit a stable photocurrent for over 48 h in a highly corrosive alkaline solution.

2.2 Experimental

2.2.1 Materials & Fabrication of Ni microarray-patterned Si Photoelectrodes

Chemicals:

Hydrogen peroxide (H_2O_2, with inhibitor, 30% (w/w) in H_2O), hydrochloric acid (HCl, ACS reagent, 37%), potassium hexacyanoferrate(III) ($K_3Fe(CN)_6$, ACS reagent ≥ 99.0%), potassium hexacyanoferrate(II) trihydrate ($K_4Fe(CN)_6 \cdot 3H_2O$, ACS reagent, 98.5 – 102.0%), potassium hydroxide (KOH, ACS reagent, ≥ 85%), and potassium chloride (KCl, ACS reagent, ≥ 99.0%) were purchased from Millipore Sigma/Sigma-Aldrich. Sulfuric acid (H_2SO_4 ≥ 98%, AR ACS) was purchased from VWR. Buffer HF Improved (fluoride – bifluoride hydrofluoric acid buffer) was purchased from the Transene Company, Inc. LOR10B resist, Remover PG, and MF-319 developer were purchased from MicroChem Corp. S1805 positive photoresist was purchased from the Dow Chemical Company. Single-crystal, n-type Si wafers with the (111) orientation (phosphorous-doped, single-side polished, and a resistivity range of 1 to 10 Ω cm) were purchased from MTI Corporation. Single-crystal, p+-type Si wafers with the (111) orientation (boron-doped, single-side polished, and a resistivity range of 0 to 0.003 Ω cm) were purchased from University Wafer. All chemicals were used as received. Deionized (DI) water with a resistivity of 18.2 MΩ cm was supplied from a Barnstead GenPure Pro water purification system.

Preparation of substrates:

Bare silicon wafers were first cleaned using Piranha solution consisting of 3:1 H_2SO_4:H_2O_2 (by volume) at 120°C for 20 minutes to remove particles and organic residue. The wafers were then immersed in a buffered HF oxide etchant at room temperature for 1 min to remove the native oxide on the silicon surface. Immediately after this step, the wafers were placed in a standard RCA SC-2 solution made up of 5:1:1 H_2O:HCl:H_2O_2 (by volume) at 80°C for 15 minutes. The HCl concentration was 37 wt.%. Between each step, the wafers were vigorously rinsed with deionized water and blow-dried using a stream of N_2 gas. After the SC-2 cleaning step, a thin, passivating oxide layer forms on the wafer surface, protecting it from contamination before subsequent processing.

Atomic-layer deposition of aluminum oxide:

Atomic layer deposition (ALD) of aluminum oxide (Al_2O_3) was conducted in a Veeco Savannah S100 Thermal ALD system using trimethylaluminum and water vapor as precursors. During the ALD process, the silicon substrate is exposed to precursors in alternating pulses, and purging is performed between each pulse to prevent the precursors from reacting with each other in the gas phase. Before ALD deposition, substrates were placed in the reactor chamber and pumped down to a base pressure of ~5×10^{-2} Torr. The system was stabilized for another 10 min and heated to 200°C. One ALD cycle consisted of a 0.015-s pulse of trimethylaluminum, a 5-s N_2 purge at 20 sccm, a 0.015-s pulse of H_2O, and another 5-s N_2 purge at 20 sccm. A total of 12 cycles were deposited on Si wafers that were cleaned as described above. The thicknesses of the deposited Al_2O_3 films were characterized by ellipsometry (J.A. Woollam alpha-SE) using dielectric models of Al_2O_3 and native silicon oxide on a silicon substrate.

Photoresist-patterning on silicon samples:

Arrays of Ni disks with diameters ranging from 1 to 5 μm and Ni squares with an edge length of 5 μm were patterned on Si substrates by direct laser-write lithography. The first step was to transfer the pattern mask onto the photoresist by using a Heidelberg DWL 66^+ laser writer, equipped with a 375-nm UV laser. Patterns were designed with computer-aided design (CAD) software (R.47.0.0 AutoCAD 2021). The digital pattern file was then converted to writing-path code, which directs the laser to areas on the substrate to expose the photoresist. After exposure, a development step was carried out to reveal the transferred pattern mask on the photoresist.

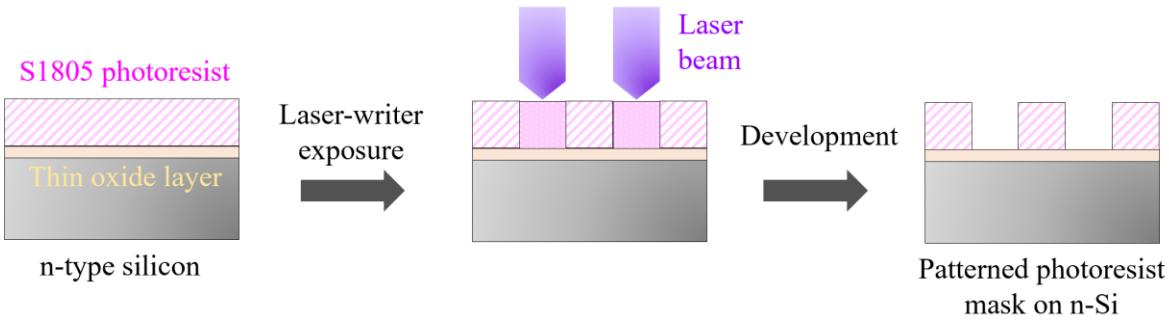

Figure 2.1 Schematic showing the process of preparing a patterned photoresist mask on a silicon substrate by laser-write lithography.

In our experiments, the patterned photoresist mask was developed as shown in **Figure 2.1**. First, a positive photoresist (S1805) was spin-coated onto the silicon substrate at 4000 rpm for 50 s (10-s dispersal at 500 rpm) and then baked at 115°C for 1 minute on a hot plate. The substrate was then placed inside the laser-writer chamber and exposed by the laser writer locally where the patterns were assigned. The exposure parameters for the mask were 10% focus, 100% intensity, 47-mW laser power, and 1% filter. The typical area for a pattern was 0.09 cm^{-2} (3 mm × 3 mm), which was used to make an individual photoelectrode. The patterns on the Si substrate had a center-

to-center separation of 5 mm. The exposed photoresist was developed by immersing it in MIF-319 developer for 60 s. After development, the substrate was thoroughly rinsed using deionized H_2O and blow-dried gently with N_2 gas.

Ni metal film deposition

Ni films were deposited from a Ni target (99.999%, Kurt J. Lesker) onto the photoresist-patterned silicon substrates by DC magnetron sputtering in a physical vapor deposition system (Kurt J. Lesker PVD 75). Immediately after the reactive ion etching (RIE) step performed on some samples (described further below), samples were transferred to the sputtering chamber to minimize the surface oxidation of Si in air. Before Ni deposition, the chamber was pumped down to reach a base pressure below 2×10^{-6} Torr. During deposition, the DC power was maintained at 180 W, which gives a deposition rate of approximately 1.3 Å/s. The deposition time was 343 s to obtain a 40-nm thick Ni film unless stated otherwise. Following deposition of the Ni layer, lift-off was conducted by immersing the sample in Remover PG overnight, followed by sonication in a new solution of Remover PG for 20 s. After lift-off, the substrate was thoroughly rinsed using deionized H_2O and blow-dried with N_2 gas.

Ni-patterned Si photoanodes with different metal-insulator-semiconductor (MIS) configurations

Using a combination of laser-write lithography and anisotropic, dry etching, we fabricated Ni-patterned Si photoelectrodes with different interfacial layers between the Si substrate and Ni catalyst. **Figure 2.2** demonstrates the configurations and fabrication processes of the three types of Ni-patterned Si photoelectrodes used in this research. The first type in **Figure 2.2 a**, was prepared directly using a n-type Si substrate that had a native oxide layer on its surface. The

photoresist mask was patterned over the native oxide layer, and Ni metal was then deposited through the mask. The photoresist was removed in the final lift-off step to prepare Ni-patterned Si photoelectrodes with an interfacial native oxide layer, which are denoted as n-Si/$SiO_{x,native}$/Ni.

For the fabrication of n-Si/Ni electrodes without the interfacial oxide layer between the Ni/Si interface as shown in **Figure 2.2 b**, photoresist-patterned silicon substrates were placed in an Oxford Plasmalab 100 inductively coupled plasma (ICP) etcher before Ni deposition. Reactive ion etching (RIE) was performed for 10 s under a chamber pressure of 15 mTorr, with 10 W RF power and 700 W ICP power, while flowing 10 sccm of CF_4 and 50 sccm of Ar to locally expose the Si surface in regions not covered by the photoresist mask. The etching is highly anisotropic and efficiently removes the native oxide on the silicon substrate without affecting the patterned photoresist. The SiO_2 etch rate using these parameters was estimated to be ~1 nm/s by measuring the thickness of SiO_2 films prepared by chemical vapor deposition (Oxford PECVD) on n-type Si(100) substrates followed by RIE. The initial thickness of the thermal SiO_2 layer before etching was ~54 nm, and the thickness after different etch times were measured by ellipsometry (J.A. Woollam alpha-SE). The deposition of Ni on these patterned substrates without the oxide layer was the same as described above. These photoanodes are denoted as n-Si/Ni below.

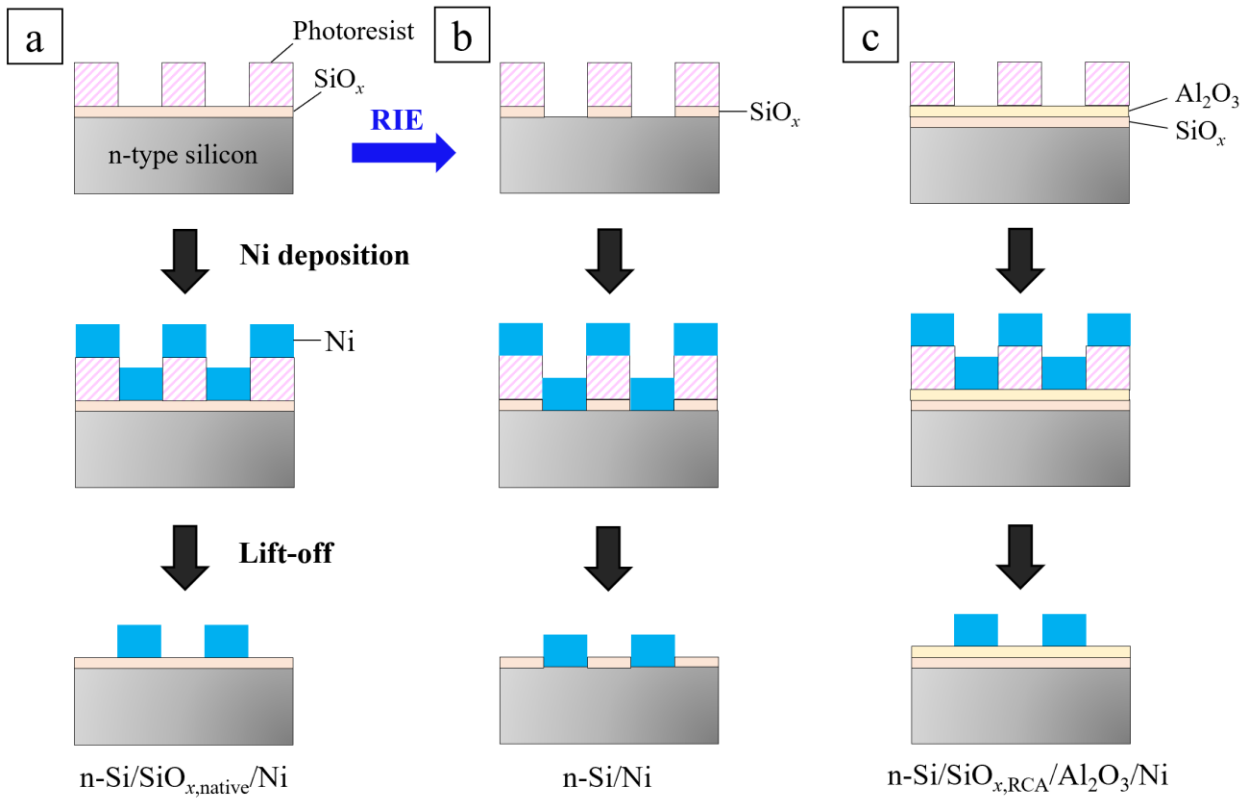

Figure 2.2 Schematic showing the processes of preparing Ni-patterned Si photoanodes with different MIS configurations. (a) n-Si/$SiO_{x,native}$/Ni photoanode (b) n-Si/Ni photoanode (c) n-Si/$SiO_{x,RCA}$ /Al_2O_3/Ni photoanode.

The third type of photoelectrode with interfacial layers of both silicon oxide and aluminum oxide is shown in **Figure 2.2 c**. The native oxide layer on the n-Si substate was first stripped by immersing it in HF and then immersing it in a RCA SC-2 solution to regrow a uniform thermal silicon oxide layer ($SiO_{x,RCA}$) as described above. An aluminum oxide layer was then deposited on the silicon oxide surface by ALD. The preparation of the photoresist mask and the Ni deposition process were identical to the first MIS configuration. The resultant Ni-patterned Si photoelectrodes possessed two interfacial oxide layers consisting of silicon oxide and aluminum oxide and are denoted as n-Si/$SiO_{x,RCA}$/Al_2O_3/Ni.

2.2.2 Electrochemical Measurements

Si photoelectrode preparation:

Each patterned silicon wafer was cut using a diamond scribe to isolate individual 3 mm × 3 mm patterned regions for fabrication into photoelectrodes. In–Ga eutectic alloy was scratched into the backside of each Si substrate with a diamond scribe to make electrical contact. A coiled tinned copper wire was pressed into the eutectic and then covered with conductive silver paint (SPI Supplies) to seal the wire to the Si substrate. The Cu wire was threaded through a glass tube, with the Si substrate oriented such that the surface normal direction of the Si substrate was perpendicular to the glass tube (see **Figure 2.3**). The backside and edges of the Si substrate, along with the exposed portion of the Cu wire, were sealed with epoxy (LOCTITE Hysol 9460™). The epoxy was also used to cover the non-patterned portions of the front side of the Si substrate, leaving only the Ni-patterned region of the electrode exposed. The epoxy was dried for 2 h in a furnace at ~60°C. The Cu wire at the other end of the glass tube was connected to the potentiostat with an alligator clip. The exposed area of each electrode was measured by scanning an image of the electrode along with a ruler and analyzing the image using ImageJ software. The typical exposed electrode area was approximately 0.1 cm^2. For plots of current density vs. potential (*J*-*E*) reported in this work, *J* represents the current density normalized to the geometric area of the exposed region of the Si electrode.

Photoelectrochemical measurements

Electrochemical measurements were conducted in a custom electrochemical cell. A schematic of the cell is shown in **Figure 2.3**. The cell was made from borosilicate glass with three 14/20 ground glass joints at the top designed for a three-electrode configuration and a flat window

on the side for illumination. Pt gauze was used as the counter electrode. The Pt gauze was attached to a Pt wire that was soldered to a tinned Cu wire, and the soldered joint was sealed in a glass tube. A mercury/mercury oxide (Hg/HgO in 4.24 M KOH (aq), Pine Research Instrumentation) electrode was used as the reference electrode. Photoelectrochemical measurements were performed in an aqueous solution of 1.0 M KOH, and the solution was continuously stirred with a magnetic stir bar at the bottom of the electrochemical cell. The Hg/HgO electrode was calibrated using a silver/silver chloride (Ag/AgCl, in 3 M NaCl, BASi) electrode, and the measured potentials were converted into potentials versus the reversible hydrogen electrode (RHE) using the following relation:

$$E\ (\text{vs. RHE}) = E\ (\text{vs. Hg/HgO}) + 0.098 + 0.059\text{pH}$$

Compensation for the series resistance of the solution was not included in the data reported in this work. Broadband ELH-type and ENH-type (Osram) halogen bulbs with custom housings were used as the illumination source for *J-E* measurements and long-term stability tests for water oxidation, respectively. Before each experiment, the illumination intensity at the working electrode was measured and adjusted accordingly by placing a calibrated Si photodiode (FDS100-Cal, Thor Labs) into the electrochemical cell at the same location as the working electrode (facing the optical window of the electrochemical cell). The current measured from the photodiode under illumination with an ELH bulb was converted into an irradiance based on the active area (3.6 × 3.6 mm) of the photodiode and the integrated, wavelength-dependent responsivity of the ELH lamp. A typical current reading was 5.25 mA, which corresponds to a light intensity of 100 mW cm^{-2}. For light intensity-dependent studies, the irradiance was adjusted by inserting a series of neutral density filters in between the electrochemical cell and the ELH lamp.

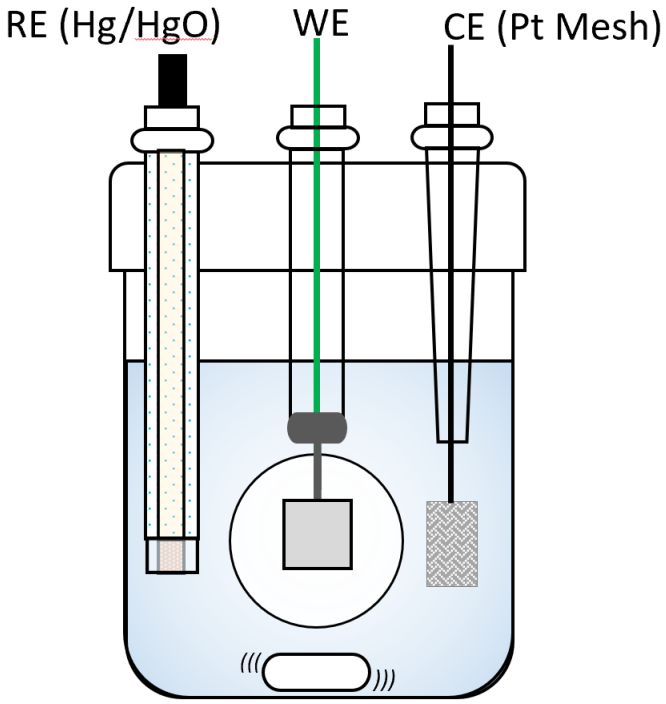

Figure 2.3 Schematic of the electrochemical cell used in photoelectrochemical testing of Ni-patterned Si photoanodes. RE: reference electrode, WE: working electrode, CE: counter electrode.

Cyclic voltammetry (CV), linear sweep voltammetry (LSV), chronoamperometry, and electrochemical impedance spectroscopy (EIS) were all performed using a BioLogic VSP-300 potentiostat/galvanostat. All CV scans started at open circuit, were first swept in the positive direction to a potential of +1.6 V vs. Hg/HgO, and were then swept in the negative direction to -0.4 V. The scan rate was 100 mV s^{-1}. The Ni catalyst arrays on all Si photoanodes were first activated by running 50 consecutive CV cycles from -0.4 V to 1.6 V vs. Hg/HgO at 100 mV s^{-1} under illumination with an ELH lamp at an irradiance of 100 mW cm^{-2}. LSV scans were recorded at a scan rate of 20 mV s^{-1} from -0.4 V to 1.6 V vs. Hg/HgO. Before each LSV scan, the solution was purged with nitrogen for 10 min.

Si photoanode water-oxidation stability measurements:

Chronoamperometric stability measurements were performed in a 1.0 M KOH electrolyte solution under illumination with an ENH-type, halogen lamp at a light intensity of 100 mW cm^{-2} using a constant potential of 1.73 V versus RHE. A variable transformer was connected to the ENH lamp to lower the power supplied to the bulb to between 40 and 50 V_{ac}, which prevents the bulb from overheating and burning out during continuous operation. During the measurement, the solution was continuously stirred and purged with nitrogen. The electrochemical cell was cooled by continuously blowing compressed air around the cell. The electrolyte in the cell was changed every 24 h to minimize changes in the KOH (aq) concentration and the build-up of gas bubbles on the surface of the electrodes. The light intensity at the working electrode was calibrated each time after the electrolyte was replaced.

Electrochemical impedance spectroscopy (EIS):

EIS of the Si photoanodes was performed in the dark in an aqueous solution of 1 M KCl, 0.05 M $K_3Fe(CN)_6$, and 0.35 M $K_4Fe(CN)_6$. Similar to the photoelectrochemical measurements, Pt gauze was used as the counter electrode, and Hg/HgO was used as the reference electrode. The frequency range was scanned from 200 kHz to 200 Hz with an AC amplitude of 10 mV. The DC potential range was 1.3 V to 0.3 V vs. Hg/HgO.

2.2.3 Details of Sample Characterization

Scanning electron microscopy (SEM) images were collected using a Thermo Scientific Quattro Environmental Scanning Electron Microscope operated at an acceleration voltage of 15 kV. The diameter and surface morphology of the patterned Ni catalysts before and after photoelectrochemical measurements were imaged using SEM. To examine the morphology of a

Si photoanode after testing its stability for water oxidation, the portion of the epoxy-coated Cu wire was cut to detach the Si substrate for the rest of the electrode. A razor blade was used to scrape off the epoxy covering the copper wire, and carbon tape was used to connect the exposed wire to the SEM sample holder.

High-resolution transmission electron microscopy (HRTEM) using a JEOL JEM-2100F field-emission microscope was performed to examine the cross-section of a n-Si/$SiO_{x,RCA}$/Al_2O_3/Ni photoanode. The TEM lamella was prepared by focused ion-beam (FIB) milling using a Thermofisher Scios 2 DualBeam FIB. Before cutting, Pt was first deposited on the top face of the Si substrate to protect the Ni catalyst surface from ion damage. Ga-ion cutting was performed using 5 nA at 30 kV with the sample stage tilt at an angle of 53.5°. After cutting, a small probe was attached to the lamella through Pt deposition, and the sample was transferred *in-situ* to a TEM half grid by the probe inside the FIB chamber. The lamella was then thinned by Ga-ion milling at 30 kV for electron transparency.

Reflectance spectra of the n-Si/Ni electrodes with different coverages of the Ni catalyst arrays were acquired using a Cary 5000 spectrometer equipped with a 150-mm, external integrating sphere. Each Si substrate was taped to the back of an aperture that was placed at the rear port of the integrating sphere. A PMT detector was used for ultraviolet (UV) and visible wavelengths (250 – 800 nm), and a lead sulfide detector was used for near infrared (NIR) wavelengths (800 – 1200 nm). A tungsten halogen lamp was used as the source for visible and NIR wavelengths (350 – 1200 nm), and a deuterium lamp was used for the UV region (250 – 350 nm). The scan rate for each measurement was 300 nm/min, and the step size was 1.0 nm.

2.3 Results and Discussion

2.3.1 n-Si/Ni Photoanodes and Ni Coverage Optimization

We first examined the relationship between the Ni filling fraction of n-Si/Ni photoanodes (configuration shown in **Figure 2.2 b**), their optical response, and the photocurrent density they produced. These photoanodes were fabricated using n-type, phosphorous-doped Si wafers with the (111) orientation (resistivity 1-10 Ω cm). The wafers initially had a native oxide layer with a thickness of ~1.6 nm, as measured by ellipsometry. Ni catalyst with sizes of 3 μm or 5 μm were patterned in square arrays on the Si wafers using laser-write lithography (see **Experimental Section 2.2.1** for full experimental details). The spacing between the Ni catalysts on the Si electrodes was adjusted for each designed pattern in the laser writer system to fabricate four different arrays with Ni filling fractions of 4%, 9%, 18%, and 36%. The native oxide layer at the designated regions for the Ni catalysts was first removed by RIE before Ni sputtering. **Figure 2.4** shows SEM images of n-Si/Ni photoanodes with Ni filling fractions ranging from 4% to 36%. For photoanodes with Ni coverages of 4% (**Figure 2.4 a)** and 9% (**Figure 2.4 b)**, the Ni catalysts are circular and have a diameter of approximately 3 μm. For photoanodes with higher Ni coverages of 18% (**Figure 2.4 c)** and 36% (**Figure 2.4 d)**, the Ni catalysts are square with an edge length of 5 μm. All the patterned Ni catalysts are approximately 40-nm thick. The SEM images demonstrate our direct-write laser lithography process can produce uniform, large-scale arrays with well-controlled densities.

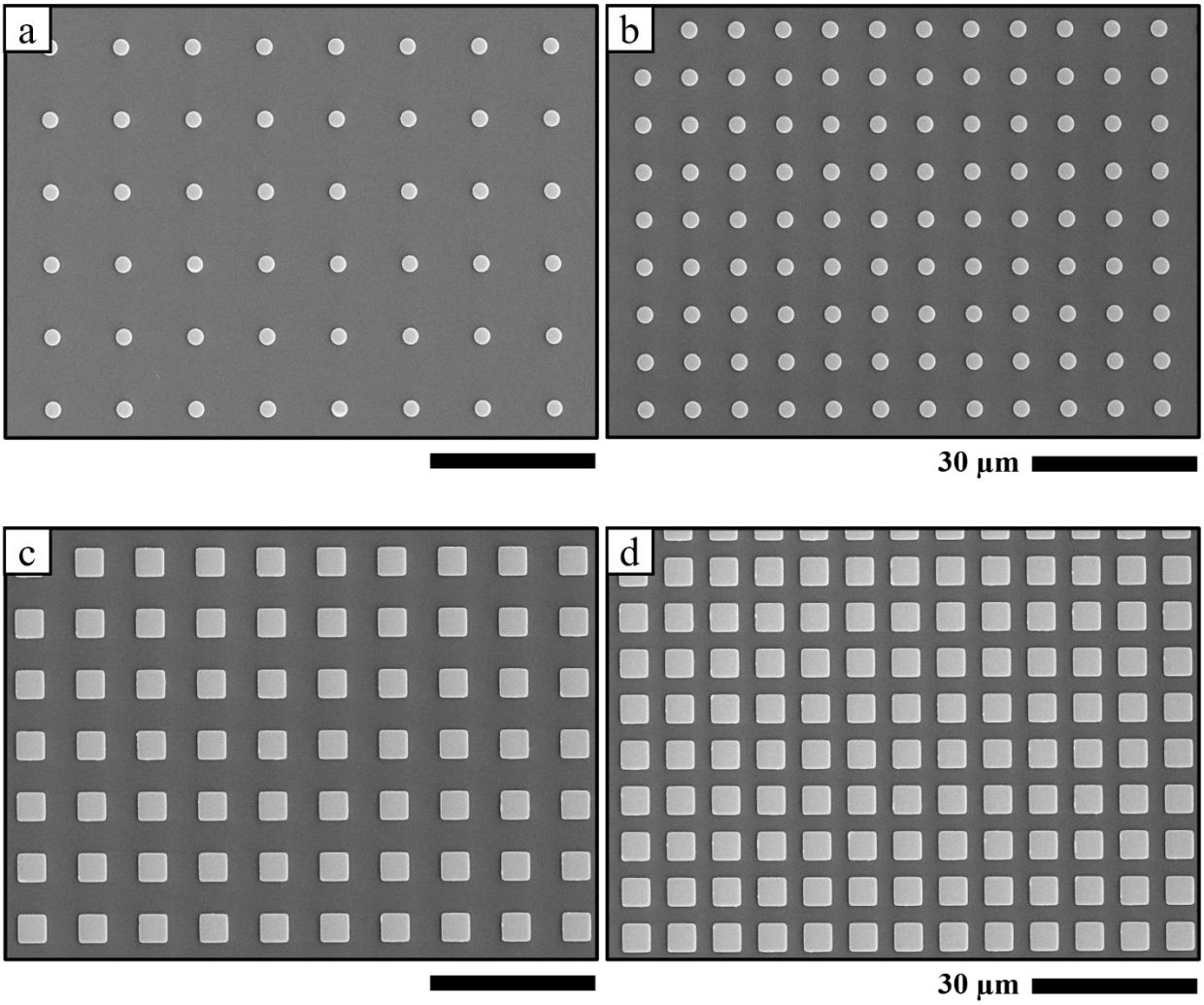

Figure 2.4 Scanning electron microscopy (SEM) images of n-Si/Ni photoanodes with filling fractions between 4.0 and 36.0%. (a) Ni disks with a diameter of 3 µm and 4.0% coverage, (b) Ni disks with a diameter of 3 µm and 9.0% coverage, (c) Ni squares with a 5-µm edge length and 18.0% coverage, and (d) Ni squares with a 5-µm edge length and 36.0% coverage. The thickness of the Ni catalysts is 40 nm for all samples. The scale bars under each image are 30 µm.

A catalyst is required to reduce the kinetic barrier for water oxidation reaction and to help stabilize the Si photoanode.[25, 26] However, the array of Ni catalysts reflects light and obstructs light absorption by the underlying Si.[16, 20] Reflectance spectra of the n-Si/Ni photoanodes shown in **Figure 2.4** were measured using UV-vis-NIR spectroscopy, and the results are shown in **Figure**

2.5. The reflectance spectrum of a bare n-Si substrate is also shown (black line in **Figure 2.5**) for reference. The reflectance spectrum of the photoanode with the lowest Ni coverage (4%) closely resembles bare n-Si with a slight increase in reflectance in the visible and near-infrared regions. The reflectance of the other n-Si/Ni photoanodes clearly increases as the Ni filling fraction increases from 4% to 36%.

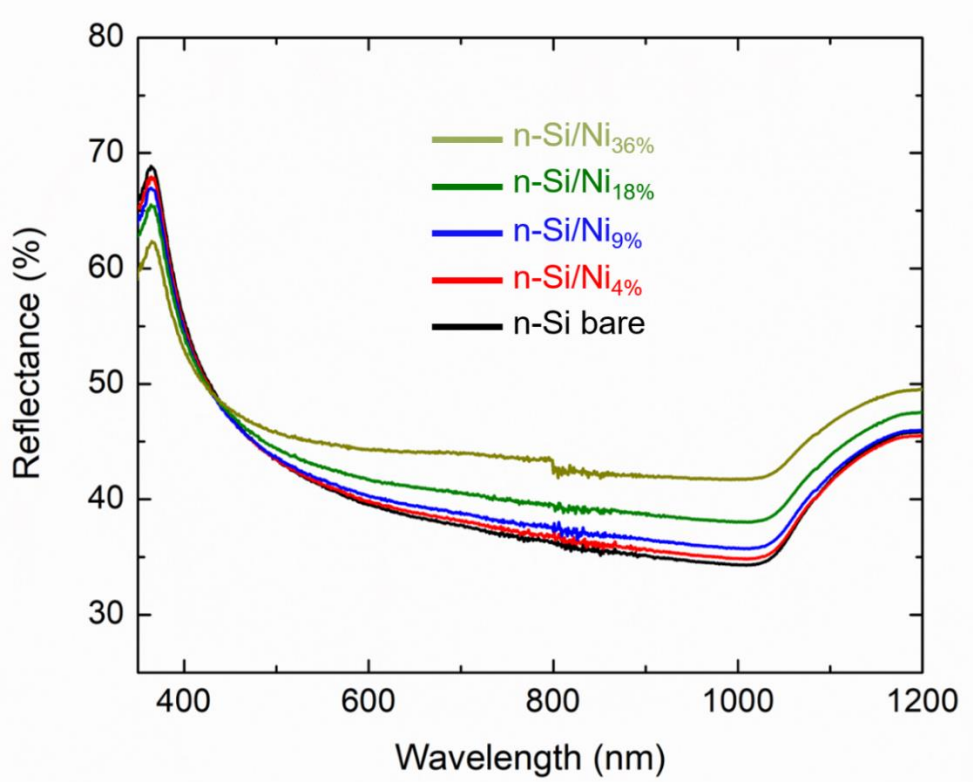

Figure 2.5 Reflectance spectra of the n-Si/Ni photoanodes with filling fractions between 4.0 and 36.0%. For reference, the reflectance spectrum of bare n-Si is also shown. The detector changes at 800 nm, and the increased noise between 800 and 900 nm is due to the lower responsivities of both the PMT and PbS detectors.

The current density versus potential (*J*-*E*) behaviors of n-Si/Ni photoanodes with different Ni filling fractions were characterized both under illumination with an ELH lamp at an irradiance of 100 mW cm^{-2} and in the dark for OER (**Figure 2.6**). Current densities were normalized to the total exposed geometric area of the electrode. The representative scans using cyclic voltammetry

(CV) shown below were all measured after photoelectrochemical activation, by running 50 CV cycles from -0.4 V to +1.6 V vs. Hg/HgO at a scan rate of 100 mV/s under ELH-lamp illumination at 100 mW cm^{-2}. All CV scans of the n-Si/Ni photoanodes showed a small redox wave before the onset of OER, which corresponds to the $Ni(OH)_2$/NiOOH redox couple.[27, 28] Activation of Ni surfaces leading to a gradual improvement of the photoanode performance has been reported in previous studies.[11, 29] The activation process partially transforms $Ni(OH)_2$ at the surface into NiOOH, an active OER catalyst,[30, 31] which increases electrocatalytic performance. In addition, improved hole transfer was found when NiOOH/$Ni(OH)_2$ was formed at the Ni/electrolyte interface during activation.[11]

In the dark, the diffusion-limited current density increased from 1.2 mA cm^{-2} to 4.9 mA cm^{-2} at +1.73 V *vs.* RHE when the Ni filling fraction was increased from 4% to 18% (**Figure 2.6 b**). This observed trend is expected due to the increase in catalytically active area with Ni filling fraction. Under illumination (**Figure 2.6 a**), the measured photocurrent densities of n-Si/Ni photoanodes with different Ni filling fractions were between 27 mA cm^{-2} and 38 mA cm^{-2} at +1.73 V *vs.* RHE, which were significantly higher than the current densities measured in the dark. The higher observed photocurrents are due to the increased concentration of minority carriers (i.e., holes for an n-type semiconductor) under illumination. Interestingly, the sample with a 9% Ni filling fraction provided the highest light-limited photocurrent density, while the samples with 18% and 4% Ni filling fractions showed similar photocurrent densities. This observation can be explained by the trade-off between optical shadowing and electrocatalytic activity provided by the Ni catalysts patterned on the Si photoanodes. Covering the semiconductor surface with metal leads to increased reflection of the incident light, reducing light absorption in the underlying semiconductor and thus diminishing the photocurrent output. **Figure 2.5** shows the relationship

between reflectance and filling fraction of the n-Si/Ni photoanodes. Compared to samples with a Ni filling fraction of 18%, samples with a 9% Ni filling fraction reflect less light, consistent with their higher photocurrent density.

The *J-E* behavior of n-Si/Ni photoanodes shown in **Figure 2.6 a** and **Figure 2.14** (green traces) demonstrates that their onset potential for water oxidation is approximately the same regardless of the size and coverage of the Ni catalyst. The onset potential of n-Si/Ni photoanodes was near +1.4 V *vs.* RHE, similar to previously reported, Ni-patterned n-Si photoanodes.[20] We also fabricated the same Ni catalyst pattern on highly doped, p-type silicon substrates, p^+-Si/Ni, which serve as a non-photoactive electrode for comparison. The *J-E* measurement of the p^+-Si/Ni electrode for water oxidation in the dark gave an onset potential near +1.6 V *vs.* RHE (**Figure 2.8**, blue trace), an approximately 200-mV difference from the onset potential of n-Si/Ni photoanodes under illumination. The small difference in the onset potential suggests that the photovoltage of the n-Si/Ni photoanodes is small despite the high work function of Ni metal. The small photovoltage is likely the result of Fermi level pinning that occurs when the Si semiconductor and Ni metal are in direct contact, leading to surface recombination due to the presence of metal-induced, mid-gap electronic states.[32-34] One method to prevent Fermi level pinning and improve the photovoltage is to insert a thin, insulating layer between the metal and semiconductor, creating a metal-insulator-semiconductor (MIS) junction.[34] The thin insulator separates the metal and semiconductor but still allows charge carriers to tunnel through. In this study, we investigate the performance of Ni-patterned n-Si photoanodes with three types of MIS junction structures and different sizes of the Ni catalyst. When comparing the *J-E* behavior for different junction structures, we kept the Ni filling fraction at 9% since it produced the highest photocurrent density in our n-Si/Ni photoanodes.

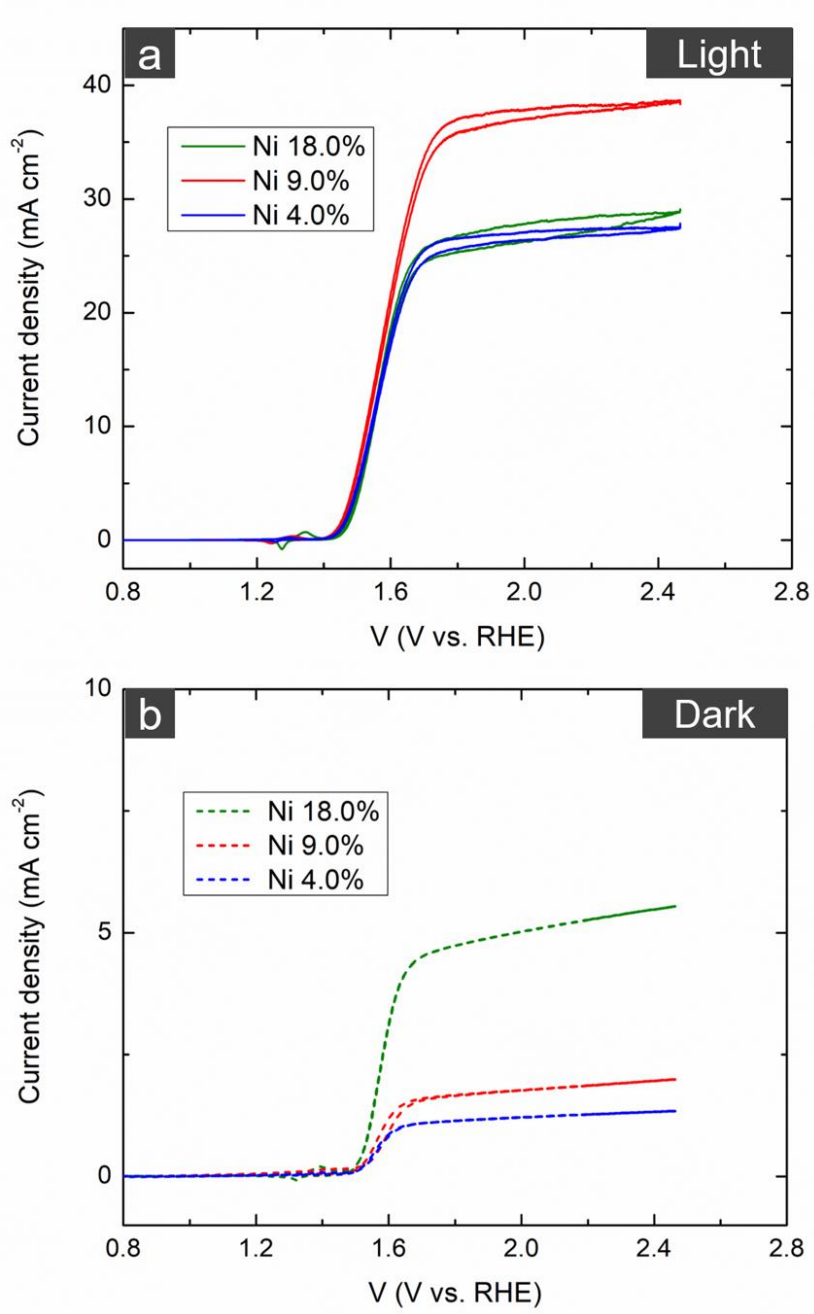

Figure 2.6 Cyclic voltammetry (CV) of n-Si/Ni photoanodes patterned with 3-μm diameter Ni catalysts in 1 M KOH (a) under ELH-lamp illumination at an irradiance of 100 mW cm^{-2}, and (b) in the dark. Scans of photoanodes with three different Ni filling fractions are shown: 4.0% (blue traces), 9.0% (red traces), and 18.0% (green traces). Note the different scales for current density in panels (a) and (b).

2.3.2 n-Si/$SiO_{x,RCA}$ /Al_2O_3/Ni Photoanodes

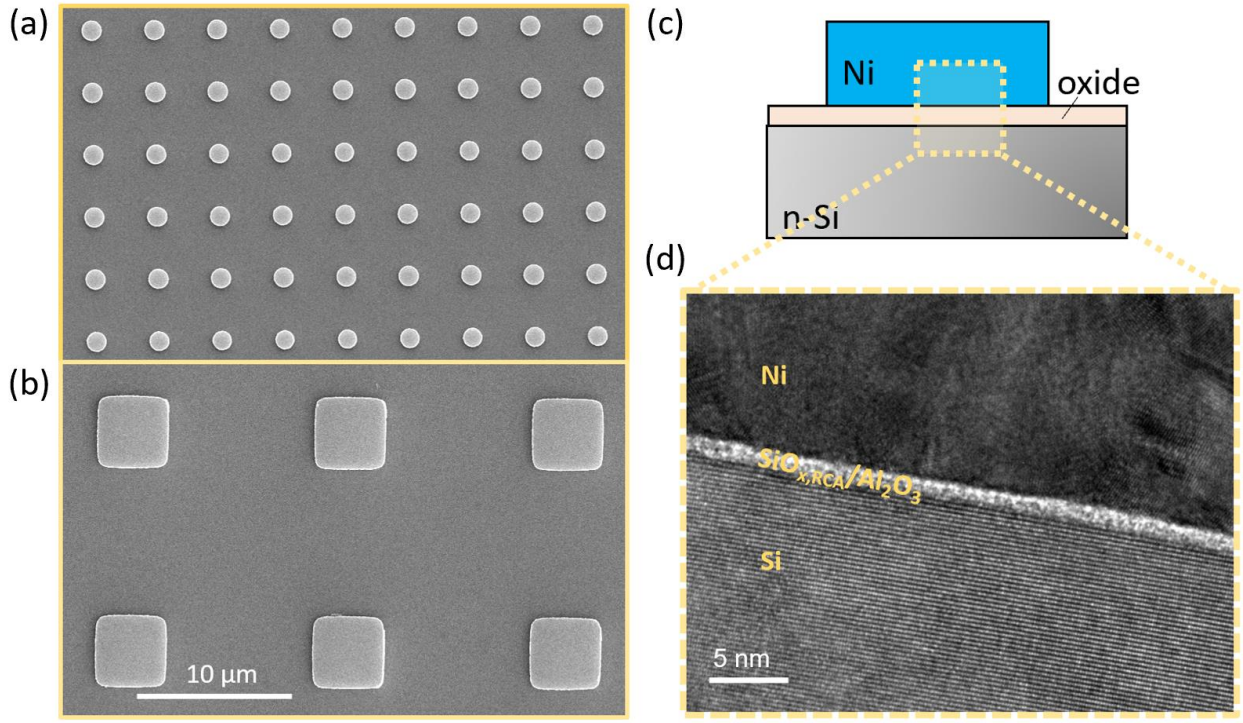

Figure 2.7 n-Si/$SiO_{x,RCA}$/Al_2O_3/Ni photoanodes fabricated by direct-write laser lithography. SEM images of n-Si/$SiO_{x,RCA}$/Al_2O_3/Ni electrodes patterned with (a) Ni disks with a diameter of 1.5 μm and (b) Ni squares with 5-μm edge length. Both electrodes have a Ni filling fraction of 9%. (c) Schematic drawing of the cross-section of a n-Si/$SiO_{x,RCA}$/Al_2O_3/Ni photoanode. (d) Cross-sectional TEM image of n-Si/$SiO_{x,RCA}$/Al_2O_3/Ni photoanode patterned with 1.5 μm diameter Ni catalysts, showing the interfacial oxide layer with a thickness of ~ 2 nm between Si and Ni.

To improve the photovoltage and alleviate Fermi-level pinning in the n-Si/Ni photoanodes, we engineered the semiconductor/catalyst interface by coating the Si substrate with two interfacial oxide layers consisting of silicon oxide and aluminum oxide before patterning the substrate with the Ni catalysts (**Figure 2.7 c**). Experimental details for the preparation of the n-Si/$SiO_{x,RCA}$/Al_2O_3/Ni photoanodes are described in **Section 2.2** above. In brief, the first silicon oxide layer was formed by immersing the Si substrate in an RCA SC-2 solution. The thickness of the SiO_x layer was ~0.8 nm as measured by ellipsometry. The second aluminum oxide layer was

then deposited via ALD, resulting in a thickness of ~1.2 nm as measured by ellipsometry. Ni catalysts with different sizes then were patterned on the n-Si/$SiO_{x,RCA}$/Al_2O_3 substrates. **Figure 2.7 a, b** shows SEM images of the as-prepared n-Si/$SiO_{x,RCA}$/Al_2O_3/Ni photoanodes. These SEM images demonstrate that we are able to pattern the Ni catalysts over a large electrode surface area (3 mm × 3 mm) with a precisely controlled size and interparticle spacing. A high-resolution, cross-sectional TEM image of a n-Si/$SiO_{x,RCA}$/Al_2O_3/Ni photoanode with a Ni catalyst size of 1.5 μm is shown in **Figure 2.7 d**. The TEM image shows the interface between a Ni disk and the Si substrate, which demonstrates that a uniform and complete thin oxide layer was successfully inserted. The Ni catalyst is polycrystalline, and the thickness of the oxide layer comprised of SiO_x and Al_2O_3 is around 2 nm, which is in good agreement with the ellipsometry measurements.

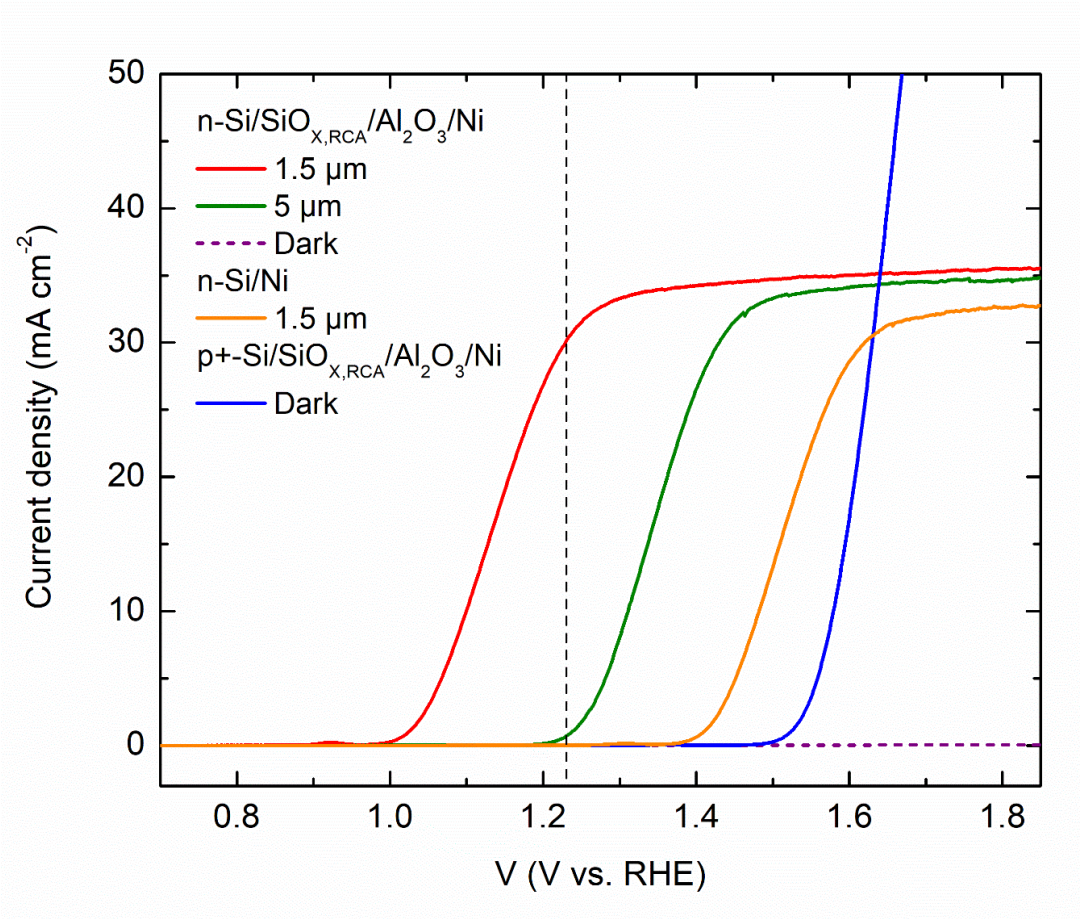

Figure 2.8 Photocurrent density versus applied potential (*J-E*) measured using linear sweep voltammetry for n-Si/$SiO_{x,RCA}$/Al_2O_3/Ni and n-Si/Ni photoanodes with a 9% Ni filling fraction in 1 M KOH under ELH-lamp illumination at 100 mW cm^{-2}. The behaviors of n-Si/$SiO_{x,RCA}$/Al_2O_3/Ni photoanodes patterned with Ni squares with a 5-μm edge length and Ni disks with a 1.5-μm diameter are shown in green and red, respectively. The dashed purple trace shows a n-Si/$SiO_{x,RCA}$/Al_2O_3/Ni photoanode in the dark. For comparison, the orange trace shows a n-Si/Ni photoanode patterned with 1.5-μm diameter Ni disks, and the blue trace shows a non-photoactive p^+-Si/$SiO_{x,RCA}$/Al_2O_3/Ni electrode. The vertical dashed black line indicates the thermodynamic potential for water oxidation, E^0 (O_2/OH^-).

Photoelectrochemical water oxidation using n-Si/$SiO_{x,RCA}$/Al_2O_3/Ni photoanodes with different Ni catalyst sizes was conducted in 1 M KOH under ELH-lamp illumination at a light intensity equivalent to sunlight (i.e., 100 mW cm^{-2}). The anodic behavior of the photoanodes with Ni catalyst sizes of 1.5 μm and 5 μm using linear sweep voltammetry (LSV) are shown in **Figure 2.8**. All LSV scans shown here were obtained after photoelectrochemical conditioning of the Ni

catalyst by applying 50 CV cycles under illumination. LSV scans in the dark were also measured for both photoanodes (i.e., 1.5 μm and 5 μm). Only the scan using 1.5-μm Ni catalysts is shown in the plot (dashed purple trace) as the measured current was close to zero for both photoanodes. For the n-Si/$SiO_{x,RCA}$/Al_2O_3/Ni photoanode with the larger Ni catalyst size (5 μm, green trace), the photocurrent onset potential, determined by the potential required to reach a current density of 100 μA cm^{-2}, was 1.20 V *vs.* RHE. In comparison, n-Si/Ni photoanodes with the 1.5-μm Ni catalysts and same density exhibited an onset potential of 1.40 V *vs.* RHE (**Figure 2.8**, orange trace). Thus, insertion of the oxide layers in the n-Si/$SiO_{x,RCA}$/Al_2O_3/Ni (5 μm) photoanode produced a shift of ~200 mV to more negative potentials for the OER to occur.

The onset potential of a photoanode largely depends on its photovoltage, and a larger photovoltage usually results in a more negative onset potential for oxidation reactions.[14, 35] Accordingly, the negative shift in the onset potential of 200 mV indicates an enhancement in the photovoltage of the n-Si/$SiO_{x,RCA}$/Al_2O_3/Ni photoanode. The photovoltage of a Ni-patterned n-Si photoanode is determined by its Schottky junction barrier height (Φ_b). Ideally, this barrier height is the difference between the electron affinity of Si and the work function (Φ_M) of Ni.[36] However, the presence of surface states can cause Fermi-level pinning, which will diminish the barrier height and the resulting photovoltage.[18, 37] Previous studies have demonstrated that when Ni is directly sputtered onto Si, defects and surface states are introduced at the Ni/Si interface.[38, 39] The high density of surface states causes strong Fermi-level pinning, resulting in a low observed photovoltage for n-Si/Ni photoanodes. On the other hand, interfacial oxide layers including SiO_x, and Al_2O_3, are known to passivate the Si surface and reduce the density of surface states.[18, 40, 41] Therefore, the improved photovoltage of the n-Si/$SiO_{x,RCA}$ /Al_2O_3/Ni photoanode can be partially

attributed to chemical passivation of the stacked $SiO_{x,RCA}$ and Al_2O_3 layers that unpin the Fermi level of Si.

Unlike other large-scale lithography methods, direct laser-write lithography benefits from the maskless feature, which allows us to fabricate samples with varied individual metal catalyst sizes while keeping the total catalyst coverage constant. This provides us the ability to isolate the effect of catalyst size on our photoanode performance. Thus, we fabricated two n-$Si/SiO_{x,RCA}/Al_2O_3$/Ni photoanodes, one with Ni disks with a diameter of 1.5 μm and the other with Ni squares with an edge length of 5 μm; both photoanodes had a Ni filling fraction of 9%. Surprisingly, we observed a significant shift in the onset potential for water oxidation from 1.20 V *vs.* RHE for the 5-μm catalyst pattern (**Figure 2.8**, green trace) to 0.98 V *vs.* RHE when the size of the Ni catalyst was reduced to 1.5 μm (**Figure 2.8**, red trace). To better understand how the Ni catalyst size affects the photoanode performance and the junction energetics, we measure the photovoltaic response of the photoanodes with different Ni catalyst sizes under a series of light intensities. Each photovoltage is obtained by the difference in the potential at the same observed current density between the photoanode under illumination and a non-photoactive p+-$Si/SiO_{x,RCA}/Al_2O_3$/Ni electrode in the dark. The photovoltaic responses of the n-$Si/SiO_{x,RCA}/Al_2O_3$/Ni photoanodes patterned with 1.5-μm and 5-μm Ni catalysts are shown in **Figure 2.9** under several different light intensities. Under a light intensity of 100 mW cm^{-2} (red curves), the photoanode patterned with the 1.5-μm Ni catalysts exhibited an open-circuit photovoltage of 0.49 V, whereas photoanode patterned with the 5-μm Ni catalysts only reached an open-circuit photovoltage of 0.31 V. As they have the same Ni filling fraction and identical chemical and material configurations, the significant gain in photovoltage (from 0.31 to 0.49 V) between these two photoanodes can only be attributed to the size difference of the Ni catalysts.

To gain further insights into the change in solid-state junction energetics when the size of the Ni catalyst is reduced, we calculated the barrier height (Φ_b) of each photoanode using equation (2.1)[40, 42, 43],

$$\Phi_b = \frac{kT}{q}\ln\left(\frac{A^*T^2}{J_s}\right) \quad (2.1)$$

Where k is Boltzmann's constant ($1.38\times 10^{-23}\ J\ K^{-1}$), T is the temperature (298 K), q is the charge of an electron ($1.60 \times 10^{-19}\ C$), $A^*$is the effective Richardson's constant of Si (120 A cm^{-2} K^{-2}),[18] and J_s is the dark saturation current (A cm^{-2}). For photoanodes in solution, J_s can be obtained using equation (2.3)[18], which is derived from the diode equation (2.2)[44] shown below:

$$J = J_s\left(e^{\frac{q(V-JR_sA)}{nKT}} - 1\right) - J_L \quad (2.2)$$

Where J is the observed current density (A cm^{-2}), J_L is the limiting current density (A cm^{-2}), R_s is the series resistance (Ω), n is the diode quality factor, and A is the electrode area (cm^2).

When $J = 0$,

$$V_{oc} = \frac{nkT}{q}\ln\left(\frac{J_L}{J_s} + 1\right) \approx \frac{nkT}{q}\ln\left(\frac{J_L}{J_s}\right) \quad (2.3)$$

The open-circuit voltage (V_{oc}) is defined as the voltage at zero current. V_{oc} and J_L were obtained from the equivalent photovoltaic response of each photoanode measured under different light intensities (**Figure 2.9**). Both n and J_s were determined using equation (2.3) with the measured values of V_{oc} and J_L, in **Figure 2.10 a, b** at a series of light intensities. For the n-Si/$SiO_{x,RCA}$/Al_2O_3/Ni photoanode with the 1.5-μm Ni catalyst size, the diode quality factor, n was determined to be 1.1 from the slope in **Figure 2.10 a**, and the dark saturation

current, J_S was determined from the intercept to be 2.28×10^{-9} A cm^{-2}, corresponding to a barrier height of 0.91 eV. The n-Si/$SiO_{x,RCA}$/Al_2O_3/Ni photoanode with the 5-μm Ni catalyst size has a diode quality factor of 1.3, and a dark saturation current of 2.26×10^{-6} A cm^{-2} as shown in **Figure 2.10 b**. This dark saturation current gives a barrier height of 0.75 eV for the 5-μm pattern, which is significantly smaller than the barrier height of 0.91 eV obtained for the 1.5-μm Ni catalyst size. We attribute the increase in "effective" barrier height exhibited by the n-Si/$SiO_{x,RCA}$/Al_2O_3/Ni photoanode with the smaller Ni catalyst size to the "pinch-off" effect. The observation of a higher "effective" barrier height has been reported in systems with inhomogeneous barrier heights having a contact length scale of the inhomogeneity comparable to or smaller than the depletion width of the semiconductor.[18, 45-49]

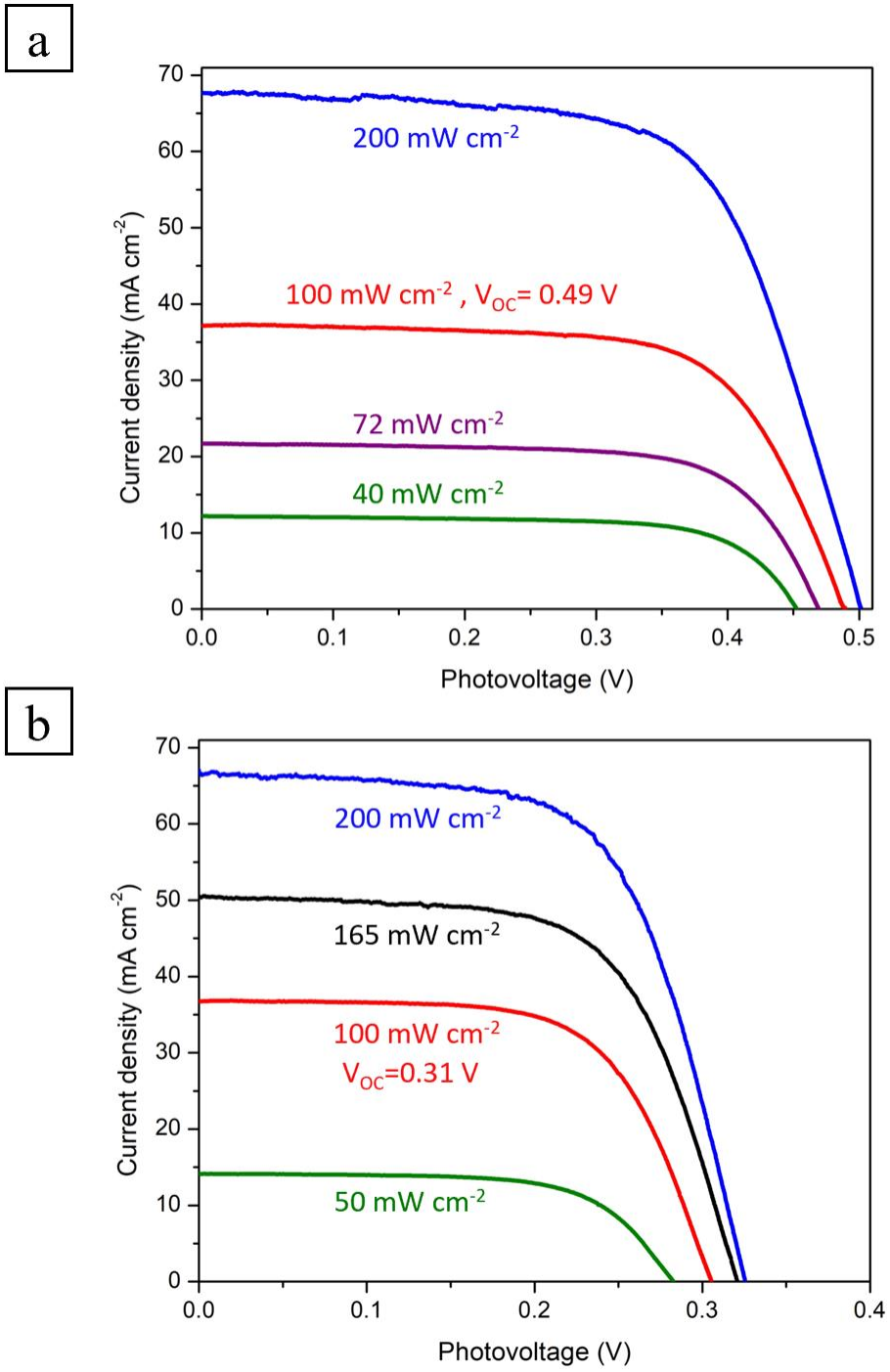

Figure 2.9 Equivalent photovoltaic responses of n-Si/$SiO_{x,RCA}$/Al_2O_3/Ni photoanodes at different light intensities with (a) 1.5-µm Ni catalyst pattern, (b) 5-µm Ni catalyst pattern. The measured photoresponses under ELH-lamp illumination at 100 mW cm^{-2} are shown in red. The open-circuit photovoltages (V_{oc}) at this light intensity are 0.49 V in (a) for the 1.5-µm Ni catalyst pattern and 0.31 V in (b) for the 5-µm Ni catalyst pattern.

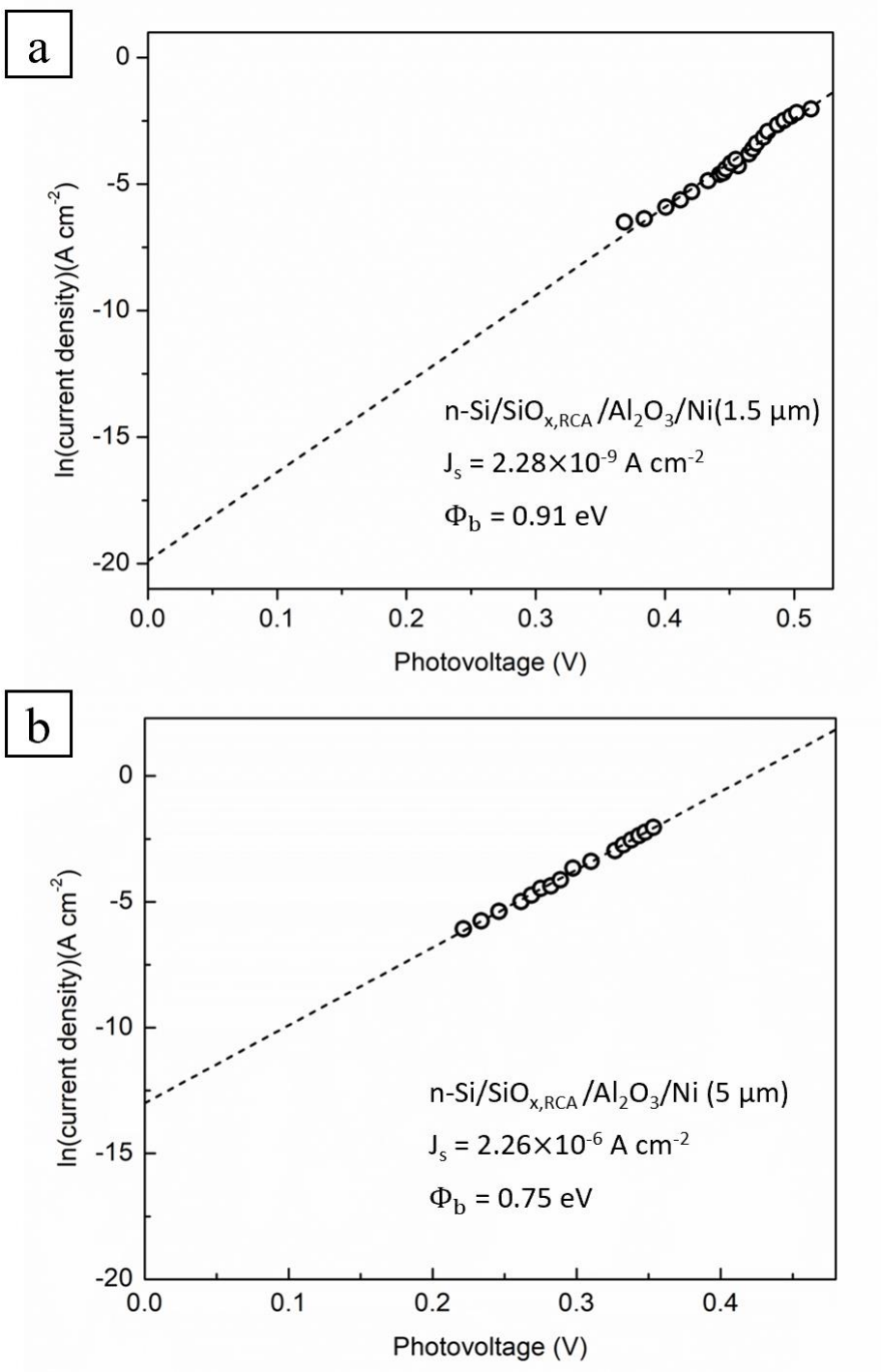

Figure 2.10 Plots of ln(*J*)-*V* showing the measured limiting current density and the corresponding photovoltage under different light intensities for n-Si/$SiO_{x,RCA}$/Al_2O_3/Ni photoanodes with (a) 1.5-µm Ni catalyst pattern, and (b) 5-µm Ni catalyst pattern.

2.3.3 Parallel Conduction and Pinch-off Model in Photoanodes with Inhomogeneous Junctions

The increased barrier height observed for n-Si/$SiO_{x,RCA}$/Al_2O_3/Ni photoanodes as the size of the Ni catalysts decreases can be explained by a transition in charge transport from the parallel-conduction to the pinch-off regime. **Figure 2.11** shows a schematic energy diagram illustrating the two different transport models for n-Si/oxide photoanodes patterned with Ni catalysts. A n-Si substrate coated with an interfacial oxide layer is in contact with two phases resulting in inhomogeneous barrier heights. The Ni-covered region (n-Si/oxide/Ni) forms a Schottky junction, which provides a low barrier height (Φ_b^{Ni}) and a low resistance pathway for charge transport.[11] In contrast, the regions of the Si substrate that are not covered by Ni (n-Si/oxide) have a high barrier height (Φ_b^0) due to the large bandgap of the insulating oxide. In a typical system with inhomogeneous barrier heights, these two different interfaces are considered as separated heterojunctions operating in parallel with stepwise low and high barrier heights, as shown in **Figure 2.11 a**. In this study, the overall barrier height of the n-Si/$SiO_{x,RCA}$/Al_2O_3/Ni (5 μm) photoanode that operates via the parallel conduction model was found to be mainly controlled by the low barrier height n-Si/oxide/Ni junction based on its photoresponse and EIS measurements, which will be discussed at the end of this section.

When the contact area of the Ni catalyst becomes small enough, quantum mechanical tunneling of charge carriers results in a barrier height that is continuously modulated across the n-Si/oxide surface (**Figure 2.11 b**).[24, 50] In this case, the low-barrier height region (n-Si/oxide/Ni) is pinched-off, meaning the majority carriers (e.g., electrons for an n-type semiconductor) do not experience the low-barrier height of n-Si/oxide/Ni junction, but instead experience a higher

"effective" barrier height imposed by the surrounding n-Si/oxide junction.[47] The pinched-off photoanode will thus have an increased overall barrier height that is in between the low and high barrier heights of the two junctions. In addition to the enhanced photovoltage provided by the pinch-off effect, in this configuration minority carriers (e.g., holes in n-Si) will be effectively directed to the less resistive pathway and collect at the Ni catalyst to perform interfacial water oxidation.[51]

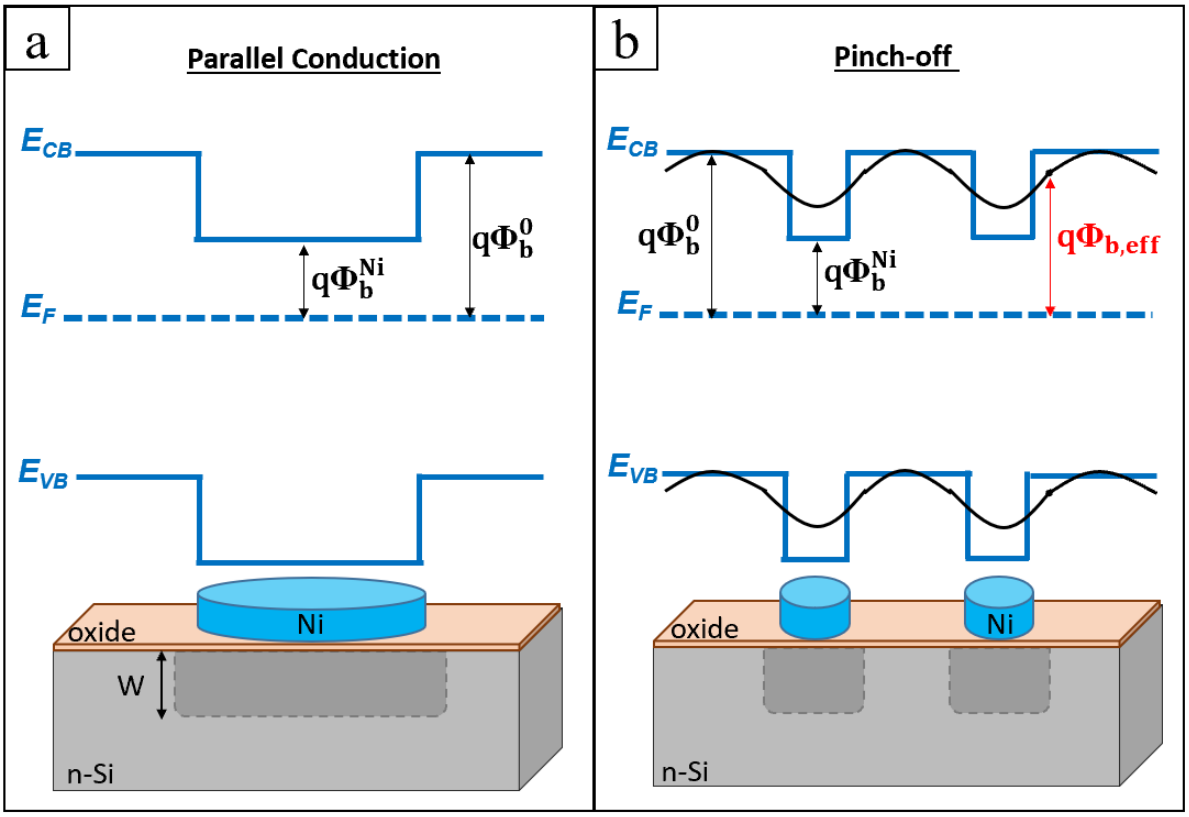

Figure 2.11 Schematic energy diagrams of n-type silicon coated with a thin oxide layer in contact with a Ni patch that produces a low-barrier height (Φ_b^{Ni}) region, and a second phase surrounding the Ni patch that produces a high-barrier height region (Φ_b^0) region. In (a) the Ni patch is large and in (b) the Ni patch is small compared with the depletion width. Blue lines represent the energies of the conduction band edge (E_{CB}), valence band edge (E_{VB}), and Fermi level (E_F, dashed line) for n-Si. In (b), the Ni patches are pinched-off due to their small size, resulting in an effective barrier height ($\Phi_{b,eff}$) that is much higher than Φ_b^{Ni}.

The barrier height of the n-Si/$SiO_{x,RCA}$/Al_2O_3/Ni junction was evaluated by performing EIS in an electrolyte solution containing the ferro/ferricyanide redox couple. Note the Ni layer here is a complete film with a homogeneous barrier height instead of the patterned Ni catalysts. The Mott–Schottky equation relates the capacitance to the applied voltage across a semiconductor/electrolyte junction following:[52]

$$\frac{1}{C_{SC}^2} = \frac{2}{\varepsilon_0 \varepsilon_{Si} A^2 q N_D}\left(\mathrm{V} - \mathrm{V_{fb}} - \frac{kT}{q}\right) \tag{2.4}$$

Where C_{SC} is space-charge capacitance (F cm^{-2}), ε_0 is the vacuum permittivity (8.85×10^{-14} F cm^{-1}), ε_{Si} is the relative permittivity of silicon (11.7), A is the surface area of the electrode in contact with the electrolyte (cm^2), q is the charge of an electron (1.6×10^{-9} C), N_D is the donor density of Si (cm^{-3}), V is the applied potential (V), V_{fb} is the flat-band potential (V), k is the Boltzman's constant (1.38×10^{-23} J K^{-1}), and T is temperature (298 K). Using equation (2.4), the flat-band potential (V_{fb}) can be determined from the extrapolated intercept of the x-axis in the Mott–Schottky plot, and the donor density (N_D) can be calculated from the slope of the Mott–Schottky plot. The EIS measurements for the n-Si/$SiO_{x,RCA}$/Al_2O_3/Ni electrode film is shown in **Figure 2.12**. From the Mott–Schottky plot, the V_{fb} of the n-Si/$SiO_{x,RCA}$/Al_2O_3/Ni film was -0.59 V versus $Fe(CN)_6^{3-/4-}$, and the donor density (N_D) was calculated from the slope (2.51×10^{15} cm^4 F^{-2} V^{-1}) to be 4.77×10^{15} cm^{-3}. The N_D value corresponds to a resistivity of 1.02 Ω cm and is within the range (1-10 Ω cm) provided by the manufacturer. The barrier height (Φ_b) was then calculated using the Schottky equation below:

$$\Phi_b = E_{fb} + V_n \tag{2.5}$$

where V_n is the difference in energy between the conduction band edge and the Fermi level, and was obtained using the following equation:

$$V_n = kT\ln\left(\frac{N_C}{N_D}\right) \tag{2.6}$$

where N_C is the density of states in the conduction band, and equals 2.8×10^{19} cm^{-3} for silicon at room temperature.[53] V_n was calculated to be 0.22 eV, and thus the barrier height is 0.73 eV for the n-Si/$SiO_{x,RCA}$/Al_2O_3/Ni film.

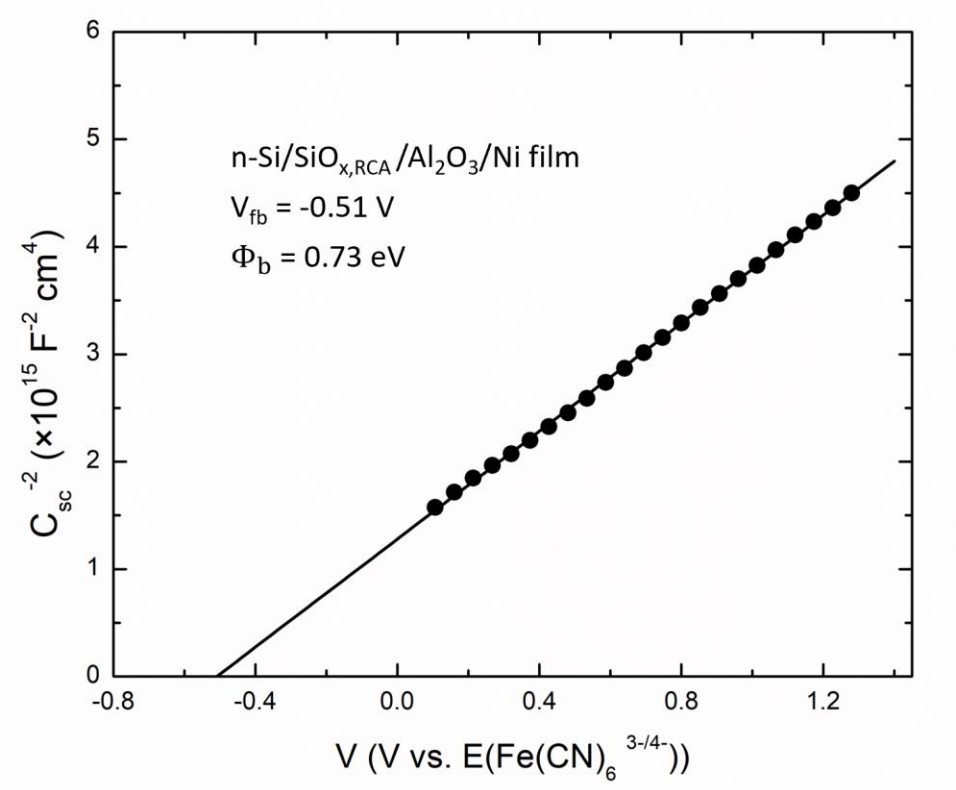

Figure 2.12 Mott–Schottky plot of the inverse of the space-charge capacitance squared as a function of the applied potential relative to the redox potential of the $Fe(CN)_6^{3-/4-}$ couple for a n-Si/$SiO_{x,RCA}$/Al_2O_3/Ni electrode with a complete Ni film.

The 0.73 eV barrier height of the n-Si/$SiO_{x,RCA}$/Al_2O_3/Ni (film) junction obtained from Mott–Schottky impedance analysis was similar to the 0.75 eV barrier height we observed for the

n-Si/$SiO_{x,RCA}$/Al_2O_3/Ni (5-μm) photoanode. This result indicates that the performance of the n-Si/$SiO_{x,RCA}$/Al_2O_3/Ni (5-μm) photoanodes with inhomogeneous barrier heights that are in the parallel-conduction regime is determined by the low barrier height of the n-Si/$SiO_{x,RCA}$/Al_2O_3/Ni junction. However, the barrier height of the pinched-off n-Si/$SiO_{x,RCA}$/Al_2O_3/Ni (1.5-μm) photoanodes deviated from that of the n-Si/$SiO_{x,RCA}$/Al_2O_3/Ni junction with a complete Ni film and reached a value of 0.91 eV. The observed higher "effective" barrier height of the n-Si/$SiO_{x,RCA}$/Al_2O_3/Ni (1.5-μm) photoanode results from the surrounding high barrier height induced depletion region that overlaps with the depletion region of the low barrier height Ni region when the Ni contact size is reduced. Thus, the overall performance is controlled by both the low- and high-barrier height junctions of the n-Si/$SiO_{x,RCA}$/Al_2O_3/Ni (1.5 μm) photoanode.

2.3.4 Approaching the Pinch-off Regime through Interfacial Engineering

In this study, we demonstrated that we are able to systematically control the Ni catalyst size as well as manipulate the configuration of the interfacial oxide layer in Si photoanodes. The ability to pattern Ni catalysts with a well-controlled individual size and overall surface coverage on different oxide layer surfaces provides us the opportunity to investigate whether we can approach the pinch-off regime by simply increasing barrier-height difference (Δ) between the low and the high barriers at the inhomogeneously coated Ni catalyst Schottky junction (**Figure 2.13**). For small circular patches with a low barrier height (Φ_b^{Patch}) surrounded by an otherwise uniform region of high barrier height (Φ_b^0), significant pinch-off is expected when:[47, 54]

$$\frac{\Delta}{2R} > \frac{V_{bb}}{W} \tag{2.7}$$

Where in our n-Si/Ni model system, R is the radius of the circular Ni patch (cm), Δ is the difference between the high and low barrier heights ($\Delta = \Phi_b^0 - \Phi_b^{Ni}$, V), W (cm) and V_{bb} are the depletion width and the degree of band bending (V), respectively, behind the high-barrier-height region of n-Si. V_{bb} is defined as:[47]

$$V_{bb} = \Phi_b^0 - V_n + V_{app} \tag{2.8}$$

where V_n is the potential difference between the Fermi level and conduction band minimum in n-Si, and V_{app} is the applied potential. The depletion width, $W = (2\varepsilon_{si}V_{bb}/qN_D)^{1/2}$ in n-Si can vary from a fraction of a micrometer to tens of micrometers depending on the doping density and the applied bias.[54, 55]

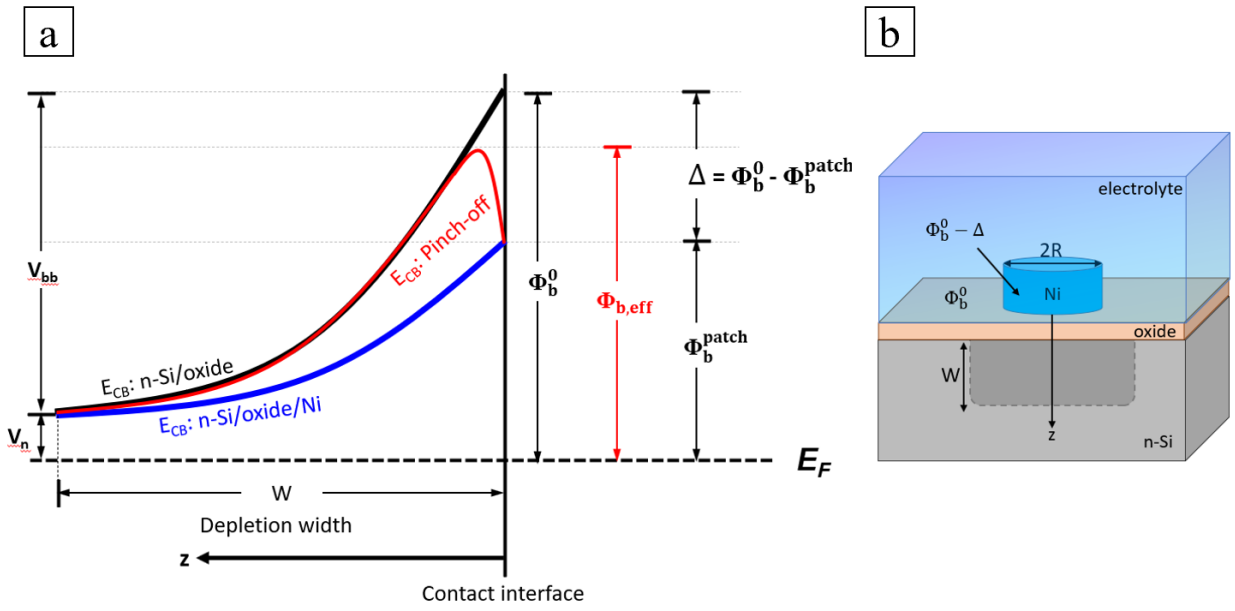

Figure 2.13 (a) Potential of the conduction band minimum behind a contact with an inhomogeneous barrier height as a function of position in the n-type silicon electrode. The position of the interface is taken as zero, and further into the n-Si (i.e., away from the interface) is taken to be the positive z direction. $\Phi_{b,eff}$ is the effective barrier height at a pinched-off, low-barrier-height, circular Ni patch. (b) Schematic of a small Ni circular patch with a low barrier height, $\Phi_b^0 - \Delta$, surrounded by a region of high barrier height, Φ_b^0. R is the radius of the Ni patch. Figure adapted from reference [47].

Numerical simulations of the change in potential along the *z*-axis perpendicular to the semiconductor surface and passing through the center of the low-barrier-height, circular patch were performed by Sullivan and co-workers using the following analytic expression:[56]

$$V(z) = V_{\text{bb}}\left(1 - \frac{z}{W}\right)^2 - \Delta\left(1 - \frac{z}{\left(z^2 + R^2\right)^{1/2}}\right) + V_n + V_{\text{app}} \qquad (2.9)$$

Where $V(z)$ is the potential of the conduction band minimum of the semiconductor, and the distance into the semiconductor (i.e., away from the interface) is taken to be the positive z-direction. The expected potential profile behind a pinched-off circular patch is shown in **Figure 2.13 a** (red curve). The effective barrier height, $\Phi_{\text{b,eff}}$, at the pinched-off, low-barrier-height region is smaller than the surrounding high barrier height, Φ_{b}^{0}, but larger than the original, low barrier height, $\Phi_{\text{b}}^{\text{patch}}$. The criterion for pinch-off in equation (2.7) is determined by differentiating the above equation (2.9) with respect to *z*, and its validity has been demonstrated in previous numerical simulations.[56]

Several prior reports on photoelectrochemical water oxidation demonstrated that by utilizing MIS photoanodes decorated with metal nanoparticles the pinch-off regime could be achieved operating under the condition where $R \ll W$.[3, 11, 18, 19] In this study, we fabricated photoanodes not only with different sizes of metal catalysts but also different configurations of the interfacial oxide layer to achieve the pinch-off regime under the condition: $\frac{\Delta}{2R} > \frac{V_{\text{bb}}}{W}$. To investigate the effect of Δ, three different interfacial oxide layer configurations were examined with the exact same Ni catalysts patterned on each substrate. **Figure 2.14** shows a schematic of the three different configurations and the photoresponses of a total of six different samples: two photoanodes for each

configuration patterned with 1.5-μm and 5-μm Ni catalysts, respectively, with the same 9% Ni filling fraction.

Among the three photoanode configurations, only n-Si/$SiO_{x,RCA}$/Al_2O_3/Ni photoanodes exhibited a size-dependent pinch-off effect in which the onset potential shifted negatively when the size of the patterned Ni catalysts was reduced from 5 μm to 1.5 μm. Since the size of the 1.5-μm Ni catalysts was kept the same for all three photoanode configurations, we propose that the barrier-height difference, $\Delta = \Phi_b^0 - \Phi_b^{Ni}$, is largest for the n-Si/$SiO_{x,RCA}$/Al_2O_3/Ni photoanodes among the three different configurations and enables pinch-off with Ni catalysts at a relatively large size (compared to nanoparticle catalysts used previously). The value of Δ for each configuration was further measured to verify our hypothesis, and the details are discussed below. **Table 2.2** compares the values of Δ for the three photoanode configurations.

Table 2.2 Barrier-height difference (Δ) and the corresponding onset potential for the three different photoanode configurations with different sizes of the Ni catalyst.

Photoanode	Φ_b^0 (V)	Φ_b^{Ni} (V)	Δ (V)	Ni catalyst size	V_{onset} (V *vs.* RHE)
n-Si/Ni	0.7	0.61[17]	0.09	5 μm	1.4 V
				1.5 μm	1.4 V
n-Si/$SiO_{x,native}$/Ni	0.7	0.61 < V < 0.73	< 0.09	5 μm	1.25 V
				1.5 μm	1.25 V
n-Si/$SiO_{x,RCA}$/Al_2O_3/Ni	1.29	0.73	0.56	5 μm	1.2 V
				1.5 μm	0.98 V

The two photoanodes with the n-Si/Ni configuration and different sizes of the patterned Ni catalyst exhibited nearly the same photoresponse (n-Si/Ni 1.5 μm: green trace and n-Si/Ni 5 μm: dashed green trace in **Figure 2.14**), both with an onset potential of ~1.4 V *vs.* RHE. This observation implies the criteria $\frac{\Delta}{2R} > \frac{V_{bb}}{W}$ for pinch-off was not met in the n-Si/Ni photoanodes even

when the radius of circular Ni contact decreased to 0.75 μm. Φ_b^0 in this configuration is determined by the n-Si/native oxide junction surrounding the Ni catalyst and was measured to be ~0.7 eV by Mott–Schottky impedance analysis (**Figure 2.15 a**). We assume a value of 0.61 eV for Φ_b^{Ni} based on a recently reported value for individual n-Si/Ni nanocontacts measured via conductive AFM.[17] Thus, Δ for the n-Si/Ni photoanode configuration in this study is approximately 0.09 V. In general, for a larger contact area, a larger value of Δ is required to reach pinch-off. Our results are consistent with prior numerical simulations that showed when Δ is 0.1 eV, the radius of the circular patch has to be smaller than 0.1 μm in order to achieve pinch-off.[56]

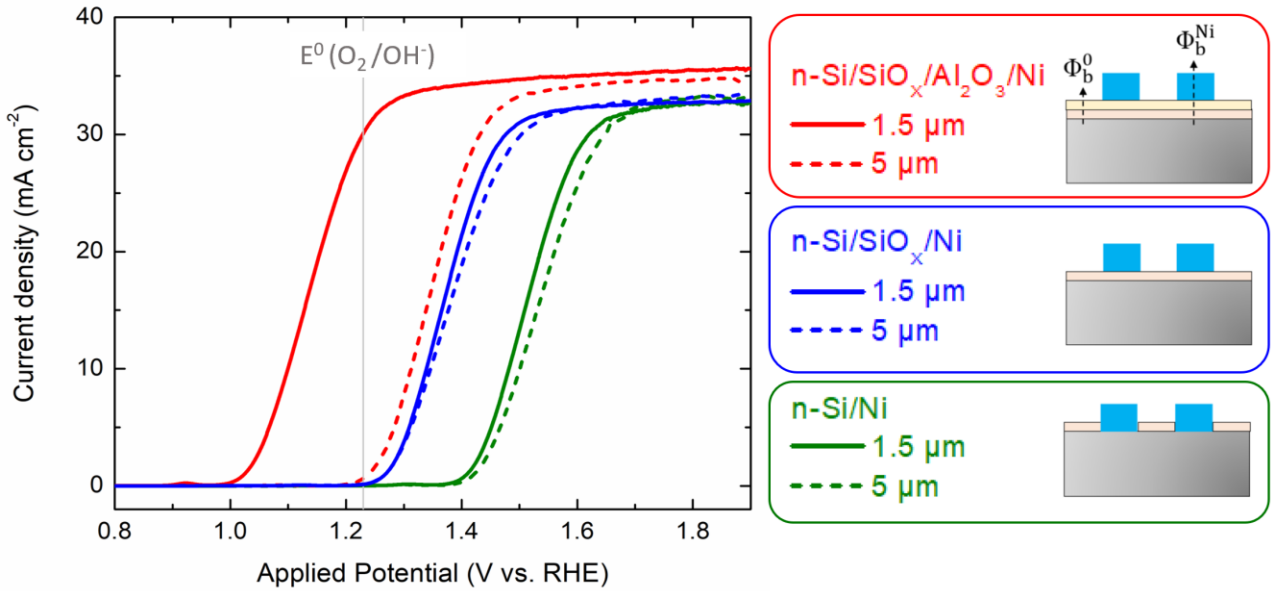

Figure 2.14 Representative *J-E* curves of photoanodes with three different interface configurations in 1 M KOH under ELH-lamp illumination at 100 mW cm^{-2}. Schematics of the three photoanode configurations with the same Ni-catalyst pattern but different values of Φ_b^0, Φ_b^{Ni}, and Δ are shown in the panels on the right. From top to bottom: n-Si/$SiO_{x,RCA}$/Al_2O_3/Ni, n-Si/$SiO_{x,native}$/Ni, and n-Si/Ni.

Similarly, the photoresponses of the two n-Si/$SiO_{x,native}$/Ni photoanodes patterned with different Ni catalyst sizes showed no significant difference (n-Si/$SiO_{x,native}$/Ni 1.5 μm: blue trace and n-Si/$SiO_{x,native}$/Ni 5 μm: dashed blue trace in **Figure 2.14**). However, the onset potentials of both photoanodes shifted by 0.15 V to 1.25 V *vs.* RHE, indicating an improved photovoltage compared to the n-Si/Ni photoanode. In this configuration, Φ_b^0 is the same as the n-Si/Ni photoanodes from the n-Si/native oxide junction that surrounds the Ni catalysts. However, the value of Φ_b^{Ni} under the Ni patches changes because of the presence of a thin native oxide layer (~1.6 nm) between Ni and n-Si. The negative shift in the onset potential is expected, as the presence of the native oxide layer alleviates Fermi-level pinning, resulting in an increased Φ_b^{Ni}. Therefore, Δ for the n-Si/$SiO_{x,native}$/Ni photoanodes is expected to be even smaller than the value of Δ for n-Si/Ni photoanodes, such that they do not operate in the pinch-off regime using the dimensions of Ni catalysts investigated here.

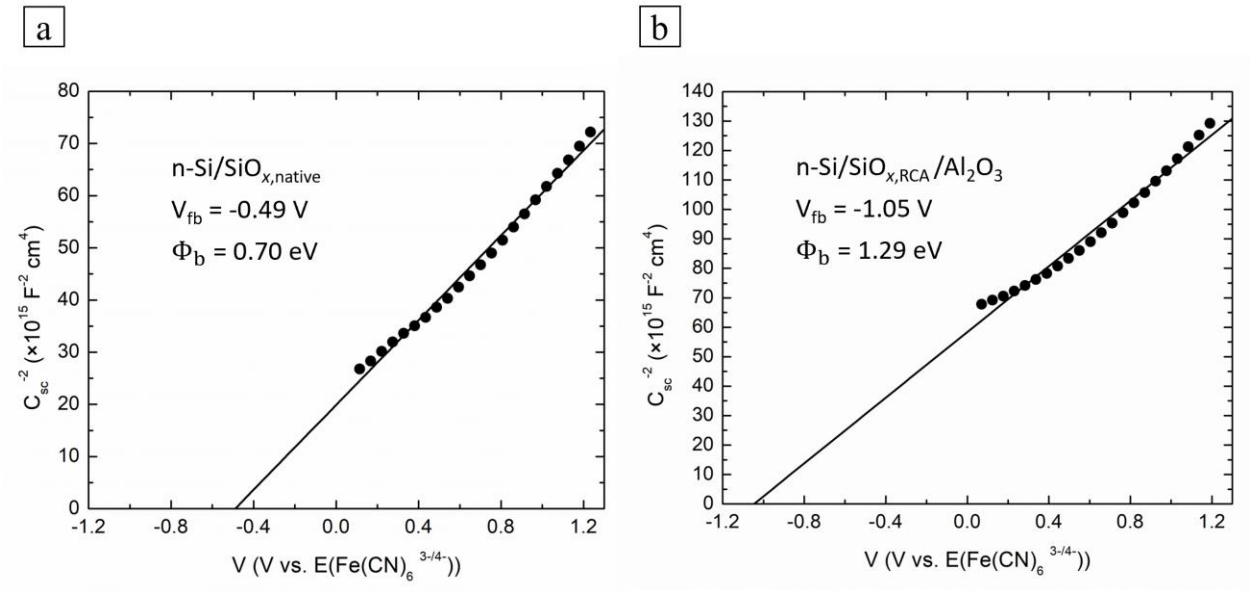

Figure 2.15 Mott–Schottky plots of the inverse of the space-charge capacitance squared as a function of the applied potential relative to the redox potential of the $Fe(CN)_6^{3-/4-}$ couple for (a) a n-Si electrode with native oxide on the surface and (b) n-Si electrode coated with a stacked layer of $SiO_{x,RCA,}$ and Al_2O_3.

After introducing a layer of aluminum oxide between the SiO_x/Ni interface, we observed a further shift in the onset potential to ~1.2 V *vs.* RHE for the n-Si/$SiO_{x,RCA}$/Al_2O_3/Ni photoanode patterned with 5-μm Ni catalysts compared to the n-Si/$SiO_{x,native}$/Ni photoanodes (~1.25 V vs RHE). The higher quality of chemical passivation provided by the stacked layers of Al_2O_3 and $SiO_{x,RCA}$ compared to the single $SiO_{x,native}$ layer unpins the Fermi level even more, leading to a further negative shift in the onset potential. More importantly, when the size of the Ni catalysts on the n-Si/$SiO_{x,RCA}$/Al_2O_3/Ni photoanode was reduced to 1.5 μm, we observed a significant shift in onset potential to ~0.98 V *vs.* RHE. We did not observe this size-dependent phenomenon for the other two photoanode configurations. In this configuration, Φ_b^{Ni} is the barrier height at the Ni catalyst region, and Φ_b^0 is the barrier height at the n-Si/$SiO_{x,RCA}$/Al_2O_3 junction surrounding the Ni catalyst. Both Φ_b^{Ni} and Φ_b^0 were measured separately by Mott–Schottky impedance analysis to be

0.73 eV (**Figure 2.12**) and 1.29 eV (**Figure 2.15 b**), respectively. The value of Δ in this configuration is thus estimated to be 0.56 V, which is significantly larger than the value of Δ for the other two photoanode configurations (**Table 2.2**). Due to the large value of Δ in n-Si/$SiO_{x,RCA}$/Al_2O_3/Ni photoanodes, the criteria: $\frac{\Delta}{2R} > \frac{V_{bb}}{W}$ needed to achieve pinch-off can be met when the Ni contact radius is reduced to 0.75 μm. Thus, we attribute the negative shift in onset potential and the improvement in photovoltage observed for the n-Si/$SiO_{x,RCA}$/Al_2O_3/Ni photoanode patterned with 1.5-μm Ni catalysts (R = 0.75 μm) in comparison with the 5-μm Ni catalysts patterned ones to the pinch-off effect. The fact that the photoresponses of photoanodes patterned with different Ni catalyst sizes showed no difference in the other two configurations with small Δ, suggests that we have successfully entered the pinch-off regime without utilizing nanoscale Ni catalysts but by increasing Δ through interfacial engineering.

2.3.5 Stability of n-Si/$SiO_{x,RCA}$ /Al_2O_3/Ni Photoanodes during Water Oxidation

The stability of a n-Si/$SiO_{x,RCA}$/Al_2O_3/Ni photoanode (1.5-μm) during water oxidation was evaluated in a 1.0 M KOH solution under illumination with an ENH-type halogen lamp at a constant applied potential of 1.73 V versus RHE for 48 h. The measured chronoamperometry curve is shown in **Figure 2.16**. The initial photocurrent density was ~36 mA cm^{-2}. The photoanode operated continuously for 48 h in a highly corrosive KOH solution without a noticeable decay in current. The minor fluctuations in photocurrent are due to the formation and detachment of gas bubbles at the electrode surface and also the result of N_2 purging during the measurement. Several studies on Si photoanodes decorated with metal catalysts have shown that deactivation of photoanodes during water oxidation is mainly due to etching or detachment of the catalyst in the strongly alkaline electrolyte.[15, 20] The loss of catalyst is more extreme for Si photoanodes decorated

with nanoscale particles, leading to poor photoanode stability (< 11 h).[11, 18, 19] The morphology of the n-Si/$SiO_{x,RCA}$/Al_2O_3/Ni photoanode patterned with 1.5-μm Ni catalysts after 48 h of water oxidation was examined using SEM (**Figure 2.16, inset**). There was no noticeable degradation or loss of the Ni catalyst, consistent with the stable photocurrent over this time period.

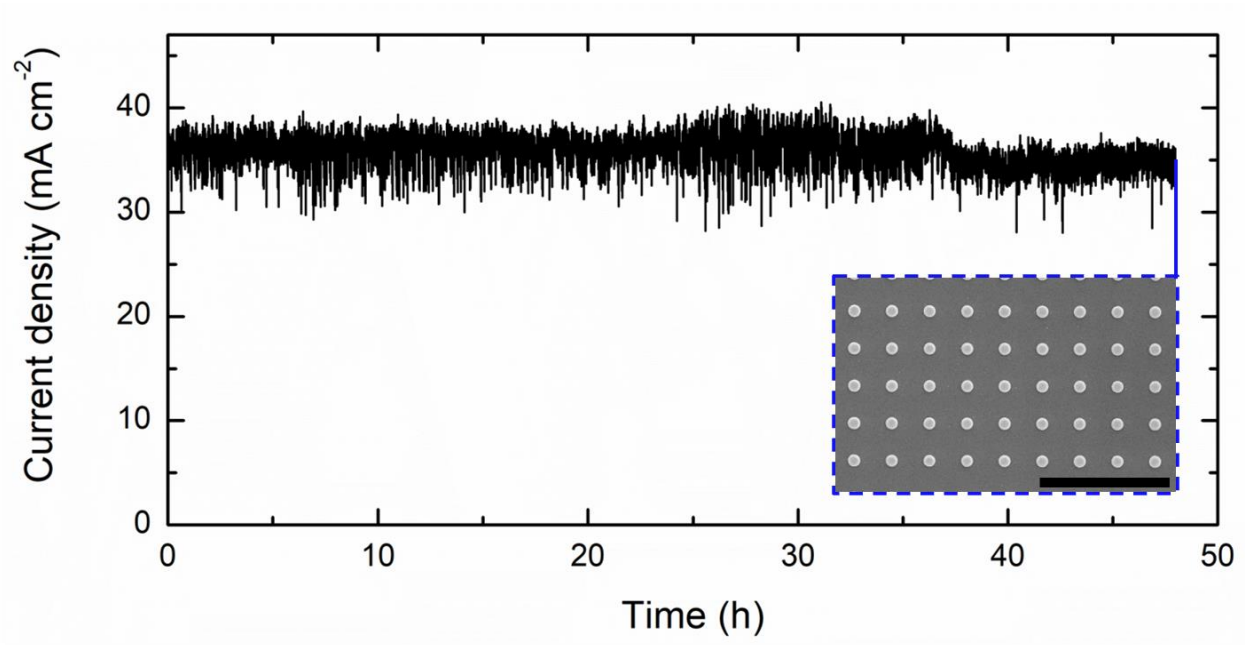

Figure 2.16 Current density versus time using a n-Si/$SiO_{x,RCA}$/Al_2O_3/Ni photoanode at a constant applied potential of 1.73 V vs. RHE in a 1 M KOH solution under ENH lamp illumination at 100 mW cm^{-2}. The Ni catalyst size is 1.5 μm, and the Ni filling fraction is 9%. The measurement was stopped at 24 h and resumed after the electrolyte was replaced with fresh 1 M KOH. The inset shows a SEM image of the n-Si/$SiO_{x,RCA}$/Al_2O_3/Ni photoanode after 48 h of continuous operation. The scale bar in the inset is 20 μm.

Importantly, the 0.49 V photovoltage we observed for the n-Si/$SiO_{x,RCA}$/Al_2O_3/Ni photoanode patterned with 1.5-μm Ni catalysts is better than or comparable to most of the recently reported n-Si photoanodes decorated with nanoscale Ni particles operating in the pinch-off regime (**Table 2.1**).[3, 11, 18, 19, 23, 24] These photoanodes require nanoscale catalysts to achieve a high

photovoltage through pinch-off, which inevitably leads to poor photoanode stability. In this study, we demonstrated that we are able to enter the pinch-off regime using microscale Ni catalysts by constructing a unique inhomogeneous MIS junction through interfacial engineering. The n-Si/$SiO_{x,RCA}$/Al_2O_3/Ni (1.5-μm) photoanode we fabricated enables exploitation of the pinch-off effect to achieve a high photovoltage without sacrificing photoanode stability.

2.4 Summary and Conclusions

In summary, we fabricated high-performance (onset potential = 0.98 V *vs.* RHE, photocurrent density = 30.2 mA cm^{-2} at 1.23 V *vs*. RHE), Si-based MIS photoanodes consisting of n-Si/$SiO_{x,RCA}$/Al_2O_3/Ni patterned with low-cost, ordered nickel arrays for photoelectrochemical water oxidation. Despite the fact that Ni only covers a small portion of the Si photoanode (9 % Ni filling fraction), our photoanode showed remarkable stability operating in a highly corrosive alkaline solution for over 48 h. Using a combination of laser lithography and interfacial engineering, we systematically varied the photoanode configuration as well as the size of the Ni catalysts and demonstrated that we could achieve the pinch-off effect with microscale Ni catalysts by tuning the barrier-height difference (Δ) between the low and the high barriers at the inhomogeneous Schottky junction. Among the three different configurations, the photoanode with the stacked $SiO_{x,RCA}$/Al_2O_3 interfacial oxide layer provided the largest Δ, and a significant improvement in photovoltage was observed when the Ni catalyst size was reduced from 5 μm to 1.5 μm due to the pinch-off effect. In addition, we have shown that the interfacial oxide layers not only play a critical role in turning on the pinch-off effect but also determine the extent of Fermi-level depinning, which is responsible for the shift in onset potential between the different photoanode configurations. Finally, our pinched-off photoanodes achieve a photovoltage close to

that of a np^+-Si buried-junction photoanode. Thus, our design provides a novel strategy for employing the pinch-off effect without the need for nanoscale catalysts, which suffer from poor stability. This work is important in directing the future design of inhomogeneous MIS junctions for the realization of efficient and stable pinched-off silicon-based photoanodes.

2.5 Acknowledgements

This material is based upon work supported by the National Science Foundation (NSF) under grant no. CHE-1753344. Laser-write lithography, atomic layer deposition, Ni-film deposition, reactive-ion etching, ellipsometry, electron microscopy, and x-ray photoelectron spectroscopy were performed at the Institute of Materials Science & Engineering at Washington University.

2.6 References

1. Kuang, Y.; Jia, Q.; Ma, G.; Hisatomi, T.; Minegishi, T.; Nishiyama, H.; Nakabayashi, M.; Shibata, N.; Yamada, T.; Kudo, A., Ultrastable low-bias water splitting photoanodes via photocorrosion inhibition and in situ catalyst regeneration. *Nature Energy* **2016,** *2* (1), 1-9.

2. Lee, S. A.; Choi, S.; Kim, C.; Yang, J. W.; Kim, S. Y.; Jang, H. W., Si-based water oxidation photoanodes conjugated with earth-abundant transition metal-based catalysts. *ACS Materials Letters* **2019,** *2* (1), 107-126.

3. Lee, S. A.; Lee, T. H.; Kim, C.; Lee, M. G.; Choi, M.-J.; Park, H.; Choi, S.; Oh, J.; Jang, H. W., Tailored NiO_x/Ni cocatalysts on silicon for highly efficient water splitting photoanodes via pulsed electrodeposition. *ACS Catalysis* **2018,** *8* (8), 7261-7269.

4. Chen, Y. W.; Prange, J. D.; Dühnen, S.; Park, Y.; Gunji, M.; Chidsey, C. E.; McIntyre, P. C., Atomic layer-deposited tunnel oxide stabilizes silicon photoanodes for water oxidation. *Nature Materials* **2011,** *10* (7), 539-544.

5. Yang, J.; Walczak, K.; Anzenberg, E.; Toma, F. M.; Yuan, G.; Beeman, J.; Schwartzberg, A.; Lin, Y.; Hettick, M.; Javey, A., Efficient and sustained photoelectrochemical water oxidation by cobalt oxide/silicon photoanodes with nanotextured interfaces. *Journal of the American Chemical Society* **2014,** *136* (17), 6191-6194.

6. Sun, K.; Shen, S.; Liang, Y.; Burrows, P. E.; Mao, S. S.; Wang, D., Enabling silicon for solar-fuel production. *Chemical Reviews* **2014,** *114* (17), 8662-8719.

7. Chen, L.; Yang, J.; Klaus, S.; Lee, L. J.; Woods-Robinson, R.; Ma, J.; Lum, Y.; Cooper, J. K.; Toma, F. M.; Wang, L.-W., p-Type transparent conducting oxide/n-type semiconductor

heterojunctions for efficient and stable solar water oxidation. *Journal of the American Chemical Society* **2015,** *137* (30), 9595-9603.

8. Zhou, H.; Yu, F.; Zhu, Q.; Sun, J.; Qin, F.; Yu, L.; Bao, J.; Yu, Y.; Chen, S.; Ren, Z., Water splitting by electrolysis at high current densities under 1.6 volts. *Energy & Environmental Science* **2018,** *11* (10), 2858-2864.

9. Bae, D.; Seger, B.; Vesborg, P. C.; Hansen, O.; Chorkendorff, I., Strategies for stable water splitting via protected photoelectrodes. *Chemical Society Reviews* **2017,** *46* (7), 1933-1954.

10. Hu, S.; Lewis, N. S.; Ager, J. W.; Yang, J.; McKone, J. R.; Strandwitz, N. C., Thin-film materials for the protection of semiconducting photoelectrodes in solar-fuel generators. *The Journal of Physical Chemistry C* **2015,** *119* (43), 24201-24228.

11. Oh, K.; Mériadec, C.; Lassalle-Kaiser, B.; Dorcet, V.; Fabre, B.; Ababou-Girard, S.; Joanny, L.; Gouttefangeas, F.; Loget, G., Elucidating the performance and unexpected stability of partially coated water-splitting silicon photoanodes. *Energy & Environmental Science* **2018,** *11* (9), 2590-2599.

12. McDowell, M. T.; Lichterman, M. F.; Carim, A. I.; Liu, R.; Hu, S.; Brunschwig, B. S.; Lewis, N. S., The influence of structure and processing on the behavior of TiO_2 protective layers for stabilization of n-Si/TiO_2/Ni photoanodes for water oxidation. *ACS Applied Materials & Interfaces* **2015,** *7* (28), 15189-15199.

13. Scheuermann, A. G.; Prange, J. D.; Gunji, M.; Chidsey, C. E.; McIntyre, P. C., Effects of catalyst material and atomic layer deposited TiO_2 oxide thickness on the water oxidation performance of metal–insulator–silicon anodes. *Energy & Environmental Science* **2013,** *6* (8), 2487-2496.

14. Scheuermann, A. G.; Lawrence, J. P.; Kemp, K. W.; Ito, T.; Walsh, A.; Chidsey, C. E.; Hurley, P. K.; McIntyre, P. C., Design principles for maximizing photovoltage in metal-oxide-protected water-splitting photoanodes. *Nature Materials* **2016,** *15* (1), 99-105.

15. Oh, S.; Oh, J., High performance and stability of micropatterned oxide-passivated photoanodes with local catalysts for photoelectrochemical water splitting. *The Journal of Physical Chemistry C* **2016,** *120* (1), 133-141.

16. Chen, Y.; Sun, K.; Audesirk, H.; Xiang, C.; Lewis, N. S., A quantitative analysis of the efficiency of solar-driven water-splitting device designs based on tandem photoabsorbers patterned with islands of metallic electrocatalysts. *Energy & Environmental Science* **2015,** *8* (6), 1736-1747.

17. Laskowski, F. A.; Oener, S. Z.; Nellist, M. R.; Gordon, A. M.; Bain, D. C.; Fehrs, J. L.; Boettcher, S. W., Nanoscale semiconductor/catalyst interfaces in photoelectrochemistry. *Nature Materials* **2020,** *19* (1), 69-76.

18. Hill, J. C.; Landers, A. T.; Switzer, J. A., An electrodeposited inhomogeneous metal–insulator–semiconductor junction for efficient photoelectrochemical water oxidation. *Nature Materials* **2015,** *14* (11), 1150-1155.

19. Loget, G.; Fabre, B.; Fryars, S.; Meriadec, C.; Ababou-Girard, S., Dispersed Ni nanoparticles stabilize silicon photoanodes for efficient and inexpensive sunlight-assisted water oxidation. *ACS Energy Letters* **2017,** *2* (3), 569-573.

20. Sun, K.; Ritzert, N. L.; John, J.; Tan, H.; Hale, W. G.; Jiang, J.; Moreno-Hernandez, I.; Papadantonakis, K. M.; Moffat, T. P.; Brunschwig, B. S.; Lewis, N. S., Performance and failure

modes of Si anodes patterned with thin-film Ni catalyst islands for water oxidation. *Sustainable Energy & Fuels* **2018,** *2* (5), 983-998.

21. Oh, S.; Song, H.; Oh, J., An optically and electrochemically decoupled monolithic photoelectrochemical cell for high-performance solar-driven water splitting. *Nano Letters* **2017,** *17* (9), 5416-5422.

22. Yu, X.; Yang, P.; Chen, S.; Zhang, M.; Shi, G., NiFe alloy protected silicon photoanode for efficient water splitting. *Advanced Energy Materials* **2017,** *7* (6), 1601805.

23. Xu, G.; Xu, Z.; Shi, Z.; Pei, L.; Yan, S.; Gu, Z.; Zou, Z., Silicon photoanodes partially covered by Ni@Ni(OH)$_2$ core–shell particles for photoelectrochemical water oxidation. *ChemSusChem* **2017,** *10* (14), 2897-2903.

24. Ying, Z.; Yang, X.; Tong, R.; Zhu, Q.; Chen, T.; He, Z.; Pan, H., Enhancing the Efficiency and Stability of NiO_x-Based Silicon Photoanode via Interfacial Engineering. *ACS Applied Energy Materials* **2019,** *2* (9), 6883-6890.

25. Kenney, M. J.; Gong, M.; Li, Y.; Wu, J. Z.; Feng, J.; Lanza, M.; Dai, H., High-performance silicon photoanodes passivated with ultrathin nickel films for water oxidation. *Science* **2013,** *342* (6160), 836-840.

26. Feng, J.; Gong, M.; Kenney, M. J.; Wu, J. Z.; Zhang, B.; Li, Y.; Dai, H., Nickel-coated silicon photocathode for water splitting in alkaline electrolytes. *Nano Research* **2015,** *8* (5), 1577-1583.

27. Medway, S.; Lucas, C.; Kowal, A.; Nichols, R.; Johnson, D., In situ studies of the oxidation of nickel electrodes in alkaline solution. *Journal of Electroanalytical Chemistry* **2006,** *587* (1), 172-181.

28. Hall, D. S.; Bock, C.; MacDougall, B. R., The electrochemistry of metallic nickel: oxides, hydroxides, hydrides and alkaline hydrogen evolution. *Journal of The Electrochemical Society* **2013,** *160* (3), F235.

29. Laskowski, F. A.; Nellist, M. R.; Venkatkarthick, R.; Boettcher, S. W., Junction behavior of n-Si photoanodes protected by thin Ni elucidated from dual working electrode photoelectrochemistry. *Energy & Environmental Science* **2017,** *10* (2), 570-579.

30. Bediako, D. K.; Lassalle-Kaiser, B.; Surendranath, Y.; Yano, J.; Yachandra, V. K.; Nocera, D. G., Structure–activity correlations in a nickel–borate oxygen evolution catalyst. *Journal of the American Chemical Society* **2012,** *134* (15), 6801-6809.

31. Trotochaud, L.; Ranney, J. K.; Williams, K. N.; Boettcher, S. W., Solution-cast metal oxide thin film electrocatalysts for oxygen evolution. *Journal of the American Chemical Society* **2012,** *134* (41), 17253-17261.

32. Mönch, W., On the alleviation of Fermi-level pinning by ultrathin insulator layers in Schottky contacts. *Journal of Applied Physics* **2012,** *111* (7), 073706.

33. Agrawal, A.; Lin, J.; Barth, M.; White, R.; Zheng, B.; Chopra, S.; Gupta, S.; Wang, K.; Gelatos, J.; Mohney, S. E., Fermi level depinning and contact resistivity reduction using a reduced titania interlayer in n-silicon metal-insulator-semiconductor ohmic contacts. *Applied Physics Letters* **2014,** *104* (11), 112101.

34. Digdaya, I. A.; Adhyaksa, G. W.; Trześniewski, B. J.; Garnett, E. C.; Smith, W. A., Interfacial engineering of metal-insulator-semiconductor junctions for efficient and stable photoelectrochemical water oxidation. *Nature Communications* **2017,** *8* (1), 1-8.

35. Cui, W.; Wu, S.; Chen, F.; Xia, Z.; Li, Y.; Zhang, X.-H.; Song, T.; Lee, S.-T.; Sun, B., Silicon/organic heterojunction for photoelectrochemical energy conversion photoanode with a record photovoltage. *ACS Nano* **2016,** *10* (10), 9411-9419.

36. Li, S.; She, G.; Chen, C.; Zhang, S.; Mu, L.; Guo, X.; Shi, W., Enhancing the photovoltage of Ni/n-Si photoanode for water oxidation through a rapid thermal process. *ACS Applied Materials & Interfaces* **2018,** *10* (10), 8594-8598.

37. Cowley, A.; Sze, S., Surface states and barrier height of metal-semiconductor systems. *Journal of Applied Physics* **1965,** *36* (10), 3212-3220.

38. Berg, S.; Andersson, L.; Norström, H.; Grusell, E., 2.2 Substrate surface damages by rf-sputtering. *Vacuum* **1977,** *27* (3), 189-191.

39. Mullins, F. H.; Brunnschweiler, A., The effects of sputtering damage on the characteristics of molybdenum-silicon Schottky barrier diodes. *Solid-State Electronics* **1976,** *19* (1), 47-50.

40. Digdaya, I. A.; Trześniewski, B. J.; Adhyaksa, G. W.; Garnett, E. C.; Smith, W. A., General considerations for improving photovoltage in metal–insulator–semiconductor photoanodes. *The Journal of Physical Chemistry C* **2018,** *122* (10), 5462-5471.

41. Dingemans, G.; Kessels, W., Status and prospects of Al_2O_3-based surface passivation schemes for silicon solar cells. *Journal of Vacuum Science & Technology A: Vacuum, Surfaces, and Films* **2012,** *30* (4), 040802.

42. Triendl, F.; Pfusterschmied, G.; Pobegen, G.; Konrath, J.; Schmid, U., Theoretical and experimental investigations of barrier height inhomogeneities in poly-Si/4H-SiC heterojunction diodes. *Semiconductor Science and Technology* **2020,** *35* (11), 115011.

43. Cimilli, F.; Sağlam, M.; Efeoğlu, H.; Türüt, A., Temperature-dependent current–voltage characteristics of the Au/n-InP diodes with inhomogeneous Schottky barrier height. *Physica B: Condensed Matter* **2009,** *404* (8-11), 1558-1562.

44. Nouchi, R., Extraction of the Schottky parameters in metal-semiconductor-metal diodes from a single current-voltage measurement. *Journal of Applied Physics* **2014,** *116* (18), 184505.

45. Nakato, Y.; Ueda, K.; Yano, H.; Tsubomura, H., Effect of microscopic discontinuity of metal overlayers on the photovoltages in metal-coated semiconductor-liquid junction photoelectrochemical cells for efficient solar energy conversion. *The Journal of Physical Chemistry* **1988,** *92* (8), 2316-2324.

46. Ohdomari, I.; Aochi, H., Size effect of parallel silicide contact. *Physical Review B* **1987,** *35* (2), 682.

47. Rossi, R. C.; Lewis, N. S., Investigation of the size-scaling behavior of spatially nonuniform barrier height contacts to semiconductor surfaces using ordered nanometer-scale nickel arrays on silicon electrodes. *The Journal of Physical Chemistry B* **2001,** *105* (49), 12303-12318.

48. Tung, R. T., The physics and chemistry of the Schottky barrier height. *Applied Physics Reviews* **2014,** *1* (1), 011304.

49. Rossi, R. C.; Tan, M. X.; Lewis, N. S., Size-dependent electrical behavior of spatially inhomogeneous barrier height regions on silicon. *Applied Physics Letters* **2000,** *77* (17), 2698-2700.

50. Nakato, Y.; Tsubomura, H., Silicon photoelectrodes modified with ultrafine metal islands. *Electrochimica acta* **1992,** *37* (5), 897-907.

51. Loget, G., Water oxidation with inhomogeneous metal-silicon interfaces. *Current Opinion in Colloid & Interface Science* **2019,** *39*, 40-50.

52. Gelderman, K.; Lee, L.; Donne, S., Flat-band potential of a semiconductor: using the Mott–Schottky equation. *Journal of chemical education* **2007,** *84* (4), 685.

53. Yao, T.; Chen, R.; Li, J.; Han, J.; Qin, W.; Wang, H.; Shi, J.; Fan, F.; Li, C., Manipulating the interfacial energetics of n-type silicon photoanode for efficient water oxidation. *Journal of the American Chemical Society* **2016,** *138* (41), 13664-13672.

54. Tung, R., Electron transport at metal-semiconductor interfaces: General theory. *Physical Review B* **1992,** *45* (23), 13509.

55. Poole, C.; Darwazeh, I., *Microwave active circuit analysis and design*. Academic Press: 2015.

56. Sullivan, J.; Tung, R.; Pinto, M.; Graham, W., Electron transport of inhomogeneous Schottky barriers: A numerical study. *Journal of applied physics* **1991,** *70* (12), 7403-7424.

Chapter 3

Imaging and improving hot-carrier extraction in plasmonic metal/semiconductor heterostructures

3.1 Introduction

Surface plasmons resonances (SPR) in metal nanostructures result from the collective oscillations of conduction electrons upon excitation by incident light.[1] Plasmonic metal nanoparticles exhibit several important characteristics making their wide application in photovoltaics, photocatalysis, and optoelectronic devices.[2-5] First, metal nanoparticles, especially Au and Ag, have tunable plasmon resonances at visible wavelengths.[2, 6, 7] Second, SPR in plasmonic nanostructures can concentrate light from the far field and enhance electromagnetic field intensities near the vicinity of the particles.[1, 8] Third, surface plasmons can also decay non-radiatively into hot electron–hole pairs. These energetic hot carriers can undergo interfacial charge transfer to mediate chemical reactions.[9]

The lifetimes of hot carriers in a plasmonic metal are extremely short, as they rapidly thermalize with the surrounding electron gas at a timescale of picoseconds.[10] This has led to extensive investigation of metal/semiconductor heterostructures for extracting excited hot carriers from plasmonic metal nanoparticles.[2, 4] In these systems, hot carriers with energies larger than the Schottky barrier are injected into the semiconductor; the internal field of the junction prevents the hot carriers from recombining.[11-13] Therefore, plasmonic nanostructures can photosensitize the semiconductor to extend solar absorption to the visible range by hot-electron injection, and have become a promising material system for solar-fuel production, such as water splitting to generate hydrogen fuel.[6, 14]

However, the reported hot-carrier collection efficiency is typically very low (< 1%).[12, 15-17] This low efficiency primarily comes from the intrinsic properties of metals, including ultrafast electron–electron scattering pathways and the broad distribution of hot-carrier energies, such that only a small portion of them have sufficient energies to be emitted into the semiconductor.[18, 19] It

has been found that the efficiency can be substantially improved through a direct charge-transfer mechanism when the electronic interaction between the metal nanostructure and semiconductor is strong.[20] Theoretical predictions have also suggested that an improvement in efficiency can be achieved by modifying the density of states of the metal nanostructure, which may be hard to implement in practice.[18]

Recently, another approach based on embedding plasmonic nanostructures into a semiconductor has been demonstrated to increase the conversion efficiency in a Schottky diode.[21, 22] Typically, the metal/semiconductor interface consists only of a planar junction, as the metal is usually deposited atop the semiconductor in the fabrication process. In this planar configuration, an electron can only be emitted across the junction if the normal component of its momentum is also large enough to overcome the energy barrier.[18] This means that even among the electrons that have kinetic energies above the barrier height, a large fraction of them may not be emitted due to momentum mismatch and are instead reflected back into the metal.[22, 23] Embedding plasmonic metal nanostructures into the semiconductor introduces vertical Schottky interfaces, which in principle allows a larger fraction of the excited hot-electron population to be extracted into the semiconductor.

Since embedding the Au nanostructures will result in additional Schottky interfaces, we aim to determine the relationship between embedded depth and photoresponse in the n-Si/Au photoelectrodes. This relationship has been demonstrated in solid-state Schottky diodes but not in a photoelectrochemical cell. Furthermore, the previously reported embedding approach is based on the initial formation of trenches using reactive ion etching (RIE), followed by Au deposition in the trenches. This process usually results in a smooth Schottky interface, which is also known to suppress Schottky photocurrent due to linear momentum conservation.[15] A higher conversion

efficiency of surface plasmons to photocurrent generation can be achieved by increasing the roughness at the Schottky contact.[15, 24] In this chapter, we apply metal-assisted chemical etching to embed pre-patterned Au nanoarrays in n-Si substrates. The vertical contact area between Au and Si is controlled by different etching times. We expect that this embedding method will increase the roughness of the Schottky interface. The n-Si/Au composite electrodes were characterized by atomic force microscopy (AFM) and scanning electron microscopy (SEM) to determine the embedded depth and surface morphology. The hot-carrier collection efficiency of each n-Si/Au photoelectrode was quantified using photoelectrochemical measurements.

The second goal of this chapter is to investigate the photochemistry of extracted hot carriers in plasmonic Au/TiO_2 heterostructures that are fabricated by lithography patterning. Specifically, we want to understand how local variations in the electromagnetic field intensity affect the spatial distribution of hot-carrier photochemistry. Photodeposition is an effective method for mapping hot carriers.[25-27] Photodeposition of Ag and PbO_2 were performed on Au/TiO_2 heterostructures to track where the electrons and holes are extracted. The distribution of the reactivity maps obtained from photodeposition can be correlated with electromagnetic simulations to determine the relative role of plasmon-enhanced absorption in hot-carrier extraction. We anticipate these studies will aid in the design of improved devices for solar energy conversion with enhanced efficiency for hot-carrier extraction.

3.2 Experimental

3.2.1 Materials and Fabrication of 2D Au Metal Arrays

Chemicals:

Sodium hydroxide (NaOH, ACS reagent, ≥ 97%), hydrogen peroxide (H_2O_2, with inhibitor, 30% (w/w) in H_2O), titanium diisopropoxide bis(acetylacetonate) (75 wt.% in isopropanol), titanium tetra-isopropoxide (97%), Iron (II) sulfate heptahydrate ($FeSO_4 \cdot 7H_2O$, ACS reagent, ≥ 99%), Iron (III) sulfate hydrate ($Fe_2(SO_4)_3 \cdot xH_2O$, 97%), resazurin sodium salt (dye content, ≥ 80%), sodium phosphate dibasic (Na_2HPO_4, ≥ 99.5%), sodium phosphate monobasic monohydrate (NaH_2PO_4, ≥ 99.5%), Triton X-100, sodium sulfate (Na_2SO_4, ACS reagent, ≥ 99.0%), methanol (ACS reagent, ≥ 99.8%), 1-butanol (ACS reagent, ≥ 99.4%), toluene (ACS reagent, ≥ 99.5%), sodium nitrate ($NaNO_3$, ACS reagent, ≥ 99%), silver nitrate ($AgNO_3$, ACS reagent, ≥ 99%), lead(II) nitrate ($Pb(NO)_3$, ACS reagent, ≥ 99%), and sodium persulfate ($Na_2S_2O_8$, ≥ 99%) were purchased from Sigma-Aldrich. Suspended latex microspheres with a diameter of 0.43 μm were purchased from Thermo Fisher Scientific. MIBK (methyl isobutyl ketone), 950 PMMA, anisole, LOR10B resist, Remover PG, and MF-319 developer were purchased from MicroChem Corp. S1805 positive photoresist was purchased from the Dow Chemical Company. Hydrofluoric acid (HF, 49 %) was purchased from the Transene Company, Inc. Platinum gauze (Pt, 100 mesh, 99.9% metals basis), and Pt wire (0.5 mm diameter, 99.95% metals basis) were purchased from Alfa Aesar. Single-crystal, n-type Si wafers with the (111) orientation (phosphorous-doped, single-side polished, and a resistivity range of 0.001 to 0.004 Ω cm) were purchased from Addison Engineering, Inc. Single-crystal, n-type Si wafers with the (100) orientation (phosphorous-doped, single-side polished, and a resistivity range of 1 to 10 Ω cm) were purchased from University Wafer. All chemicals were

used as received. Deionized (DI) water with 18.2 MΩ resistance was supplied from a Barnstead GenPure Pro water purification system.

Fabrication of ITO/Au nanoarray/TiO_2 electrodes by nanosphere lithography:

Indium tin oxide (ITO)-coated glass slides (8-12 Ω) were cut into 1 cm × 2.5 cm pieces using a diamond scribe. The cut substrates were first sonicated in 0.1 M NaOH solution for 10 min to render the surface of the substrate hydrophilic and then sonicated for another 10 min in ultrapure water. The cleaned ITO glass slides were stored in ultrapure water. Prior to use, the ITO substrates were vigorously rinsed with ultrapure water and blow-dried using N_2 gas. A schematic of the fabrication process using nanosphere lithography is shown in **Figure 3.1**. The first step is to prepare a 2D colloidal mask using latex microspheres with an average diameter of 0.43 µm. The microsphere suspension was diluted by a factor of 1.25 using a solution of Triton X-100 and methanol (1:400). This solution was spin-coated onto the ITO surface at 3600 rpm for 70 s to form a close-packed monolayer sphere mask. Metal thin films were deposited in a thermal evaporator (Edwards Auto 306) at a base pressure of 10^{-7} Torr. Approximately 2 nm of Ti (99.98%, Kurt J. Lesker) was first deposited at a rate of 0.1 nm/s as an adhesive layer, followed by 30 nm of Au (99.999%, Kurt J. Lesker) deposited at a rate of 0.1 nm/s. After Au deposition, the microsphere mask was physically removed using Scotch tape, revealing an array of Au triangles on the ITO electrode.

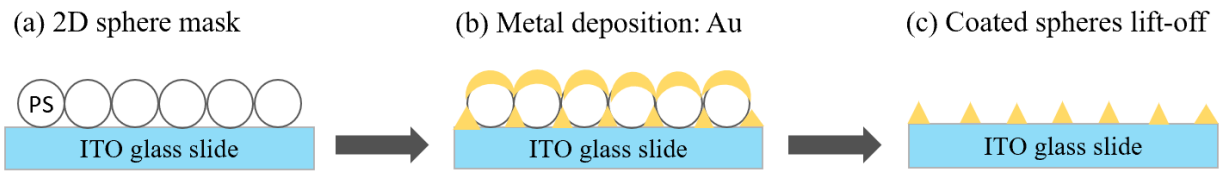

Figure 3.1 Schematic showing how nanosphere lithography was used to design ITO/Au nanoarray electrodes.

A TiO_2 sol was synthesized by the hydrolysis of 5 mL of titanium tetra-isopropoxide in 60 mL of an aqueous solution containing 425 µL of concentrated nitric acid, which was heated in an oven at 80°C for 10 h. The array of Au triangles was then coated with a layer of TiO_2 by spin-coating the prepared TiO_2 sol at 2000 rpm for 70 s on the Au-patterned ITO electrode. Finally, ITO/Au nanoarray/TiO_2 electrodes were annealed at 300°C in a muffle furnace for 1 h.

Fabrication of Si/TiO_2/Au nanoarray electrodes by nanosphere lithography & electron beam lithography:

In this configuration, a thicker TiO_2 film is first coated on the silicon substrate. Then, the lithography process is performed to pattern Au nanoarrays on the TiO_2 surface. The precursor solution used to prepare the TiO_2 film in these samples consists of diluting a solution of titanium diisopropoxide bis(acetylacetonate) (75 wt.% in isopropanol) to 0.15 M in 1-butanol. The precursor solution was spin-coated onto the silicon substrate at 1500 rpm for 70 s, followed by heating on a hot plate at 100°C for 5 min to evaporate the excess solvent. The substrate was then annealed at 450°C for 30 min in a muffle furnace. The Au nanoarrays patterned by nanosphere lithography followed the same procedure as described above, except that removal of the sphere mask after metal deposition was done by sonication in toluene instead of using Scotch tape.

We also used electron beam lithography to design and fabricate metal nanoarrays on the TiO_2 film. This method enables control over the size and shape of the individual Au nanostructures as well as their spacing. The overall process is schematically illustrated in **Figure 3.2**. First, a resist layer is deposited by spin-coating an anisole solution containing 4% 950k PMMA at 3000 rpm for 60 s. The substrate was then baked at 180°C for 2 min on a hot plate to remove excess solvent. Electron beam lithography was implemented using a JEOL 7001LVF scanning electron

microscope. Pattern writing software and a beam blanker were added to control which areas of the field are exposed. The designed patterns were first created using DesignCAD software (DesignCAD 3D Max 24) then input into the Nanometer Pattern Generation System (NPGS), which is used to control the electron beam and dosage during exposure. Prior to the electron beam writing, the substrate was first loaded into the SEM chamber, and the electron beam was focused using standard gold nanoparticles. The beam blanker was then employed and externally controlled by the NPGS to write the designed pattern into the resist layer of the sample. The accelerating voltage used was 30 kV. After electron beam exposure, the substrate was immersed in a MIBK (methyl isobutyl ketone)/isopropanol 1:3 developer for 60 s, immediately rinsed with a copious amount of water, and blow-dried gently with N_2 gas before mounting in the chamber of the thermal evaporator. The metal evaporation conditions were the same as described above, with a 2-nm adhesive layer of Ti evaporated first, followed by 30 nm of Au. The last step is removing the remaining resist via a lift-off process in acetone to reveal the designed Au nanoarray on the TiO_2-coated silicon substrate.

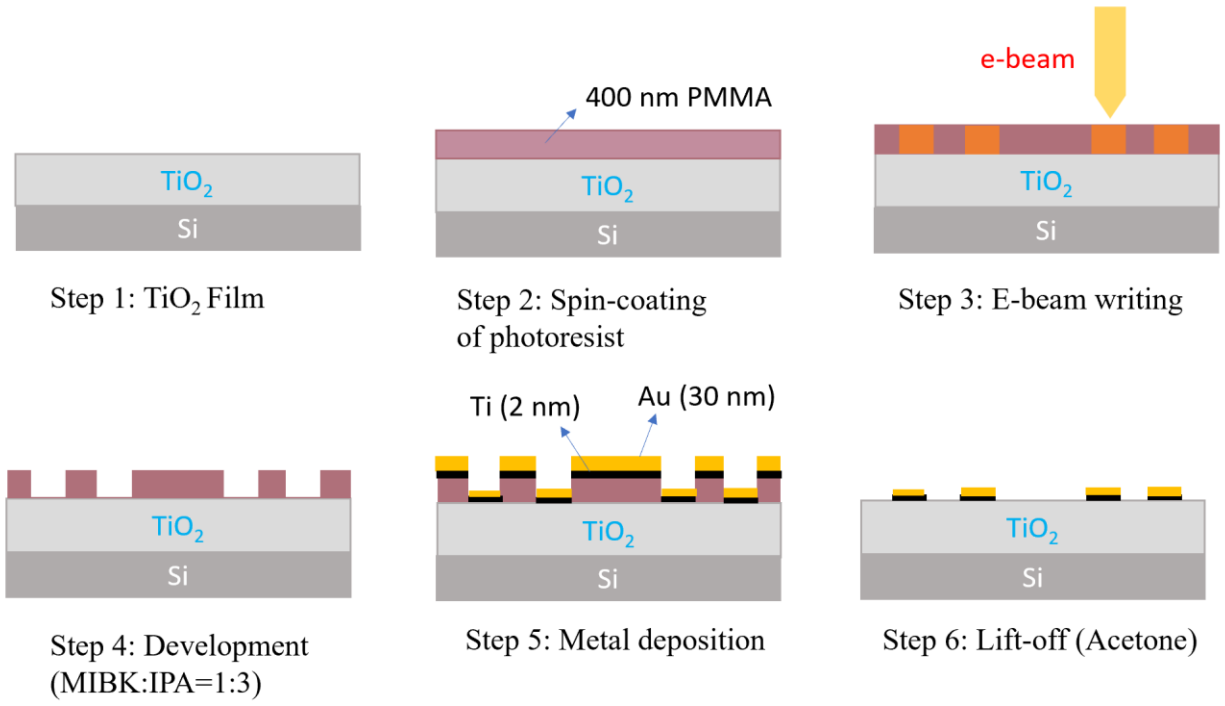

Figure 3.2 Schematic showing how electron beam lithography was used to design Si/TiO_2/Au nanoarray electrodes.

Fabrication of n-Si/embedded Au nanoarray electrodes using direct laser-write lithography:

Large-scale arrays of Au disks with a diameter of 700 nm were patterned on n-type silicon wafers by direct laser-write lithography. The laser writing process was conducted with a Heidelberg DWL 66+ laser writer, equipped with a 375-nm UV laser. The area of one electrode was designed to be 10 mm × 10 mm, with a 4 mm × 4 mm pattern located at the center. A whole, 4-inch wafer was processed at the same time to maintain consistency between different electrodes. The patterned wafer was cut into individual electrodes using a dicing saw (Disco model DAD 323).

The direct laser-write lithography process we implemented is illustrated in **Figure 3.3**. The initial steps consist of spin-coating the resist onto the silicon wafer. Two different layers of resists were used in this process. First, a lift-off resist (LOR-10B) was spin-coated on the silicon wafer (500 rpm, 20-s dispersal; 3000 rpm, 70-s spin) and soft baked at 195°C for 10 min. Then, a second

photoresist (S1805) layer was spin-coated on top of the LOR layer (500 rpm, 10-s dispersal; 6000 rpm, 50-s spin) followed by another soft bake at 115°C for 1 min. The substrate was then placed inside the laser-writer chamber. The patterns designed with AutoCAD were converted to writing-path code, which directs the laser to areas on the substrate to expose the photoresist. The exposure parameters for the mask were 10% focus, 100% intensity, 47-mW laser power, and 1% filter. The exposed photoresist was developed by immersing it in MIF-319 for 70 s, thoroughly rinsed using deionized H_2O, and blow-dried gently with N_2 gas. Due to different dissolution rates of the two resists in the developer, an undercut was formed at the pattern edge, which is critical to obtain a clean lift-off in the final step. After lift-off, 2 nm of titanium followed by 60 nm of gold were deposited onto the substrate using a thermal evaporator at a base pressure below 10^{-7} Torr. The final lift-off step was conducted at 60°C in Remover PG for 2 h, followed by sonication and a thorough rinse with deionized H_2O.

The n-Si/Au nanoarray electrodes were subjected to metal-assisted chemical etching (MACE) to embed the Au nanoarrays into the silicon substrate. The patterned wafer was first cut into 1 cm × 1 cm pieces with a dicing saw. Aqueous H_2O_2 was added to an aqueous HF/H_2O solution in a Teflon beaker to produce a solution of 5:2:1 HF(~49%):H_2O_2(~30%):H_2O immediately prior to immersing the n-Si/Au nanoarray electrodes. The etching time was varied from 5 to 40 s, and the etching reaction was stopped by removing the sample from the etching solution and quenching it with ultrapure water.

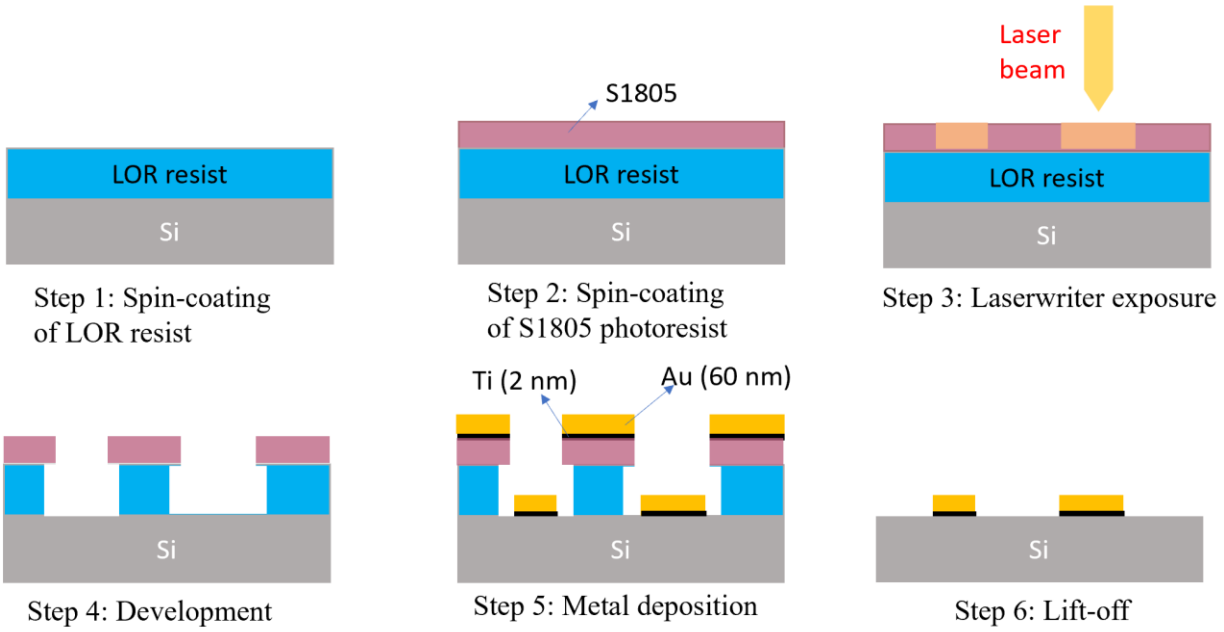

Figure 3.3 Schematic showing how direct laser-write lithography was used to design n-Si/embedded Au nanoarray electrodes.

3.2.2 Electrochemical Methods

Photoelectrochemical measurements

Electrochemical measurements were conducted in a custom electrochemical cell. The cell was made from borosilicate glass with three 14/20 ground glass joints at the top designed for a three-electrode configuration and a flat window on the side for illumination. Pt gauze was used as the counter electrode. The Pt gauze was attached to a Pt wire that was soldered to a tinned Cu wire, and the soldered joint was sealed in a glass tube. A silver/silver chloride (Ag/AgCl) electrode in 3 M NaCl was used as the reference electrode. Each working electrode was rinsed with ultrapure water and blow-dried with N_2 gas before use. The three electrodes were connected to a BioLogic VSP-300 potentiostat/galvanostat controlled using EC-Lab software (V11.33).

For the preparation of n-Si/Au nanoarray working electrodes, the Si substrates were assembled into electrodes by first scratching the backside of the Si substrate with an In–Ga eutectic alloy using a diamond scribe. A coiled tinned copper wire was pressed into the eutectic and then covered with conductive silver print (SPI supplies) to seal the wire to the Si substrate. The Cu wire was threaded through a glass tube, and the opening of the tube on the sample side was sealed with a grey epoxy (LOCTITE Hysol 9460™). The epoxy was dried for 2 h in a furnace at ~60°C. The Cu wire at the other end of the glass tube was connected to the potentiostat by an alligator clip. The backside and edges of the Si substrate, along with the exposed portion of the Cu wire, were covered with black nail polish and allowed to dry for at least 2 h.

Photoelectrochemical measurements were performed in an aqueous electrolyte containing 0.1 M $FeSO_4 \cdot 7H_2O$, 0.025 M $Fe_2(SO_4)_3 \cdot xH_2O$, and 1.0 M Na_2SO_4. The solution was purged with N_2 gas prior to the measurements and was continuously stirred during measurements with a magnetic stir bar at the bottom of the electrochemical cell. The photocurrent and photovoltage produced by each electrode were measured under illumination with a broadband ELH-type (Osram) halogen bulb filtered through a 400-nm long-pass filter in tandem with an IR filter. Cyclic voltammetry (CV), chronoamperometry, and photocurrent measurements were also performed in a solution containing 0.4 mM resazurin and 0.1 M sodium phosphate buffer with a pH of 7.4. All CV scans started at open circuit, were first swept in the positive direction to a potential of +0.1 V *vs.* Ag/AgCl, and then swept in the negative direction to −0.5 V. The scan rate was 20 mV s^{-1}.

Ag photoelectrodeposition:

Ag photoelectrodeposition was conducted in same electrochemical cell as described above, but the reference electrode was a coil of Ag wire instead of a fritted Ag/AgCl/NaCl half-cell. The deposition solution consisted of 10^{-4} M $AgNO_3$ and 0.1 M $NaNO_3$. Ag photoelectrodeposition was

carried out at an applied potential of −0.02 V vs. Ag under illumination with an ELH lamp (equipped with a 400-nm, long-pass filter) for 20 mins.

PbO_2 photodeposition

PbO_2 photodeposition was conducted on the Si/TiO_2/Au nanoarray substrates in the same electrochemical cell described above with no applied bias. The deposition solution contained 0.5 mM $Pb(NO)_3$ and $Na_2S_2O_8$ 10 mg/100 mL. The Si/TiO_2/Au nanoarray sample was immersed in the deposition solution and irradiated by an ELH lamp (equipped with a 400-nm, long-pass filter) for 40 mins under continuous stirring.

3.2.3 Details of Sample Characterization

Scanning electron microscopy (SEM) images were collected using a JEOL 7001LVF field emission scanning electron microscope operated at an acceleration voltage of 15 kV. For the ITO electrode samples, the conductive top surface of the substrate was connected to the SEM sample holder with copper tape to minimize charge buildup.

Atomic force microscopy (AFM) images were recorded by using a Bruker Dimension Icon AFM and using the scan-assist mode. The imaging analysis was performed using Gwyddion SPM data analysis software (v. 2.49).

Fluorescence spectroscopy was used to probe the electrochemical transformation of resazurin to resorufin using ITO/Au nanoarrays as the working electrode. The electrolyte solution consisted of 40 mM resazurin and 0.1 M sodium phosphate buffer. A halogen lamp was used to irradiate the ITO/Au electrode surface from the side window of the electrochemical cell under a constant potential. The system was under constant stirring with a stir bar at the bottom. Aliquots of approximately 1 mL were collected periodically over time using a needle and syringe. Each

aliquot was first diluted by 100 times, and fluorescence spectra were measured in a quartz cuvette using a Cary Eclipse Spectrometer.

Reflectance spectra of the n-Si/Au samples after different etching times were acquired using a Cary 5000 spectrometer equipped with a 150-mm, external integrating sphere. Each Si substrate was taped to the back of an aperture that was placed at the rear port of the integrating sphere. A PMT detector was used for ultraviolet (UV) and visible wavelengths (250 – 800 nm), and a lead sulfide detector was used for near infrared (NIR) wavelengths (800 – 1200 nm). A tungsten halogen lamp was used as the source for visible and NIR wavelengths (350 – 1200 nm), and a deuterium lamp was used for the UV region (250 – 350 nm). The scan rate for each measurement was 300 nm/min, and the step size was 1.0 nm.

3.3 Results and Discussion

3.3.1 Fabrication and Photoelectrochemical Measurements on ITO/Au nanoarray/TiO_2 Heterostructures

Au nanoarrays were fabricated on ITO-coated glass slides using nanosphere lithography in which a close-packed monolayer of latex microspheres (diameter = 0.43 μm) was used as a mask for metal deposition. The sphere mask was prepared by spin-coating the microsphere solution diluted with a TritonX-100/methanol mixture (1:400) onto the ITO substrate. We tested a series of dilution factors ranging from 0.75 to 2 and observed that by using a dilution factor of 1.25, a close-packed monolayer of microspheres was formed as shown in **Figure 3.4 a**. Lower dilution factors resulted in multilayers of microspheres. On the other hand, if the microsphere solution was too dilute, the microspheres were sparsely dispersed on the substrate instead of close-packed. Au was evaporated through the interstitials between the microspheres onto the ITO surface resulting in a

hexagonal array of nanotriangles. Using a 2-nm adhesion layer of Ti makes the adhesion of the evaporated Au nanostructures on the ITO surface quite robust. So, we were able to remove the microspheres physically after metal evaporation with Scotch tape. An SEM image of the Au nanoarrays on an ITO-coated glass slide after removal of the microspheres is shown in **Figure 3.4 b**. The predominant structures are "bowties" or pairs of metal triangles that can be patterned over a large area using nanosphere lithography.

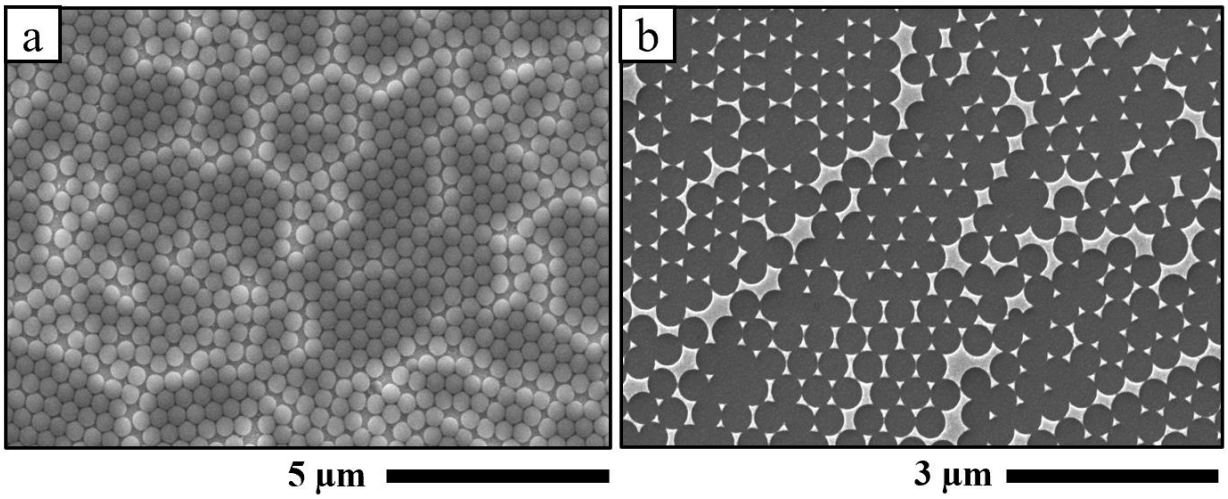

Figure 3.4 SEM images of (a) close-packed, 0.43 µm microspheres deposited on an ITO-coated glass slide, (b) Au nanoarrays on an ITO-coated glass after removal of the microspheres. The thickness of the Au nanostructures is 30 nm. The scale bars under images a and b are 5 µm and 3 µm, respectively.

A layer of TiO_2 was then deposited on the Au nanoarray to construct an ITO/Au nanoarray/TiO_2 heterostructure. The TiO_2 film is prepared using a sol-gel method in which a hydrolyzed solution of titanium tetra-isopropoxide is spin-coated onto each substrate, followed by thermal annealing. SEM images of the fabricated ITO/Au nanoarray/TiO_2 photoelectrode after thermal annealing are shown in **Figure 3.5**. The top-down view demonstrates that the triangular morphology of the Au nanostructure was preserved after annealing (**Figure 3.5 a**). A cross-

sectional SEM image showed that a uniform and continuous TiO_2 film with a thickness of ~20 nm was successfully coated onto the Au nanoarray (**Figure 3.5 b**). The TiO_2 layer on top of the array of Au nanostructures is not only essential for hot-electron injection, but the thermal process used to anneal the TiO_2 layer could also be beneficial in enhancing the plasmonic effect in the underlying Au nanostructures. Most lithographically patterned nanostructures are polycrystalline or amorphous due to the fast atomic deposition rate.[28] Polycrystalline metals possess many crystal defects and grain boundaries that have been reported to decrease the surface plasmon enhanced electric field intensity and electron–phonon relaxation time compared to single-crystalline metals.[29] The evaporated polycrystalline Au could be transformed into nearly single-crystalline ones with better plasmonic properties during the TiO_2 thermal annealing process.[28] Moreover, without the protection of a TiO_2 layer, after high-temperature treatment at 300°C in air for 1 h, the array of triangular Au nanoparticles became rounded and eventually turned into spherical particles (**Figure 3.5 b**). This phenomenon is driven by the natural tendency to reduce the total interfacial energy of the system.[30] By covering the Au nanostructures with a layer of TiO_2, the sharp tips of the Au nanotriangles can be preserved during thermal annealing (**Figure 3.5 a**).

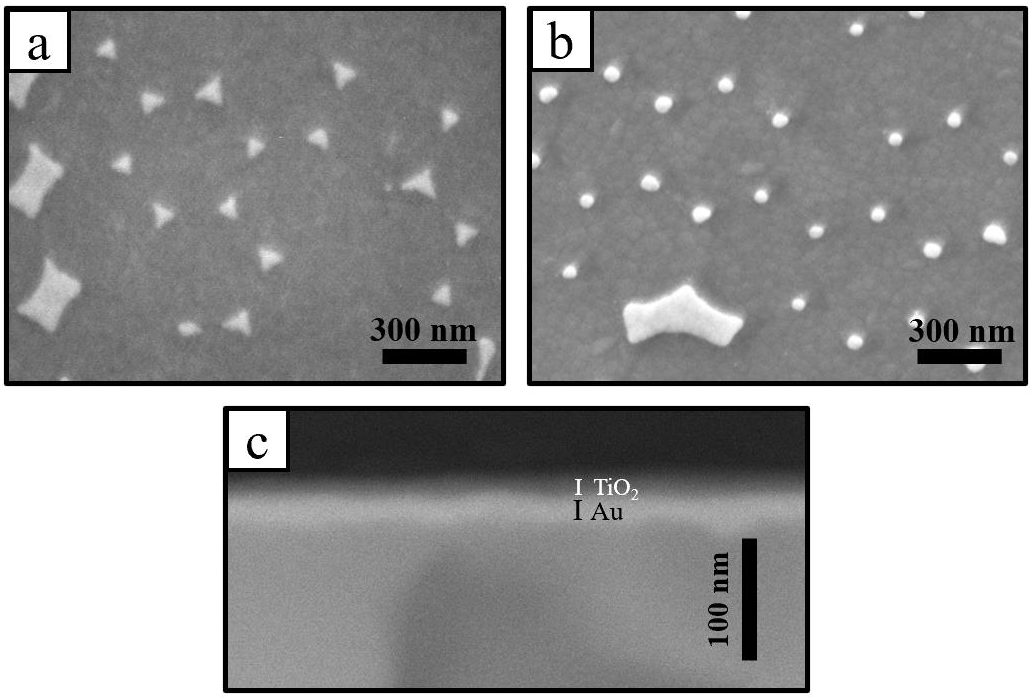

Figure 3.5 SEM images of Au nanotriangles fabricated on an ITO-coated glass slide (a) after thermal annealing with a thin TiO_2 layer deposited on the Au nanoarray; (b) after annealing without a TiO_2 coating. (c) Cross-sectional image of the ITO/Au/TiO_2 electrode. The scale bars in images a and b are both 300 nm, while the scale bar in image c is 100 nm.

We next tested the photoelectrochemical properties of the fabricated ITO/Au nanoarray/TiO_2 heterostructures. The photoelectrodes were immersed in a solution of $FeSO_4$ and $Fe_2(SO_4)_3$, which is a reversible, one-electron redox couple. **Figure 3.6 a** shows the photocurrent of this sample when illuminated by a halogen lamp equipped with a 400-nm, long-pass filter that allows only photon energies below the bandgap of TiO_2 to pass through. Thus, the light incident upon the electrode can excite the Au nanostructures without exciting the TiO_2 layer. **Figure 3.6 b** shows the shift in potential upon illumination measured at open circuit. It is known that n-type semiconductor electrodes, such as TiO_2, show anodic photocurrents and negative photopotentials.[31] Here, we observed an inverted output in our ITO/Au nanoarray/TiO_2 photoelectrode with a cathodic photocurrent and a positive open-circuit photopotential under

visible light illumination. As the Au nanoarrays are buried under the TiO_2 film, and the incident light only excites the Au nanoarray, this observation supports hot-electron injection from the plasmonically excited Au nanostructures to the TiO_2 film, resulting in reduction of the $Fe^{3+/2+}$ redox couple in the electrolyte.

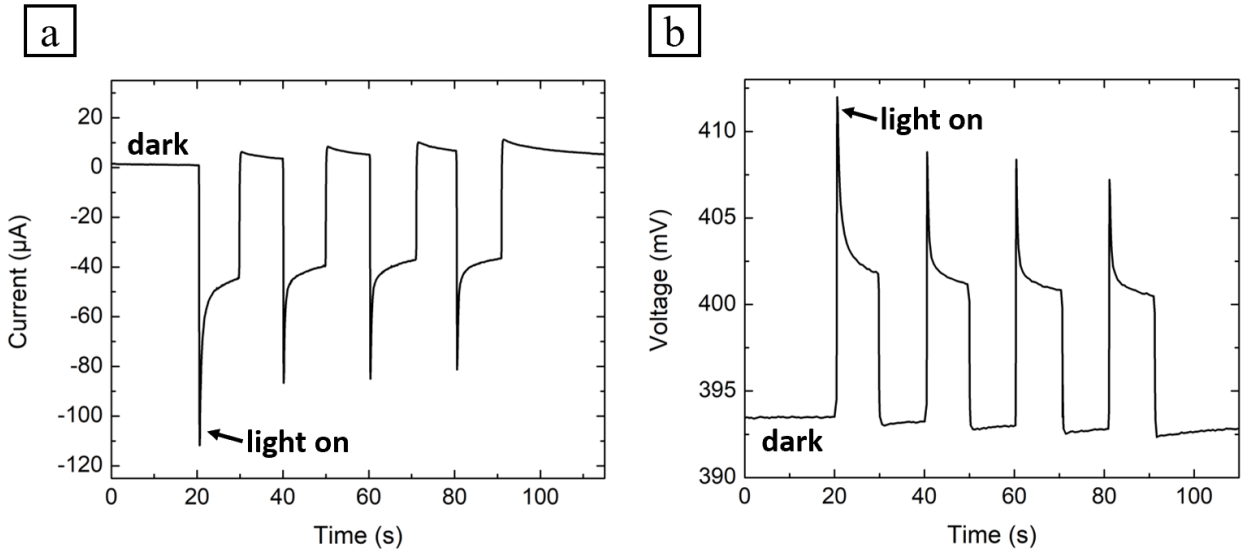

Figure 3.6 (a) Photocurrent and (b) photovoltage responses of an ITO/Au nanoarray/TiO_2 electrode under illumination with visible light.

We then replaced the $Fe^{3+/2+}$ redox couple with the resazurin/resorufin couple, to test the possibility to measure hot-electron injection using fluorescence spectroscopy and microscopy. The chemical structure of these molecules is shown in **Figure 3.7 a**. This redox couple was chosen because resazurin is weakly fluorescent and becomes highly fluorescent once transformed to resorufin. The suitability of this redox couple for measuring and imaging plasmon-induced hot electron transfer in the Au/TiO_2 heterostructure was tested by electrochemical measurements and fluorescence spectroscopy. We first evaluated the electrochemistry of the ITO/Au nanoarray photoelectrode patterned by nanosphere lithography in a solution containing 40 μM resazurin and

0.1 M sodium phosphate buffer (pH~7.4). Cyclic voltammograms for both an ITO/Au nanoarray electrode and a bare ITO electrode in the dark are shown in **Figure 3.7 b**. An irreversible reduction wave at -0.2 V *vs.* Ag/AgCl was observed using the ITO/Au nanoarray electrode, which corresponds to the reduction of resazurin to resorufin.[32] The reversible redox wave with a half-wave potential observed close to -0.3 V *vs.* Ag/AgCl is due to the reversible transformation between resorufin and dihydroresorufin.[32] To further verify the electrochemical reduction of resazurin to resorufin with the ITO/Au nanoarray working electrode, we performed bulk electrolysis by applying a constant potential of -0.35 V *vs.* Ag/AgCl in a solution containing 40 mM resazurin and 0.1 M sodium phosphate buffer. Aliquots were collected at several time intervals to measure the fluorescence intensity of the product resorufin. A color change was also observed from blue (resazurin) to pink (resorufin) during the transformation. From the fluorescence spectra (**Figure 3.8 a**), we can see that the intensity of the fluorescence band of resorufin at 585 nm increases with time, consistent with the expected redox chemistry.

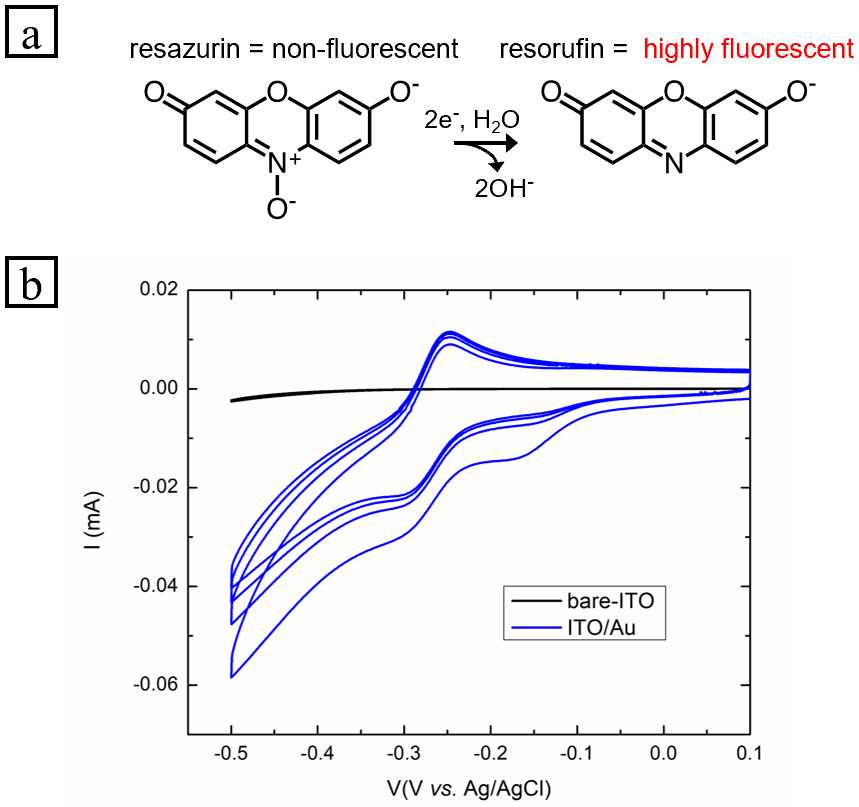

Figure 3.7 (a) The reduction of non-fluorescent resazurin to highly fluorescent resorufin. (b) Cyclic voltammograms for the resazurin/resorufin redox couple using an ITO/Au nanoarray electrode (blue trace) and bare ITO (black trace) as the working electrode. The CV scans were measured at a scan rate of 20 mV s^{-1}.

The photoresponses of ITO/Au nanoarray electrodes under illumination with visible light (ELH lamp, light intensity of 488 mW/cm^2) were tested using the photoelectrochemical cell described above. The electrolyte contained 0.4 mM resazurin in 0.1 M sodium phosphate buffer. **Figure 3.8 b** shows the photocurrent responses of an ITO/Au nanoarray electrode and a bare ITO electrode with the light switched on and off. The photocurrent generated by the ITO/Au nanoarray electrode under illumination was about −0.02 mA, whereas the bare ITO electrode generated negligible photocurrent. We attribute the difference in photocurrent between the ITO/Au nanoarray and the bare ITO electrode to the plasmonic effect of the Au nanoarrays. However,

when an ITO/Au nanoarray/TiO_2 photoelectrode was tested in the same resazurin containing solution, there was no observable photocurrent under the illumination of visible light. The observation of photocurrent using the same ITO/Au nanoarray/TiO_2 photoelectrode with the $Fe^{3+/2+}$ redox couple indicates the hot electrons injected into the TiO_2 layer from the plasmonically excited Au nanostructures cannot be used to reduce resazurin in the electrolyte.

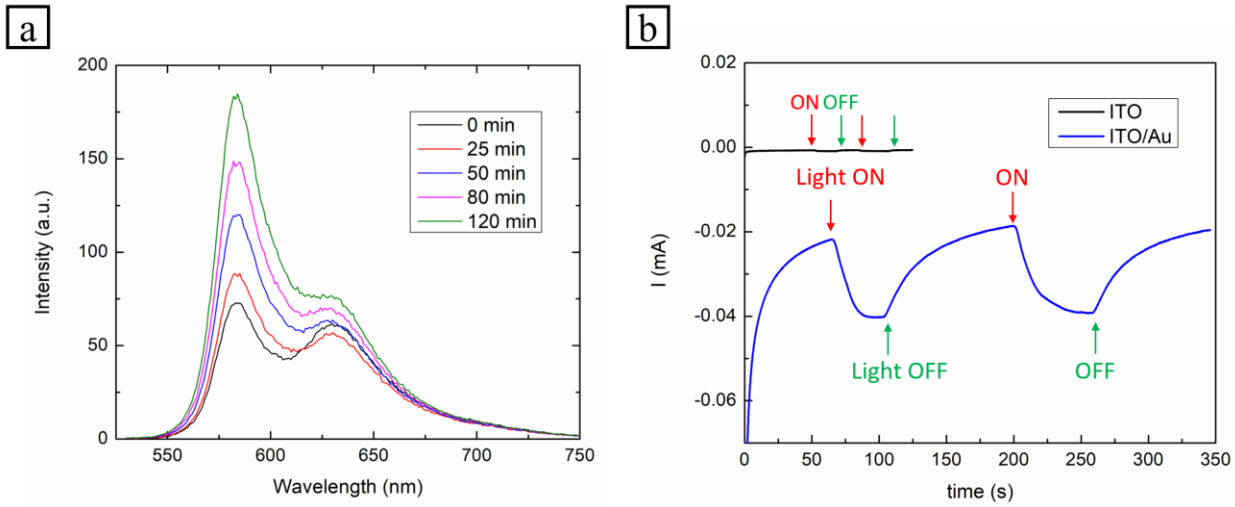

Figure 3.8 (a) Fluorescence spectra showing the transformation of resazurin to resorufin after 0 min, 25 min, 50 min, 80 min, and 120 min of electrochemical reduction under a constant applied potential at −0.35 V *vs.* Ag/AgCl using an ITO/Au nanoarray as the working electrode. (b) Photocurrent enhancement under ELH-lamp illumination at 488 mW cm^{-2}. Current response of the ITO/Au electrode (blue trace) and the bare-ITO electrode (black trace) at an applied potential of −0.35 V *vs.* Ag/AgCl. The lamp was turned on and off as indicated.

Photocurrent enhancement in ITO electrodes with thermally evaporated Au islands in contact with the $Fe(CN)_6^{3-/4-}$ redox couple has been demonstrated in previous studies.[33] Hot carriers and heat generated from plasmonic decay following the excitation of Au nanoparticles were both found to contribute to the photocurrent enhancement. Accordingly, under the high-intensity illumination from an ELH lamp, a large portion of the observed photocurrent from the ITO/Au nanoarray electrodes in our work could be due to the photothermal heating effect. The contribution from the different plasmon decay pathways is hard to differentiate. However, in the

ITO/Au nanoarray/TiO_2 system, measuring photocurrents only from hot carriers generated by plasmonically excited Au nanostructures can be achieved. In this electrode configuration, the coated TiO_2 film prevents the Au nanostructure from directly contacting the redox couple in solution. This eliminates the contribution from the photothermal heating effect as well as the catalytic effect from the Au nanoarrays. Unfortunately, the electrochemical experiments we performed with the ITO/Au nanoarray/TiO_2 photoelectrode indicated that the resazurin/resorufin redox couple is not suitable for measuring interfacial hot-carrier transfer in our ITO/Au nanoarray/TiO_2 heterostructure system.

3.3.2 Mapping Hot Carrier Photochemistry in ITO/Au nanoarray/TiO_2 and Si/TiO_2/Au nanoarray Heterostructures

A major goal in this chapter is to image the photochemistry of hot carriers in lithographically patterned plasmonic Au/TiO_2 heterostructures. In the previous section, the experimental results show that the resazurin/resorufin redox couple is not applicable for imaging hot-electron injection in the ITO/Au nanoarray/TiO_2 system using fluorescence microscopy. Another method that could also provide insight into hot-carrier photochemistry with nanoscale spatial resolution is photodeposition. Herein, we mapped the extraction of hot carriers through the photodeposition of metal and metal oxides. The precipitates are formed at locations that correspond to where the electrons or holes are extracted from the Au/TiO_2 composite. We used the photoelectrodeposition of Ag^+ to track the fate of extracted hot electrons in ITO/Au nanoarray/TiO_2 heterostructures. **Figure 3.9 a** illustrates the expected charge transport in this system. Photoelectrodeposition was conducted in an electrolyte solution consisting of $NaNO_3$ and $AgNO_3$ under a small negative applied potential (-0.01 to -0.02 V *vs.* Ag/AgCl) and visible light

illumination. An SEM image of the ITO/Au nanoarray/TiO_2 photoelectrode after Ag photoelectrodeposition is shown in **Figure 3.9 b**. The Ag nanoparticles deposited on the TiO_2 layer are found to form preferentially around the sharp edges of the underlying Au nanostructures. Recent studies have demonstrated that electromagnetic field distribution around the plasmonic nanostructures strongly affects local photochemistry.[26, 34] Thus, we attribute the larger amount of Ag precipitate resulting from the reduction of Ag^+ by hot electrons near the tips of the Au nanostructures to the higher electromagnetic field intensities at these locations. We simulated the electric field intensity profiles of Au nanoparticle dimers using the Finite Difference Time Domain (FDTD) method (**Figure 3.10**). The simulated electromagnetic field distribution is non-uniform and correlates well with the photoelectrodeposition experiments in which higher activities were observed near the tips of the Au nanostructures.

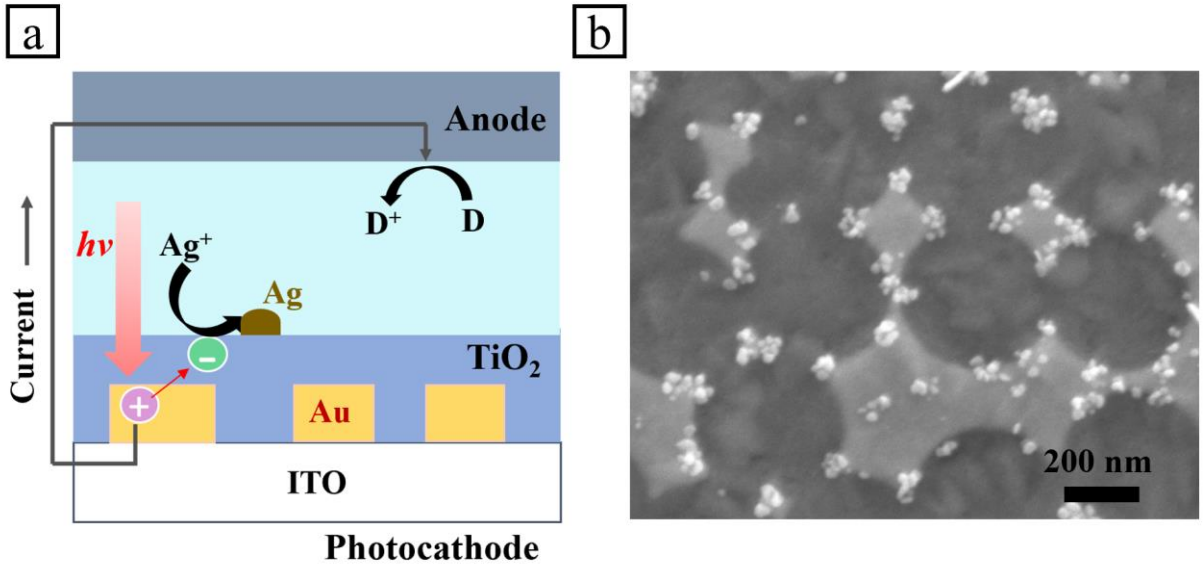

Figure 3.9 (a) Schematic illustration for charge transport in an electrochemical cell with an ITO/Au nanoarray/TiO_2 photocathode. (b) SEM image of the ITO/Au nanoarray/TiO_2 photocathode after photoelectrodeposition of Ag under visible light (> 400 nm).

To track the extracted hot holes in the Au/TiO_2 heterostructure by photodeposition, we fabricated the inverse heterostructure. That is, the array of Au nanostructures were patterned on top of the TiO_2 layer instead of being buried underneath it. In this configuration, a smooth TiO_2 film was first prepared on a silicon substrate using a sol-gel method, and then the lithography process was performed to pattern Au nanoarrays on the TiO_2 surface. More details for the fabrication of the Si/TiO_2/Au nanoarray heterostructures are given in the **Experimental Section 3.2.1**. An SEM image in **Figure 3.11 a** showed that Au nanostructures were successfully patterned onto the TiO_2 surface. The thickness of the TiO_2 film is approximately 100 nm, as indicated by cross-sectional SEM image (**Figure 3.11 b**).

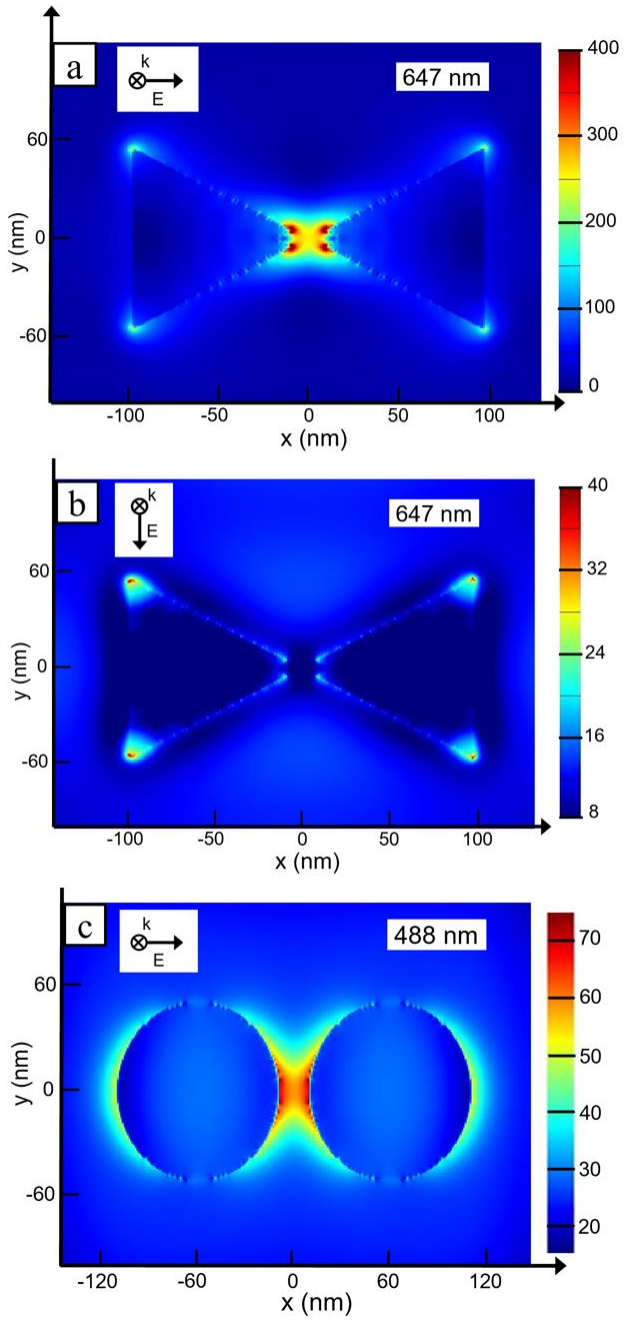

Figure 3.10 Electric field intensity profiles of Au nanoparticle dimers supported on a glass substrate in air simulated using the FDTD method. The thickness of the Au nanoparticles is 30 nm. (a, b) Electric field enhancement for Au nano-bowties with 100 nm edge lengths under 647 nm, plane wave illumination with the polarization (a) parallel, and (b) perpendicular to the dimer axis. (c) Electric field enhancement for dimers of Au disks with a 100-nm diameter and a 50-nm gap under 488 nm, plane wave illumination with the polarization parallel to the dimer axis.

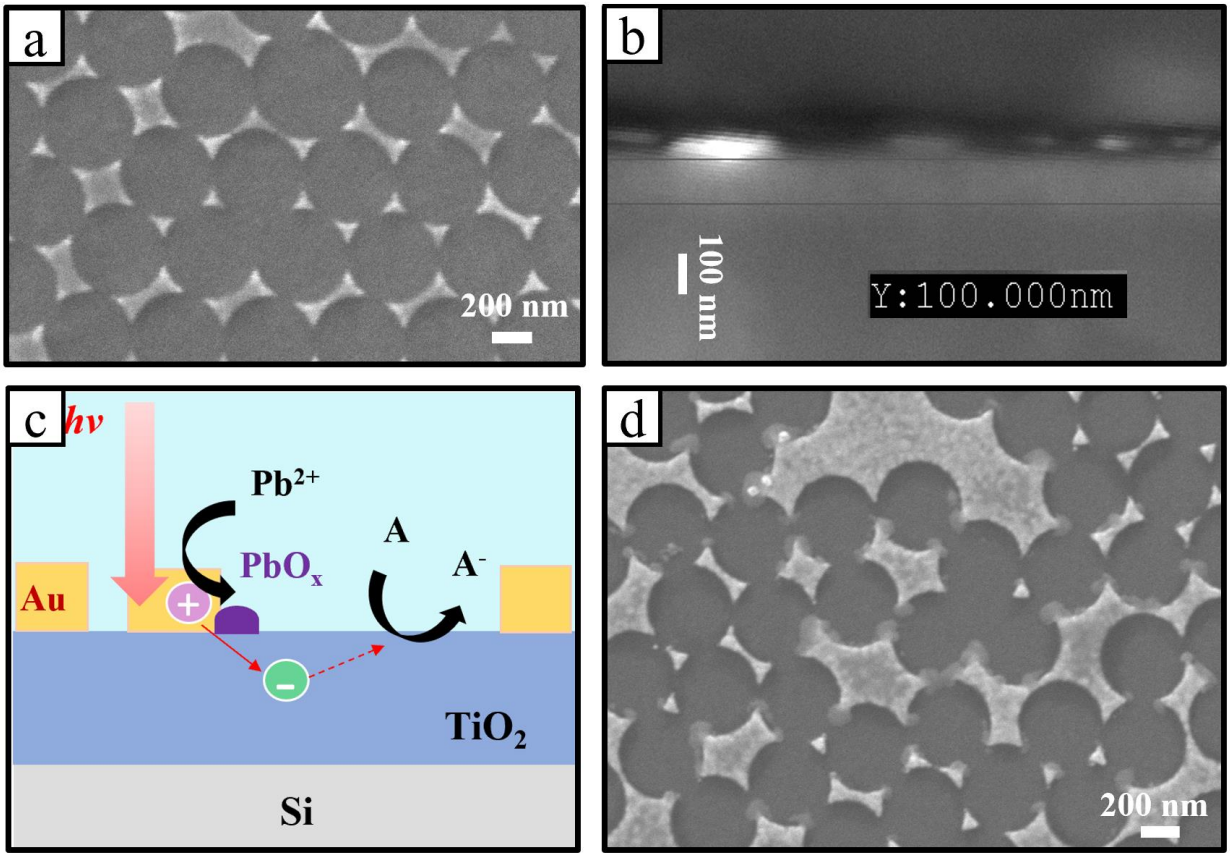

Figure 3.11 (a) SEM image of Au nanotriangles fabricated on a TiO_2 film prepared by a sol-gel method. (b) Cross-sectional image of the Si/TiO_2/Au nanoarray sample. The thickness of the TiO_2 layer is ~100 nm. The thickness of the Au nanostructures is 30 nm. (c) Schematic illustration of PbO_2 photodeposition on a Si/TiO_2/Au nanoarray sample. (d) SEM image of the Si/TiO_2/Au nanoarray sample after PbO_2 photodeposition.

Reactivity maps of hot holes generated by excitation of the Au nanostructures were obtained from the photodeposition of PbO_2 under visible light illumination (> 400 nm). A schematic of the expected charge transport in this process is shown in **Figure 3.11 c**. Photodeposition experiments were conducted in a solution containing $Pb(NO)_3$ and $Na_2S_2O_8$, which serve as the precursor and electron acceptor for PbO_2 photodeposition, respectively. The reaction for photodepositon is shown below:[25]

Photoexcitation: $TiO_2/Au + 6hv \rightarrow 6e^- + 6h^+$

Photooxidation: $3Pb^{2+} + 6H_2O + 6h^+ \rightarrow 3PbO_2 \downarrow +12H^+$

$$S_2O_8{}^{2-} + 2e^- \rightarrow 2SO_4{}^{2-}$$

Figure 3.11 d shows an SEM image of the Si/TiO_2/Au nanoarray sample after PbO_2 photodeposition. Similar to the Ag photoelectrodeposition, the PbO_2 precipitates formed preferentially near the sharp tips of the Au nanostructures, indicating the reactivity of hot holes is strongly affected by local electric field intensities.

The experiments described above were performed on Au nanostructures patterned using nanosphere lithography. To gain further insight into how the spatial distribution of hot-carrier photochemistry depends on local variations in electromagnetic field intensity, the size and shape of the Au nanostructures need to be precisely controlled. Specifically, we aim to explore the effect of plasmonic coupling on hot-carrier photochemistry. As demonstrated in **Figure 3.10**, significant electromagnetic field enhancements can be obtained between two Au nanoparticles in close proximity. Thus, we employed electron beam lithography to pattern Au nanoparticle dimers with controlled interparticle spacings. Details of the fabrication process can be found in **Experimental Section 3.2.1**. A designed Au pattern fabricated by electron beam lithography on an ITO coverslip is shown in **Figure 3.12**. The feature size of the patterned Au nano-bowties is between 200 and 400 nm, with a gap less than 100 nm.

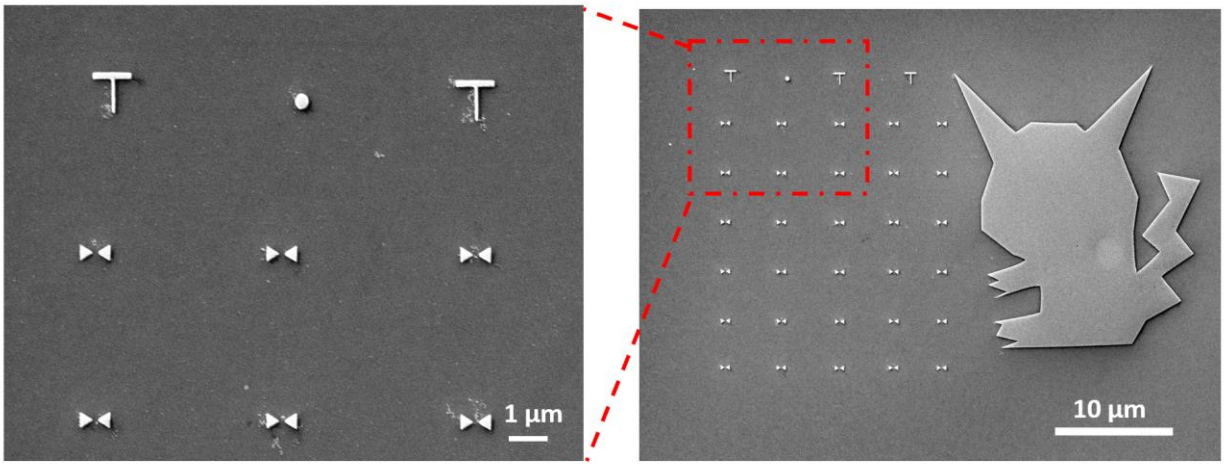

Figure 3.12 SEM images of Au nanoarrays on an ITO coverslip fabricated by electron beam lithography. The thickness of the Au patterns is 30 nm.

Electron beam lithography is a powerful method for fabricating customized nanoscale patterns with high resolution. However, nanoscale features, especially those less than 400 nm, are highly sensitive to multiple parameters during the lithography process. Typical parameters such as the thickness of the resist, the electron beam exposure dosage, development time, and temperature are all critical. The fact that the parameters are mutually dependent makes the optimization process especially challenging. For example, the required exposure dosage depends on the thickness of the resist; a thicker resist requires a higher dosage to get through. Even with a resist of the same thickness, the required exposure dosage is determined by the size of the designed feature. In general, a higher dosage is needed for smaller features. If the exposure dosage is not sufficient, the exposed resist will not be fully developed, which leads to the undercutting of undeveloped resists beneath the exposed area during lift-off. Another difficulty in this process comes from the operation of SEM to write patterns. A small probe current is desired for small features, as theoretically the lower the probe current the higher feature resolution can be achieved. Nonetheless, during the actual SEM operation, one would find that the lower the probe current, the harder it is

to tune the focus. Under our SEM operational conditions, we found the lowest probe current in which we are still able to achieve fine focus was between 30 and 35 pA. Thus, this is the current we used to write all the patterns by electron beam lithography in this work.

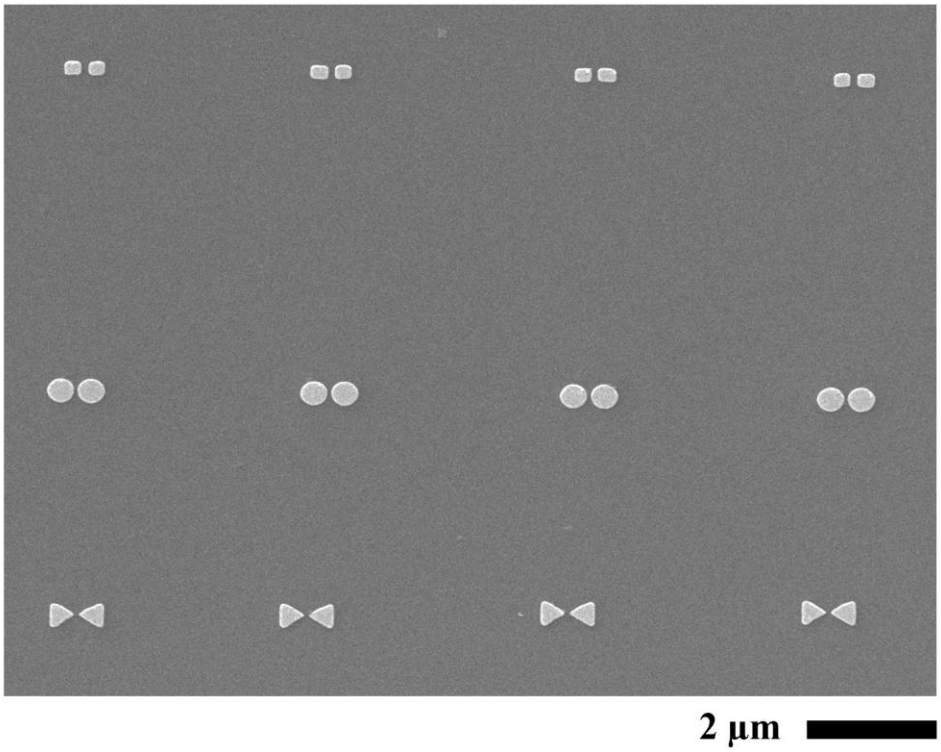

Figure 3.13 Array of Au nanostructure dimers patterned on a TiO_2 film by electron beam lithography. The edge lengths of the Au nano-bowties are 400 nm; the diameters of the Au disks are 400 nm with a 50 nm gap between dimers. The thickness of the Au nanoparticles is 30 nm.

We have also adjusted the parameters and successfully performed electron beam lithography on the TiO_2 films we synthesized. **Figure 3.13** shows the fabricated arrays of Au nanostructure dimers on TiO_2. The Au dimers were designed to correlate with the electric field intensity profiles we simulated (**Figure 3.10**), and the gaps between dimers were made as small as possible (close to 50 nm). However, photodeposition experiments conducted on the $Si/TiO_2/Au$ nanoarray samples fabricated by electron beam lithography were not successful. No precipitates

were observed to form in any of the patterned areas. This was found to be due to electron beam damage of the TiO_2 surface during the SEM imaging step before photodeposition.[35, 36]

3.3.3 Effect of Interfacial Geometry on Hot-Carrier Collection in n-Si/Au nanoarray Photoelectrodes

Embedding Au nanostructures into a semiconductor has been demonstrated to enhance hot-electron emission in Schottky diodes. In this study, we aim to determine the relationship between the embedded depth and hot-carrier collection efficiency in the n-Si/Au nanoarray photoelectrodes. We first applied metal-assisted chemical etching to n-Si/Au nanoarray samples that were fabricated by nanosphere lithography. Metal-assisted chemical etching is a highly anisotropic etching process for silicon that is catalyzed by metals, such as Au, Pt, or Ag. The etchant typically consists of diluted hydrofluoric acid and hydrogen peroxide (HF/H_2O_2). In this study, Si etching is catalyzed by Au particles, in which the surface of a Au particle immersed in the etching solution acts as the cathode for H_2O_2 reduction, while the interface with the Si substrate acts as the anode and catalyzes Si oxidation.[37, 38] The potential difference between the cathode and anode drives the overall reaction:

$$\mathrm{Si} + 2\mathrm{H_2O_2} + 6\mathrm{HF} \rightarrow \mathrm{H_2SiF_6} + 4\mathrm{H_2O}$$

Thus, the etching process is localized at the regions of the Si substrate covered by Au particles and results in the "sinking" of the Au nanostructures into the Si substrate.

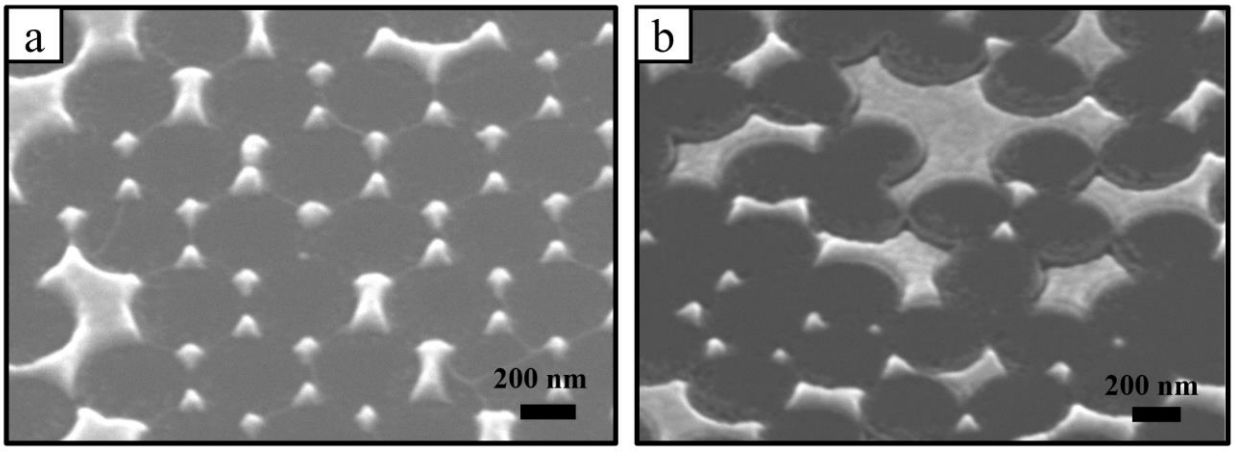

Figure 3.14 SEM images of the Au nanoarrays fabricated on n-type Si (111) after etching with a diluted HF/H_2O_2 solution (a) for 5 s, and (b) for 40 s. The thickness of the Au nanostructures is 60 nm.

Figure 3.14 shows SEM images of n-Si/Au nanoarray photoelectrodes after different metal-assisted chemical etching times. Comparing the photoelectrode etched for 40 s with the one that was only etched for 5 s, we can see that this etching method indeed results in embedded Au nanostructures. Also, we observed nearly no lateral movement or detachment of the nanostructures after etching under the SEM. The reduced migration may be due to the Ti adhesion layer, as this benefit of using a Ti layer has been previously reported.[39] The photoresponses of these two photoelectrodes were measured in a solution containing a $Fe^{3+/2+}$ redox couple. The electrode that was etched for 40 s to produce embedded Au nanostructures generated a larger photocurrent under visible light illumination. However, because the Au nanostructures patterned by nanosphere lithography have different sizes and shapes, the etching rates under each Au structure are different, which has also been demonstrated in previous studies.[40, 41] Due to the randomized Au patterns and different embedded depths of the Au nanostructures within a sample, we are unable to quantify the dependence of photocurrent response in the n-Si/Au nanoarray photoelectrodes with different embedded depths.

We next used direct laser-write lithography to pattern well-ordered arrays of Au nanodisks onto Si wafers; the diameter of each Au disk is 700 nm, and the distance between each Au disk is 4 μm. The patterned wafer was cut into identical pieces to perform a study of how the etch time determined both the embedded depth and photoresponse. AFM was conducted both before and after etching to determine the embedded depth. The samples were then assembled into photoelectrodes for photocurrent measurements. These experiments were first performed using a highly doped n-Si (111) substrate, and the results are shown in **Figure 3.15**. Similar to the electrodes prepared by nanosphere lithography, the photoresponses of n-Si(111)/Au photoelectrodes after different etching times show that the measured photocurrent increases with increased etching time (**Figure 3.15 a**). The measured embedded depth also follows the same trend as the photocurrent response, as demonstrated in **Figure 3.15 b**. The height of an Au disk on the Si surface is 60 nm before etching, and it decreases with increasing etch time. However, we found that after the height had decreased to around 47 nm, etching was no longer effective in embedding the Au nanodisks further into the Si substrate. According to the back-bond breaking theory, this could be because the preferred etching direction is not along the <111> direction of Si.[42] It is known that each atom on a Si (111) surface has three back bonds, while each atom on a Si (100) surface has only two back bonds. Because of the different back-bond strengths, Si atoms on the (100) surface are most easily removed, and etching occurs preferentially along the <100> direction.[43, 44] To test this hypothesis, we performed the same experiments on a n-Si(100) substrates.

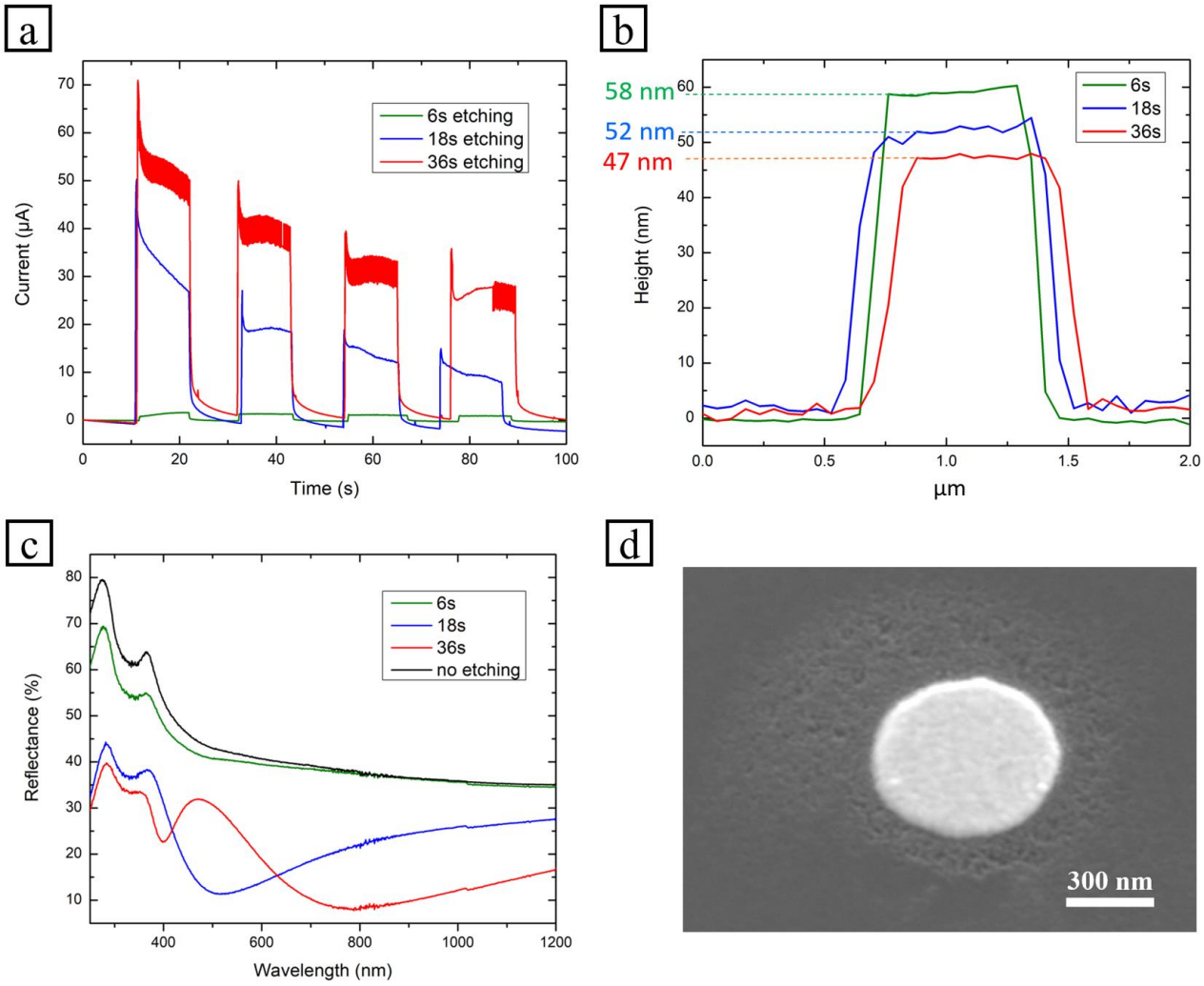

Figure 3.15 (a) Photocurrent responses of n-Si(111)/Au nanoarray photoelectrodes prepared by laser-write lithography under visible light illumination after different etching times in a diluted solution of HF/H_2O_2. (b) AFM height measurements of single Au disks on n-Si(111) substrates after different etching times. (c) Reflectance spectra of n-Si(111)/Au nanoarray photoelectrodes with different etching times. (d) SEM image of a Au nanodisk fabricated on a n-Si(111) substrate after etching with a diluted HF/H_2O_2 solution for 40 s. The thickness of the Au nanodisk is 60 nm.

For the highly doped n-Si (111)/Au samples, we observed a color change around the Au coated region during the etching process. The color varied from green to yellow depending on the etching time. **Figure 3.15 c** shows reflectance spectra for these samples, and the measured spectra varied substantially for different etching times. The reflectance spectra indicated that the enhancement of light absorption increases with etching time, which is consistent with the

photocurrent response. Given the large absorption enhancement with an embedded depth of only tens of nanometers, we expect that there could be other morphology changes, leading to the strong reflectance and color change. From the SEM image of the n-Si(111)/Au sample after a 40-s etch, we observed porous structures formed in the Si substrate around the patterned Au disks (**Figure 3.15 d**). The formation of porous silicon by metal-assisted chemical etching has been attributed to the diffusion of holes from the noble metal/silicon interface to the metal-free Si regions during etching.[45, 46] It was also suggested that more injection of holes occurs in highly doped Si due to less band bending at the highly doped Si/solution interface compared to lightly doped Si.[47, 48] Therefore, porous silicon will be more likely to form in a highly doped Si substrate, which enhances light absorption and could be the main cause of the observed photocurrent enhancement in the n-Si(111)/Au photoelectrodes.

To investigate the effect of embedded depth, the formation of porous silicon during the etching process should be avoided. We next performed the same experiments on lightly doped n-Si(100) substrates that were done using the highly doped n-Si (111)/Au substrates. The results of the lightly doped n-Si(100)/Au nanoarray photoelectrodes are shown in **Figure 3.16**. The height of the Au disks on the Si surface decreases with increasing etch time. The etching also stops being effective for this substrate in embedding the Au nanodisks at longer etch times. The original Au disk height was 60 nm, and the decrease in the Au disk height ceased at around 44 nm (**Figure 3.16 b**). Both the back-bond strength and the surface oxidation state of Si are found to affect the etching direction.[49] When the relative concentration of oxidant is high, the surface termination of Si will become Si–OH or SiO_2, which prevents the surface from further etching in this direction.[50] The etchant we applied has a high oxidant concentration ($HF:H_2O_2:H_2O$ = 5:2:1), which could

explain why the etching direction is not effective along the <100> direction despite the relatively weak back-bond strength of the Si (100) surface.

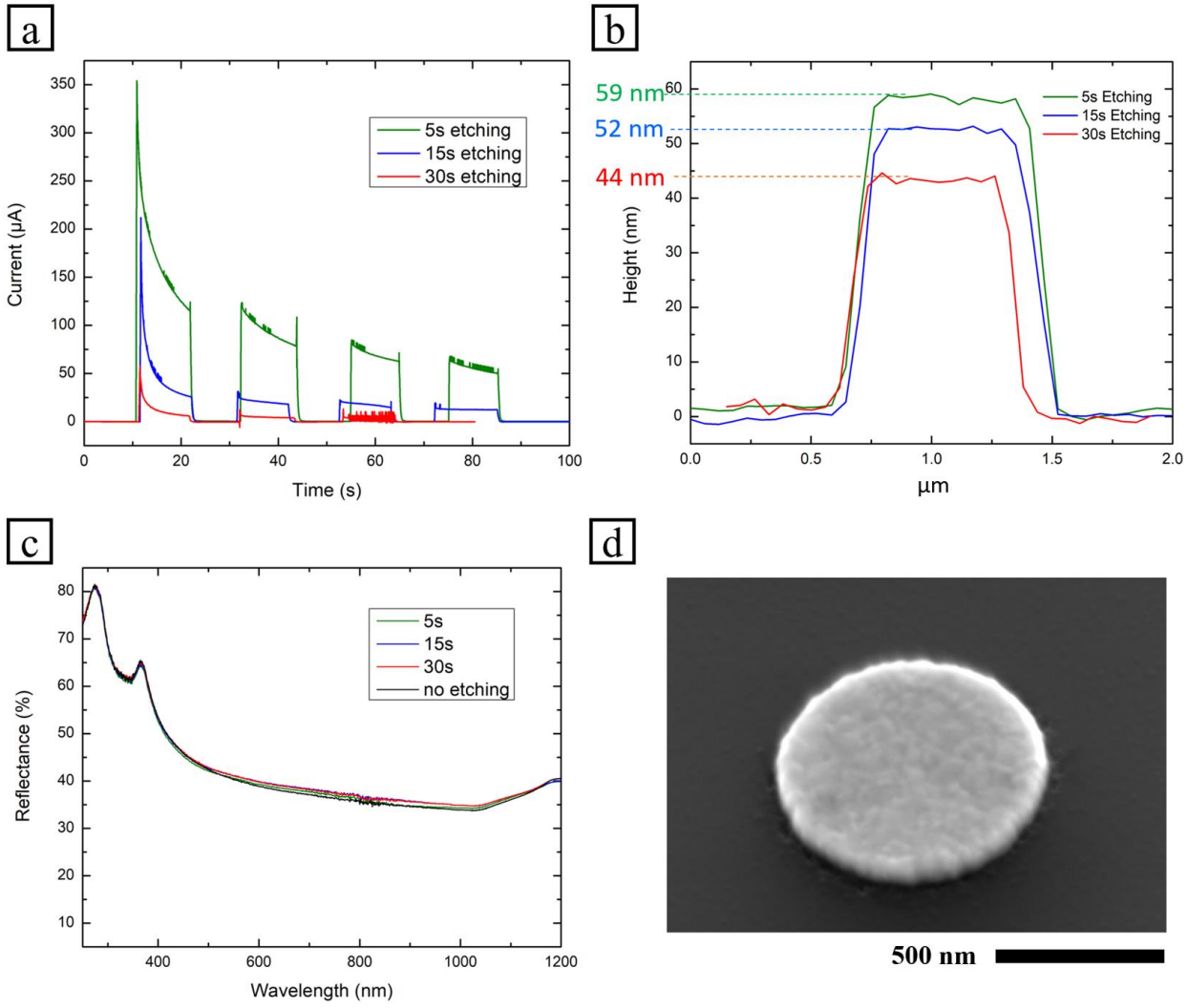

Figure 3.16 (a) Photocurrent responses of n-Si(100)/Au nanoarray photoelectrodes under visible light illumination after different etching times in a diluted HF/H_2O_2 solution. (b) AFM height measurements of single Au disks on n-Si(100) substrates after different etching times. (c) Reflectance spectra of n-Si(100)/Au samples with different etching times. (d) SEM image of a Au nanodisk fabricated on a n-Si(100) substrate after etching with a diluted HF/H_2O_2 solution for 30 s. The thickness of the Au nanodisk is 60 nm.

In contrast to the highly doped n-Si (111)/Au samples, no color change was observed in the lightly doped n-Si(100)/Au samples after etching. The measured reflectance spectra were

nearly the same for each sample after different etching times, as demonstrated in **Figure 3.16 c**. The photocurrent response decreases with increasing etch time and even completely died out for the n-Si(100)/Au nanoarray photoelectrode etched for 30 s (**Figure 3.16 a**). This observation also indicated the presence of SiO_2 at the Si(100)/Au interface, which not only prevents further etching but also blocks the charge transport. An SEM image of a lightly doped n-Si(100)/Au sample after etching is shown in **Figure 3.16 d**. The widening and roughness of the Si substrate around the perimeter of the Au disk support one of the proposed models for metal-assisted chemical etching. In this model, the Si atoms are oxidized and dissolved at the interface between the metal and Si, and the etchant and byproducts diffuse along this interfacial pathway.[41, 48]

3.4 Summary and Conclusions

Two different configurations of plasmonic Au/TiO_2 heterostructures were successfully fabricated to track the photochemistry for both hot electrons and holes. In the first configuration, the Au nanostructures were patterned on an ITO electrode and then coated with a TiO_2 layer. The generation of cathodic photocurrent in the ITO/Au nanoarray/TiO_2 photoelectrode under visible light irradiation indicates that hot electrons in the Au nanostructure are injected into the TiO_2 layer. Photoelectrodeposition of Ag on the TiO_2 layer revealed the locations where hot electrons were extracted. In the reverse configuration, in which the Au nanostructures were patterned on top of the TiO_2 layer, the extracted hot holes were tracked by the photodeposition of PbO_2. The deposition maps obtained from the two different Au/TiO_2 heterostructures both suggest that the reactivities of hot carriers are higher near the sharp edges of the Au nanostructures, where the electromagnetic field intensities are also the highest. Au dimers with an interparticle spacing less than 50 nm were successfully patterned onto TiO_2 films by electron beam lithography to investigate the effect of

plasmonic coupling on hot carrier photochemistry. However, electron beam damage of the TiO_2 surface during the SEM imaging step prevented further photodeposition experiments to be conducted.

Metal-assisted chemical etching was applied to embed Au nanodisks into two different n-Si substrates and investigate how the embedded depth affects hot-carrier collection in n-Si/Au photoelectrodes. After etching, the highly doped n-Si(111)/Au photoelectrodes exhibit enhanced photocurrent, which is attributed to the large absorption enhancement from porous silicon that forms during etching. The etching was not successful in fully embedding Au nanodisks in the highly doped n-Si(111) substrate due to the stronger back-bond strength of Si atoms on the Si (111) surface. When lightly doped n-Si(100) substrates were used, porous silicon was not observed after etching. The photocurrent response decreased with increasing etch times, which shows the opposite trend compared to the n-Si(111)/Au photoelectrodes. This could be caused by the formation of SiO_2 at the Si(100)/Au interface, which also prevented further etching along the <100> direction.

3.5 Acknowledgements

This material is based upon work supported by the National Science Foundation (NSF) under grant no. CHE-1753344. I would like to thank the technicians in the Institute of Materials Science & Engineering, Dr. Huafang Li and Dr. Tyrone Daulton for training and assisting me on the SEM and AFM. I would like to give special thanks to the clean room manager Dr. Rahul Gupta for training me on numerous instruments and processes used in this work (laser-write lithography, thermal evaporation, PVD sputtering, ALD, ellipsometry). Dr. Nathan Reed gave me a lot of help

in thermal evaporation as well as useful discussions of this work. Thanks Dr. Dian Tan for helping me on electron beam lithography.

3.6 References

1. Brus, L., Noble metal nanocrystals: plasmon electron transfer photochemistry and single-molecule Raman spectroscopy. *Accounts of chemical research* **2008,** *41* (12), 1742-1749.

2. Linic, S.; Christopher, P.; Ingram, D. B., Plasmonic-metal nanostructures for efficient conversion of solar to chemical energy. *Nature Materials* **2011,** *10* (12), 911-921.

3. Atwater, H. A.; Polman, A., Plasmonics for improved photovoltaic devices. *Nature Materials* **2010,** *9*, 205-213.

4. Clavero, C., Plasmon-induced hot-electron generation at nanoparticle/metal-oxide interfaces for photovoltaic and photocatalytic devices. *Nature Photonics* **2014,** *8* (2), 95-103.

5. Warren, S. C.; Walker, D. A.; Grzybowski, B. A., Plasmoelectronics: coupling plasmonic excitation with electron flow. *Langmuir* **2012,** *28* (24), 9093-9102.

6. Warren, S. C.; Thimsen, E., Plasmonic solar water splitting. *Energy & Environmental Science* **2012,** *5* (1), 5133-5146.

7. Hao, E.; Schatz, G. C., Electromagnetic fields around silver nanoparticles and dimers. *The Journal of Chemical Physics* **2004,** *120* (1), 357-366.

8. Kvítek, O.; Siegel, J.; Hnatowicz, V.; Švorčík, V., Noble metal nanostructures influence of structure and environment on their optical properties. *Journal of Nanomaterials* **2013,** *2013*.

9. Marchuk, K.; Willets, K. A., Localized surface plasmons and hot electrons. *Chemical Physics* **2014,** *445*, 95-104.

10. Cushing, S., Plasmonic hot carriers skip out in femtoseconds. *Nature Photonics* **2017,** *11* (12), 748-749.

11. Smith, J. G.; Faucheaux, J. A.; Jain, P. K., Plasmon resonances for solar energy harvesting: a mechanistic outlook. *Nano Today* **2015,** *10* (1), 67-80.

12. Knight, M. W.; Sobhani, H.; Nordlander, P.; Halas, N. J., Photodetection with active optical antennas. *Science* **2011,** *332* (6030), 702-704.

13. Zhang, Z.; Yates Jr, J. T., Band bending in semiconductors: chemical and physical consequences at surfaces and interfaces. *Chemical Reviews* **2012,** *112* (10), 5520-5551.

14. Valenti, M.; Jonsson, M.; Biskos, G.; Schmidt-Ott, A.; Smith, W., Plasmonic nanoparticle-semiconductor composites for efficient solar water splitting. *Journal of Materials Chemistry A* **2016,** *4* (46), 17891-17912.

15. Giugni, A.; Torre, B.; Toma, A.; Francardi, M.; Malerba, M.; Alabastri, A.; Zaccaria, R. P.; Stockman, M. I.; Di Fabrizio, E., Hot-electron nanoscopy using adiabatic compression of surface plasmons. *Nature Nanotechnology* **2013,** *8* (11), 845-852.

16. Leenheer, A. J.; Narang, P.; Lewis, N. S.; Atwater, H. A., Solar energy conversion via hot electron internal photoemission in metallic nanostructures: efficiency estimates. *Journal of Applied Physics* **2014,** *115* (13), 134301.

17. Mubeen, S.; Lee, J.; Singh, N.; Krämer, S.; Stucky, G. D.; Moskovits, M., An autonomous photosynthetic device in which all charge carriers derive from surface plasmons. *Nature Nanotechnology* **2013,** *8* (4), 247-251.

18. White, T. P.; Catchpole, K. R., Plasmon-enhanced internal photoemission for photovoltaics: theoretical efficiency limits. *Applied Physics Letters* **2012,** *101* (7), 073905.

19. Brown, A. M.; Sundararaman, R.; Narang, P.; Goddard III, W. A.; Atwater, H. A., Nonradiative plasmon decay and hot carrier dynamics: effects of phonons, surfaces, and geometry. *ACS Nano* **2016,** *10* (1), 957-966.

20. Wu, K.; Chen, J.; McBride, J. R.; Lian, T., Efficient hot-electron transfer by a plasmon-induced interfacial charge-transfer transition. *Science* **2015,** *349* (6248), 632-635.

21. Knight, M. W.; Wang, Y.; Urban, A. S.; Sobhani, A.; Zheng, B. Y.; Nordlander, P.; Halas, N. J., Embedding plasmonic nanostructure diodes enhances hot electron emission. *Nano Letters* **2013,** *13* (4), 1687-1692.

22. Scales, C.; Berini, P., Thin-film Schottky barrier photodetector models. *IEEE Journal of quantum electronics* **2010,** *46* (5), 633-643.

23. Brongersma, M. L.; Halas, N. J.; Nordlander, P., Plasmon-induced hot carrier science and technology. *Nature Nanotechnology* **2015,** *10* (1), 25-34.

24. Goykhman, I.; Desiatov, B.; Khurgin, J.; Shappir, J.; Levy, U., Waveguide based compact silicon Schottky photodetector with enhanced responsivity in the telecom spectral band. *Optics Express* **2012,** *20* (27), 28594-28602.

25. Wang, S.; Gao, Y.; Miao, S.; Liu, T.; Mu, L.; Li, R.; Fan, F.; Li, C., Positioning the water oxidation reaction sites in plasmonic photocatalysts. *Journal of the American Chemical Society* **2017,** *139* (34), 11771-11778.

26. Kim, N. H.; Meinhart, C. D.; Moskovits, M., Plasmon-mediated reduction of aqueous platinum ions: the competing roles of field enhancement and hot charge carriers. *The Journal of Physical Chemistry C* **2016,** *120* (12), 6750-6755.

27. Minamimoto, H.; Toda, T.; Futashima, R.; Li, X.; Suzuki, K.; Yasuda, S.; Murakoshi, K., Visualization of active sites for plasmon-induced electron transfer reactions using photoelectrochemical polymerization of pyrrole. *The Journal of Physical Chemistry C* **2016,** *120* (29), 16051-16058.

28. Huang, W.; Qian, W.; El-Sayed, M. A.; Ding, Y.; Wang, Z. L., Effect of the lattice crystallinity on the electron− phonon relaxation rates in gold nanoparticles. *The Journal of Physical Chemistry C* **2007,** *111* (29), 10751-10757.

29. Tanvi; Mahajan, A.; Bedi, R.; Kumar, S.; Saxena, V.; Aswal, D., Effect of the crystallinity of silver nanoparticles on surface plasmon resonance induced enhancement of effective absorption cross-section of dyes. *Journal of Applied Physics* **2015,** *117* (8), 083111.

30. Bechelany, M.; Maeder, X.; Riesterer, J.; Hankache, J.; Lerose, D.; Christiansen, S.; Michler, J.; Philippe, L., Synthesis mechanisms of organized gold nanoparticles: influence of annealing temperature and atmosphere. *Crystal Growth & Design* **2010,** *10* (2), 587-596.

31. Sakai, N.; Fujiwara, Y.; Takahashi, Y.; Tatsuma, T., Plasmon-resonance-based generation of cathodic photocurrent at electrodeposited gold nanoparticles coated with TiO_2 films. *ChemPhysChem* **2009,** *10* (5), 766-769.

32. Sambur, J. B.; Chen, T.-Y.; Choudhary, E.; Chen, G.; Nissen, E. J.; Thomas, E. M.; Zou, N.; Chen, P., Sub-particle reaction and photocurrent mapping to optimize catalyst-modified photoanodes. *Nature* **2016,** *530* (7588), 77-80.

33. Yu, Y.; Sundaresan, V.; Willets, K. A., Hot carriers versus thermal effects: resolving the enhancement mechanisms for plasmon-mediated photoelectrochemical reactions. *The Journal of Physical Chemistry C* **2018,** *122* (9), 5040-5048.

34. Cortés, E.; Xie, W.; Cambiasso, J.; Jermyn, A. S.; Sundararaman, R.; Narang, P.; Schlücker, S.; Maier, S. A., Plasmonic hot electron transport drives nano-localized chemistry. *Nature Communications* **2017,** *8* (1), 1-10.

35. Neelisetty, K. K.; Mu, X.; Gutsch, S.; Vahl, A.; Molinari, A.; von Seggern, F.; Hansen, M.; Scherer, T.; Zacharias, M.; Kienle, L., Electron beam effects on oxide thin films—structure and electrical property correlations. *Microscopy and Microanalysis* **2019,** *25* (3), 592-600.

36. Kern, P.; Jäggi, C.; Utke, I.; Friedli, V.; Michler, J., Local electron beam induced reduction and crystallization of amorphous titania films. *Applied Physics Letters* **2006,** *89* (2), 021902.

37. Li, X.; Bohn, P., Metal-assisted chemical etching in HF/H_2O_2 produces porous silicon. *Applied Physics Letters* **2000,** *77* (16), 2572-2574.

38. Akan, R.; Parfeniukas, K.; Vogt, C.; Toprak, M. S.; Vogt, U., Reaction control of metal-assisted chemical etching for silicon-based zone plate nanostructures. *RSC Advances* **2018,** *8* (23), 12628-12634.

39. Divan, R.; Rosenthal, D.; Ogando, K.; Ocola, L. E.; Rosenmann, D.; Moldovan, N., Metal-assisted etching of silicon molds for electroforming. *Journal of Vacuum Science & Technology B, Nanotechnology and Microelectronics: Materials, Processing, Measurement, and Phenomena* **2013,** *31* (6), 06FF03.

40. Geyer, N.; Fuhrmann, B.; Huang, Z.; de Boor, J.; Leipner, H. S.; Werner, P., Model for the mass transport during metal-assisted chemical etching with contiguous metal films as catalysts. *The Journal of Physical Chemistry C* **2012,** *116* (24), 13446-13451.

41. Liu, G.; Young, K. L.; Liao, X.; Personick, M. L.; Mirkin, C. A., Anisotropic nanoparticles as shape-directing catalysts for the chemical etching of silicon. *Journal of the American Chemical Society* **2013,** *135* (33), 12196-12199.

42. To, W.-K.; Fu, J.; Yang, X.; Roy, V.; Huang, Z., Porosification-reduced optical trapping of silicon nanostructures. *Nanoscale* **2012,** *4* (19), 5835-5839.

43. Chen, W.; Liu, Y.; Yang, L.; Wu, J.; Chen, Q.; Zhao, Y.; Wang, Y.; Du, X., Difference in anisotropic etching characteristics of alkaline and copper based acid solutions for single-crystalline Si. *Scientific Reports* **2018,** *8* (1), 1-8.

44. Bai, F.; To, W.-K.; Huang, Z., Porosification-induced back-bond weakening in chemical etching of n-Si (111). *The Journal of Physical Chemistry C* **2013,** *117* (5), 2203-2209.

45. Balasundaram, K.; Sadhu, J. S.; Shin, J. C.; Azeredo, B.; Chanda, D.; Malik, M.; Hsu, K.; Rogers, J. A.; Ferreira, P.; Sinha, S., Porosity control in metal-assisted chemical etching of degenerately doped silicon nanowires. *Nanotechnology* **2012,** *23* (30), 305304.

46. Romano, L.; Stampanoni, M., Microfabrication of X-ray Optics by Metal Assisted Chemical Etching: A Review. *Micromachines* **2020,** *11* (6), 589.

47. Hochbaum, A. I.; Gargas, D.; Hwang, Y. J.; Yang, P., Single crystalline mesoporous silicon nanowires. *Nano Letters* **2009,** *9* (10), 3550-3554.

48. Huang, Z.; Geyer, N.; Werner, P.; De Boor, J.; Gösele, U., Metal-assisted chemical etching of silicon: a review: in memory of Prof. Ulrich Gösele. *Advanced Materials* **2011,** *23* (2), 285-308.

49. Han, H.; Huang, Z.; Lee, W., Metal-assisted chemical etching of silicon and nanotechnology applications. *Nano Today* **2014,** *9* (3), 271-304.

50. Huang, Z.; Shimizu, T.; Senz, S.; Zhang, Z.; Geyer, N.; Gosele, U., Oxidation rate effect on the direction of metal-assisted chemical and electrochemical etching of silicon. *The Journal of Physical Chemistry C* **2010,** *114* (24), 10683-10690.

Chapter 4

Summary and Future Studies

4.1 Summary and Future Studies

The major conclusion of Chapter 2 is that we have demonstrated we could achieve the pinch-off regime using microscale Ni catalysts by manipulating the difference in barrier height at an inhomogeneous junction of a Ni-patterned silicon photoanode. The barrier heights at each junction were altered by depositing/etching different interfacial oxide layers. Previous pinched-off Si photoanodes that have been reported were all based on nanoscale catalysts, and most are synthesized by electrodeposition.[1-4] Although electrodeposition is a simple technique to prepare Si photoanodes decorated with nanoparticle catalysts, it has poor control of individual catalyst sizes. Moreover, because electrodeposition cannot be performed on silicon substrates with a pre-formed thin oxide layer, the tunability of the junction barrier heights is limited. In contrast, we fabricated Ni-patterned silicon photoanodes using a combination of laser-write lithography and interfacial engineering. The type and thickness of the interfacial oxide layers were controlled before Ni deposition, and the size and interparticle spacing of the deposited Ni catalysts were also precisely controlled.

Our study suggests that fabricating Si photoanodes through lithographic patterning methods will enable further exploration of the effect of tuning potential barriers in MIS junctions on the pinch-off effect. The pinch-off effect can be strengthened from an increased barrier-height difference (Δ) at the inhomogeneous Schottky junction, analogous to the effect of a decreased contact size for the catalyst. The measured barrier height for the Ni-free n-Si/$SiO_{x,RCA}$/Al_2O_3 junction is 1.29 eV, which provided the largest Δ among the three photoanode configurations in our study, and enabled the pinch-off effect in the n-Si/$SiO_{x,RCA}$/Al_2O_3/Ni (1.5μm) photoanodes. The interfacial barrier height between n-Si(100) and SiO_2 with a thickness of 3.6 nm was found to be 3.1 eV in a metal-oxide-semiconductor (MOS) device.[5] For thinner SiO_2 layers between 1.5 nm

to 3.1 nm, the barrier heights can reach a value close to 2 eV.[6] Due to the large potential barrier that these thin SiO_2 tunneling layers can provide, we believe SiO_2 is a good candidate for the fabrication of MIS photoanodes with inhomogeneous barrier heights. Rapid thermal oxidation is a well-known method for synthesizing ultra-thin, high-quality SiO_2 films.[7] We expect that by incorporating this process to provide a higher n-Si/SiO_2 junction barrier height, the photovoltage of our Ni-patterned Si photoanode can be further improved.

Besides tunning the barrier heights at the inhomogeneous junctions of the Si photoanode, the size of the Ni catalysts can also be reduced to improve the photovoltage of the MIS photoanodes. Currently, the smallest Ni catalyst investigated in our study is 1.5 μm in diameter. By using the laser-write lithography process with two photoresist layers (i.e., including an additional LOR layer), we can achieve a metal catalyst size of 700 nm in diameter (demonstrated in Chapter 3). Future studies should first investigate the size-dependent photovoltage of the MIS photoanodes patterned with Ni catalysts within this size range. To further study MIS photoanodes with Ni catalysts that have diameters below 700 nm, nanosphere lithography can be implemented to fabricate arrays of Ni disks with smaller sizes. Different sizes of Ni disks can be obtained by varying the size of the microsphere that is used for the lithographic mask.[8, 9]

Stability is a major concern for partially coated Si photoanodes because their deterioration has been attributed to the loss of catalyst islands from the Si substrate due to etching of Si in the electrolyte.[3] The rate of decay is related to the catalyst size on the photoanode, with smaller catalysts being more easily undercut, leading to poor photoanode stabilities in the reported pinched-off Si photoanodes with electrodeposited nanoparticle catalysts.[3, 10] Inspired by the research in Chapter 3, in which we embedded Au nanostructures into the silicon substrate, we propose a new strategy for stabilizing Si to prevent the undercutting of catalysts during operation

by embedding the patterned catalyst into the Si photoanode. Since Si etching surrounding the catalyst is thought to be the primary cause of catalyst loss, we believe that this embedding approach can prolong the lifetime of the photoanode.

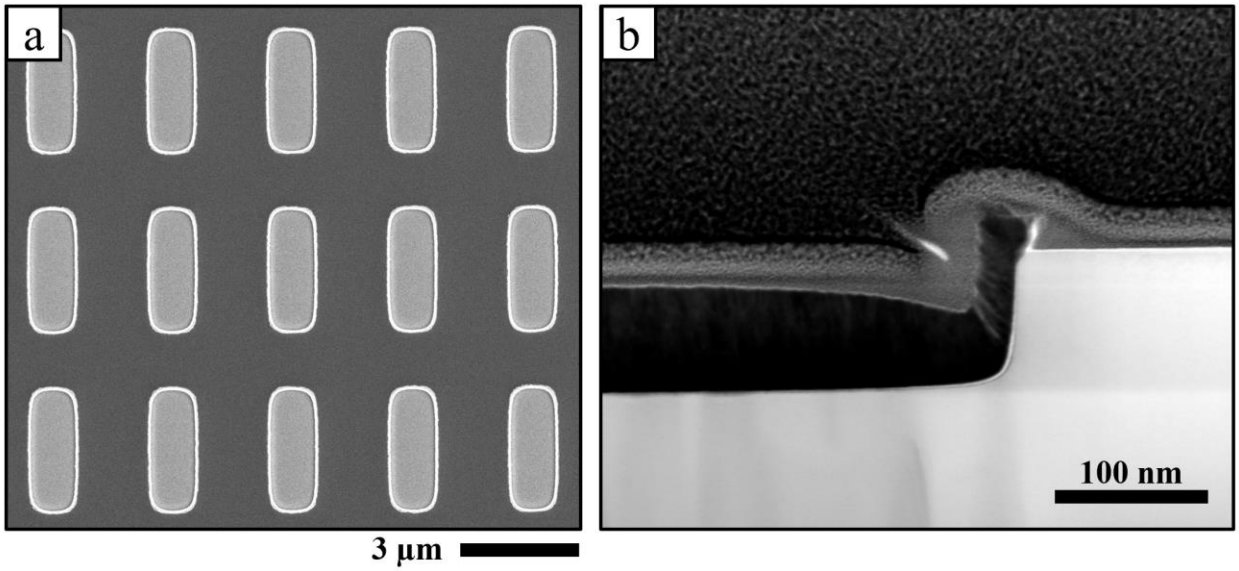

Figure 4.1 Embedded n-Si/Ni photoanode fabricated by direct laser-write lithography and RIE. (a) SEM image of the embedded n-Si/Ni photoanode having a Ni filling fraction of 18%. (b) Cross-sectional TEM image of the embedded n-Si/Ni photoanode in (a). The thickness of the Ni catalyst is 80 nm.

We have already obtained preliminary results to verify this hypothesis. First, we patterned Ni catalysts on both n-Si (111) and np^+-Si (111) substrates using direct laser-write lithography. The embedded Ni-patterned Si photoanodes were obtained by generating trenches through the photoresist mask using reactive ion etching (RIE) prior to Ni deposition. **Figure 4.1** shows SEM and cross-sectional TEM images of an embedded n-Si/Ni photoanode. The thickness of the Ni catalyst is 80 nm and was fully embedded into the silicon substrate. The TEM image shows that the Ni catalyst is thicker at the center due to shadowing from the photoresist during sputter deposition of the Ni. The build-up of Ni around the perimeter is also observed. Linear sweep voltammograms of the non-embedded and embedded n-Si/Ni photoanodes were collected in 1 M

KOH (**Figure 4.2**). The current obtained in the dark was negligible (black trace). Anodic photocurrents were measured under visible light illumination. Surprisingly, we observed a 100-mV negative shift in the onset potential for the embedded n-Si/Ni photoanodes compared to the non-embedded ones. We hypothesize that the shift in onset potential is due to the vertical interfaces introduced in the embedded photoanodes. It could be induced by the change in energetics or charge-transfer resistance at the interface. High-resolution electron microscopy, as well as electrochemical impedance spectroscopy measurements, can provide insights into the origin of the shift in onset potential.

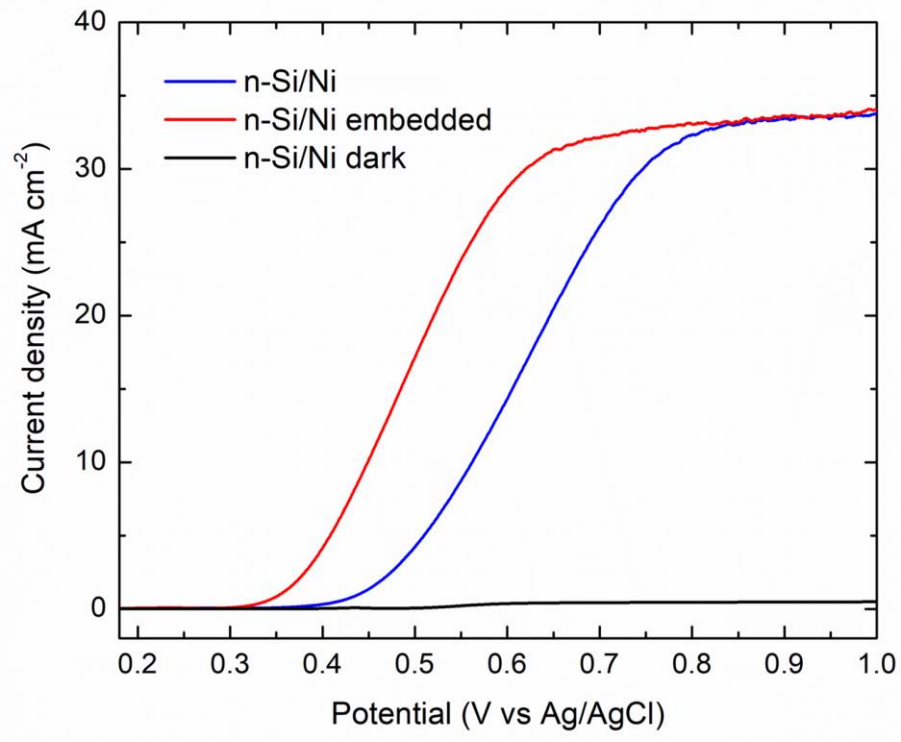

Figure 4.2 Photocurrent density versus applied potential (*j*-*E*) measured using linear sweep voltammetry for n-Si/Ni photoanodes with a 9% Ni filling fraction in 1 M KOH under ELH-lamp illumination at 100 mW cm^{-2}. The responses of the non-embedded and embedded n-Si/Ni photoanodes are shown in blue and red, respectively. The black trace shows a n-Si/Ni photoanode in the dark.

The photovoltage of a n-Si photoanode can be improved by the addition of a p^+ emitter layer on the surface of the n-Si.[11, 12] To achieve a better photovoltage and investigate the effect of embedding in the photoanodes with an emitter layer, we implemented the same patterning and embedding method on np^+-Si (111) substrates purchased from Addison Engineering. The p^+ emitter layer was prepared by boron ion implantation on a n-Si substrate at an incident angle of 7° with a dose of 1×10^{14} cm^{-2} at acceleration voltage of 45 keV followed with a dose of 5×10^{14} cm^{-2} at 32 keV. Activation of the doped p^+ junction layer was done through thermal annealing at 1000°C. The anodic behavior of the embedded and non-embedded np^+-Si/Ni photoanodes were also measured in 1 M KOH under illumination with visible light. Cyclic voltammograms of the photoanodes are shown in **Figure 4.3**. Both the embedded and non-embedded np^+-Si/Ni photoanodes exhibited the same onset potential, but the maximum photocurrent density of the embedded photoanode was higher than the non-embedded one. The measured reflectance spectra indicate a decreased reflectance after the Ni catalysts are embedded, which could explain the photocurrent enhancement in the embedded np^+-Si/Ni photoanodes.

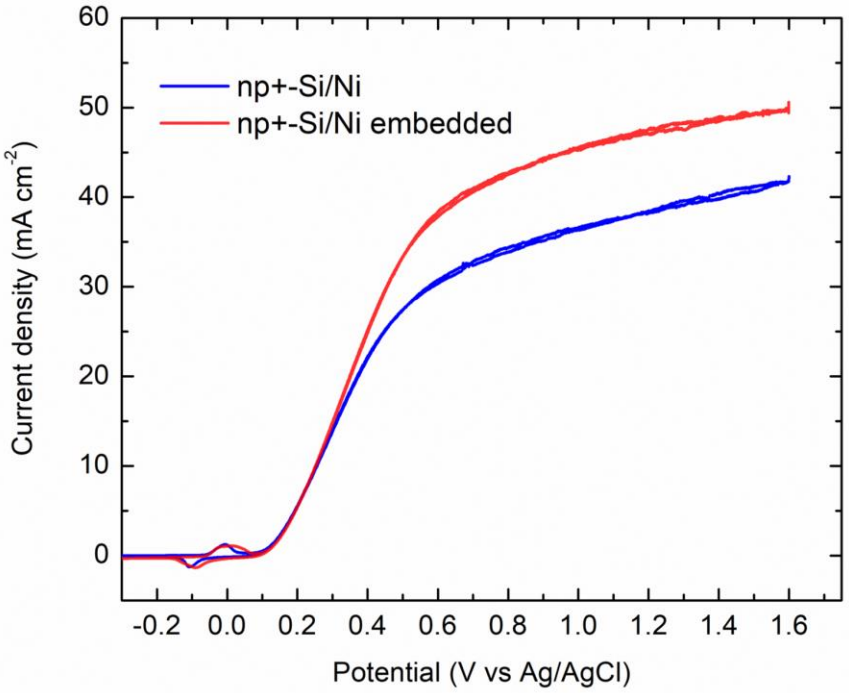

Figure 4.3. Cyclic voltammetry of np^+-Si/Ni photoanodes with a 9% Ni filling fraction in 1 M KOH under ELH-lamp illumination at an irradiance of 100 mW cm^{-2}. The scans of the non-embedded and embedded n-Si/Ni photoanodes are shown in blue and red, respectively.

To test the effectiveness of stabilizing Si photoanodes by embedding the Ni catalyst, we studied the morphology change of the photoanodes after being immersed in the same electrolyte solution used for OER for an extended period. The SEM image in **Figure 4.4 b** clearly demonstrates the loss of Ni catalysts from the non-embedded np^+-Si/Ni photoanode after being immersed in 1 M KOH for 24 h. In contrast, Ni catalysts in the embedded np^+-Si/Ni photoanode remained in place after 24 h. However, the Ni catalysts were no longer embedded because the surrounding Si had been etched (**Figure 4.4 d**). These observations indicate that the embedding method could prevent the undercutting of catalysts when np^+-Si/Ni photoanodes are immersed in KOH but not performing water oxidation. However, under operating conditions, the deactivation process is more complicated. Recent studies suggest the formation of SiO_2 at the interface between the catalyst and Si during operation leads to the failure of Si photoanodes.[11] Our preliminary results

have shown that the embedded np^+-Si/Ni photoanodes can survive up to 250 h of continuous operation in 1 M KOH under applied bias and illumination. Further studies are required to understand the stabilizing mechanism for the embedded photoanodes under active operation.

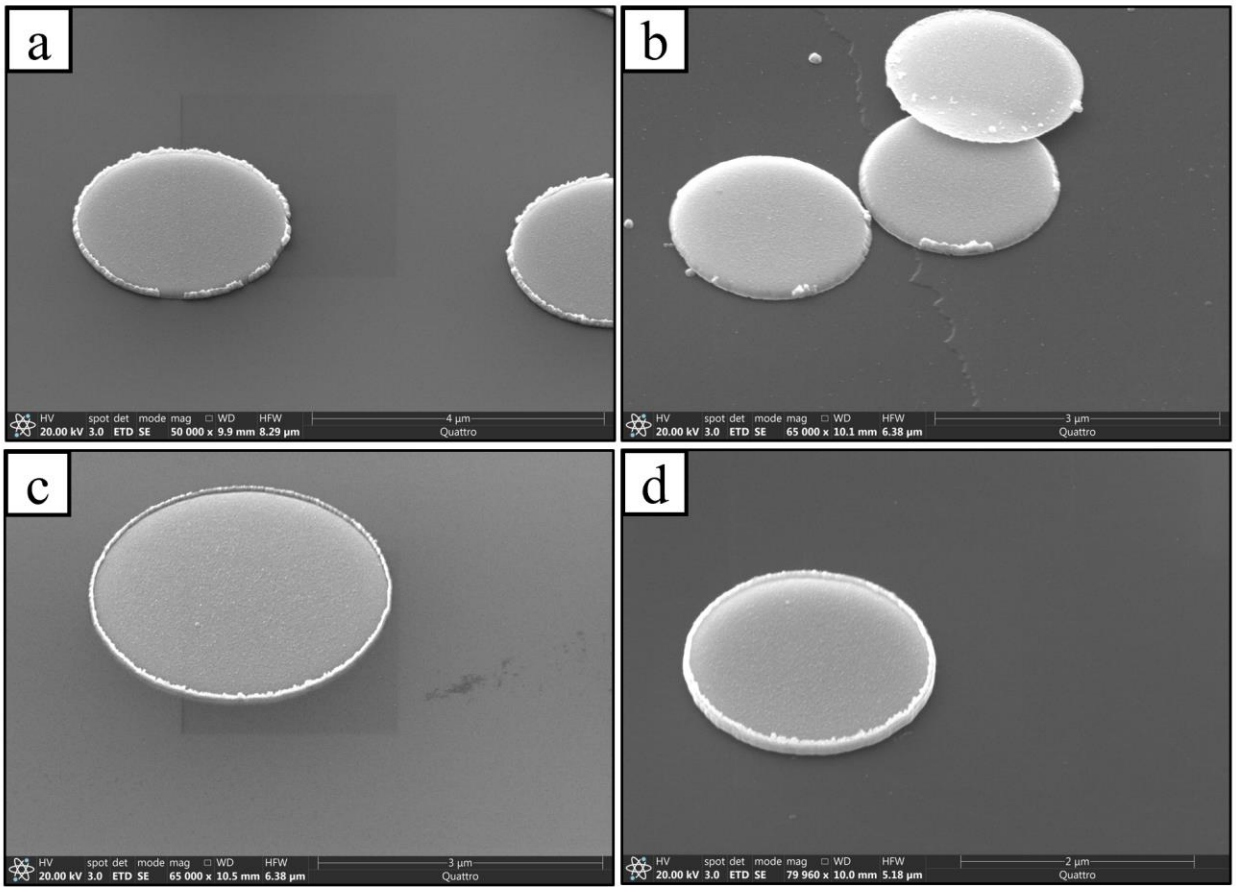

Figure 4.4 (a, b) SEM images of non-embedded np^+-Si/Ni photoanodes (a) before and (b) after immersion in 1 M KOH for 24 h. (c, d) SEM images of embedded np^+-Si/Ni photoanodes (c) before and (d) after immersion in 1 M KOH for 24 h. The thickness of the Ni catalyst is 80 nm.

The dependency of catalyst size on the stability of Si-photoanodes has not been demonstrated in previous studies. Therefore, an important area of future work should be to examine the stability of Si-photoanodes with varied Ni catalyst sizes ranging from several micrometers to a hundred nanometers. A patterned n-Si/$SiO_{x,RCA}$/Al_2O_3/Ni photoanode in this size range can operate in the pinch-off regime, and the stability test under active operation would

provide information for practical use. In combination with research on size-dependent photovoltage within this size range, important insights can be gained for the optimal design of MIS photoanodes.

4.2 References

1. Hill, J. C.; Landers, A. T.; Switzer, J. A., An electrodeposited inhomogeneous metal–insulator–semiconductor junction for efficient photoelectrochemical water oxidation. *Nature Materials* **2015,** *14* (11), 1150-1155.

2. Loget, G.; Fabre, B.; Fryars, S.; Meriadec, C.; Ababou-Girard, S., Dispersed Ni nanoparticles stabilize silicon photoanodes for efficient and inexpensive sunlight-assisted water oxidation. *ACS Energy Letters* **2017,** *2* (3), 569-573.

3. Oh, K.; Mériadec, C.; Lassalle-Kaiser, B.; Dorcet, V.; Fabre, B.; Ababou-Girard, S.; Joanny, L.; Gouttefangeas, F.; Loget, G., Elucidating the performance and unexpected stability of partially coated water-splitting silicon photoanodes. *Energy & Environmental Science* **2018,** *11* (9), 2590-2599.

4. Lee, S. A.; Lee, T. H.; Kim, C.; Lee, M. G.; Choi, M.-J.; Park, H.; Choi, S.; Oh, J.; Jang, H. W., Tailored NiO_x/Ni cocatalysts on silicon for highly efficient water splitting photoanodes via pulsed electrodeposition. *ACS Catalysis* **2018,** *8* (8), 7261-7269.

5. Kasprzak, L.; Laibowitz, R.; Ohring, M., Dependence of the Si-SiO_2 barrier height on SiO_2 thickness in MOS tunnel structures. *Journal of Applied Physics* **1977,** *48* (10), 4281-4286.

6. Hadjadj, A.; Simonetti, O.; Maurel, T.; Salace, G.; Petit, C., Si–SiO_2 barrier height and its temperature dependence in metal-oxide-semiconductor structures with ultrathin gate oxide. *Applied Physics Letters* **2002,** *80* (18), 3334-3336.

7. Depas, M.; Van Meirhaeghe, R.; Laflere, W.; Cardon, F., Electrical characteristics of Al/SiO2/n-Si tunnel diodes with an oxide layer grown by rapid thermal oxidation. *Solid-State Electronics* **1994,** *37* (3), 433-441.

8. Hulteen, J. C.; Van Duyne, R. P., Nanosphere lithography: A materials general fabrication process for periodic particle array surfaces. *Journal of Vacuum Science & Technology A: Vacuum, Surfaces, and Films* **1995,** *13* (3), 1553-1558.

9. Yang, S. M.; Jang, S. G.; Choi, D. G.; Kim, S.; Yu, H. K., Nanomachining by colloidal lithography. *Small* **2006,** *2* (4), 458-475.

10. Ying, Z.; Yang, X.; Tong, R.; Zhu, Q.; Chen, T.; He, Z.; Pan, H., Enhancing the Efficiency and Stability of NiO_x-Based Silicon Photoanode via Interfacial Engineering. *ACS Applied Energy Materials* **2019,** *2* (9), 6883-6890.

11. Sun, K.; Ritzert, N. L.; John, J.; Tan, H.; Hale, W. G.; Jiang, J.; Moreno-Hernandez, I.; Papadantonakis, K. M.; Moffat, T. P.; Brunschwig, B. S.; Lewis, N.S., Performance and failure modes of Si anodes patterned with thin-film Ni catalyst islands for water oxidation. *Sustainable Energy & Fuels* **2018,** *2* (5), 983-998.

12. Oh, S.; Oh, J., High performance and stability of micropatterned oxide-passivated photoanodes with local catalysts for photoelectrochemical water splitting. *The Journal of Physical Chemistry C* **2016,** *120* (1), 133-141.